LIGHT AND CHEMISTRY AT THE INTERFACE OF THEORY AND EXPERIMENT

by

James RW Ulcickas

A Thesis

Submitted to the Faculty of Purdue University

In Partial Fulfillment of the Requirements for the degree of

Doctor of Philosophy

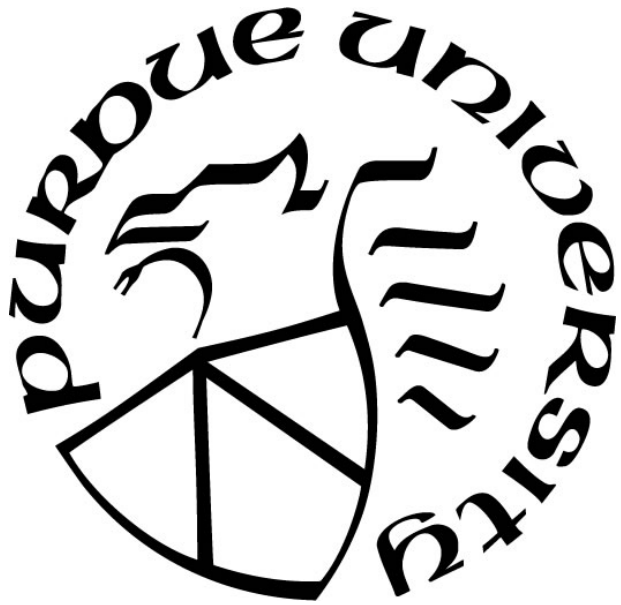

Department of Chemistry

West Lafayette, Indiana

May 2020

THE PURDUE UNIVERSITY GRADUATE SCHOOL
STATEMENT OF COMMITTEE APPROVAL

Dr. Garth Simpson, Chair
Department of Chemistry

Dr. Lyudmila Slipchenko
Department of Chemistry

Dr. Corey Thompson
Department of Chemistry

Dr. Gregery Buzzard
Department of Mathematics

Approved by:
Dr. Christine Hrycyna

Dedicated to my family, who fought for me when I could not.

ACKNOWLEDGMENTS

The author would like to acknowledge support from the Purdue University Department of Chemistry and College of Science in the form of a Ross Assistantship and Bilsland Dissertation Fellowship.

Paul Schmidt and Ximeng Dow provided significant guidance in the first year of my Ph.D. and conducted the experiments on collagen discussed in Chapter 2. Collaborating authors Fengyuan "Max" Deng and Changqin "Tina" Ding contributed a large portion to the other chapters of this thesis regarding polarization analysis. Max in particular was a fantastic mentor during the first several years of my Ph.D.

I am grateful to Lyudmila Slipchenko, for assistance in high performance computing for modeling quantum chemistry. Gregery Buzzard and Charlie Bouman provided significant assistance in the application of multi-agent consensus equilibrium to chemical problems. Thanks to them for developing the theory.

I would also like to thank Garth Simpson, whose consistent enthusiasm for physical chemistry and analytical science drew me to the laboratory and enabled the creation of this thesis. It was only through his guidance that I was able to grow into the chemist I am today.

TABLE OF CONTENTS

LIST OF TABLES

LIST OF FIGURES

LIST OF ABBREVIATIONS

CARS	Coherent Anti-Stokes Raman Scattering
CD	Circular Dichroism
CPL	Circularly Polarized Light
DCM	Dichloromethane
DFT	Density Functional Theory
ECD	Electronic Circular Dichroism
EOM	Electro-Optic Modulator
FDCD	Fluorescence Detected Circular Dichroism
F-ORD	Fluorescence Optical Rotary Dispersion
FoV	Field of View
FTIR	Fourier Transform Infrared spectroscopy
H	Horizontal (Polarization)
HF	Hartree-Fock
IR	Infrared
LID	Linear Intensity Difference
LWIR	Long Wave Infrared
MACE	Multi-Agent Consensus Equilibrium
NLO	Nonlinear Optical
NMA	N-methyl acetamide
PD	Photodiode
PMT	Photomultiplier Tube
QCL	Quantum Cascade Laser
QWP	Quarter Waveplate

ROA	Raman Optical Activity
SEROA	Surface Enhanced Raman Optical Activity
SHG	Second Harmonic Generation
SFG	Sum Frequency Generation
SNR	Signal to Noise Ratio
TD-DFT	Time-Dependent Density Functional Theory
TPEF	Two Photon Excited Fluorescence
V	Vertical (Polarization)
VCD	Vibrational Circular Dichroism
1PF	One Photon Fluorescence
μRA	Microretarding Array

ABSTRACT

Optics are a powerful probe of chemical structure that can often be linked to theoretical predictions, providing robustness as a measurement tool. Not only do optical interactions like second harmonic generation (SHG), single and two-photon excited fluorescence (TPEF), and infrared absorption provide chemical specificity at the molecular and macromolecular scale, but the ability to image enables mapping heterogeneous behavior across complex systems such as biological tissue. This thesis will discuss nonlinear and linear optics, leveraging theoretical predictions to provide frameworks for interpreting analytical measurement. In turn, the causal mechanistic understanding provided by these frameworks will enable structurally specific quantitative tools with a special emphasis on application in biological imaging. The thesis will begin with an introduction to 2^{nd} order nonlinear optics and the polarization analysis thereof, covering both the Jones framework for polarization analysis and the design of experiment. Novel experimental architectures aimed at reducing 1/f noise in polarization analysis will be discussed, leveraging both rapid modulation in time through electro-optic modulators (Chapter 2), as well as fixed-optic spatial modulation approaches (Chapter 3). In addition, challenges in polarization-dependent imaging within turbid systems will be addressed with the discussion of a theoretical framework to model SHG occurring from unpolarized light (Chapter 4). The application of this framework to thick tissue imaging for analysis of collagen local structure can provide a method for characterizing changes in tissue morphology associated with some common cancers (Chapter 5). In addition to discussion of nonlinear optical phenomena, a novel mechanism for electric dipole allowed fluorescence-detected circular dichroism will be introduced (Chapter 6). Tackling challenges associated with label-free chemically specific imaging, the construction of a novel infrared hyperspectral microscope for chemical classification in complex mixtures will be presented (Chapter 7). The thesis will conclude with a discussion of the inherent disadvantages in taking the traditional paradigm of modeling and measuring chemistry separately and provide the multi-agent consensus equilibrium (MACE) framework as an alternative to the classic meet-in-the-middle approach (Chapter 8). Spanning topics from pure theoretical descriptions of light-matter interaction to full experimental work, this thesis aims to unify these two fronts.

CHAPTER 1. INTRODUCTION

1.1 Imaging Methods for Characterizing Tissue

As an analytical tool, optical imaging methods provide a powerful nondestructive method of localizing and quantifying analytes. In biology, optical methods have a rich history, from the foundation of histology back in the 17th century.[1] Over the following centuries a vast number of approaches to enhance information obtained from optical imaging were developed. Most well-known among these methods is the process of histological staining, where sections of tissue are dyed with structure-targeting dyes, allowing optical transmittance microscopy to more easily differentiate subcellular structures. Foremost among these methods are silver staining for imaging neurons as well as hematoxylin and eosin staining for nuclei and collagen.[2-3] The ability to localize and determine structure of various tissue components, cell types, and organelles enabled modern biological understanding of many processes. In the present day these studies continue, with a greater emphasis on understanding exactly how disease pathologies affect tissue structure and function. Continued discovery in the field of biology hinges upon improved labeling and label-free imaging methods, enhanced methods for *in vivo* imaging, and further development in imaging speed to capture transient biological events.

Certain optical methods provide intrinsic advantages in imaging applications by probing chemical or macromolecular structure endogenously. While fluorescence is a powerful tool for biological study due to the ability to target specific proteins or cell-types through hybridization or dye-labeling, these approaches require nontrivial method development and sample preparation.[4-7] In contrast, modalities like Raman scattering, infrared absorbance, autofluorescence, and second and third harmonic generation provide optical contrast without the same constraints. In the case of second harmonic generation, the optical process itself is highly selective, requiring a noncentrosymmetric assembly for generation of signal.[8] The technique is intrinsically limited in information content compared to spectroscopic approaches, as measured signal by definition occurs only at the doubled frequency of the incident field. Improvements in information content can be made by leveraging the polarization dependence of this behavior, a strategy that can be extended to two-photon excited fluorescence measurements.[9] Section 1.2 below will describe some

fundamentals of nonlinear optics, while section 1.3 will introduce some fundamental concepts in polarization analysis.

The intrinsic advantage of label-free imaging is one reason methods developed in this thesis focus on second harmonic generation and infrared imaging modalities. Label-free imaging is critical in applications where measurement of *in vivo* tissue is desired, as in noninvasive disease-diagnostic efforts. However, several challenges are associated with *in vivo* measurements, particularly in the context of polarization-dependent optical measurements. Phototoxicity limits the laser peak power useable in imaging experiments and puts an effective cap on potential signal. Methods which improve signal-to-noise in beam-scanning microscopies, such as synchronous digitization, reduce the denominator in the signal to noise ratio and allow lower laser powers to be used for illumination.[10] Chapters 2 and 3 of this thesis focus on microscopy methods that suppress 1/f noise via rapid polarization modulation and spatial encoding of polarization information, respectively. In thick tissue sections and *in vivo* tissue measurements the scattering, birefringence, and diattenuation properties intrinsic to thick heterogeneous samples impede effective polarization analysis. Chapters 4 and 5 discuss theoretical frameworks to enable effective polarization analysis in the presence of unpolarized light induced by heterogeneous thick samples.

In addition to experimental difficulties associated with imaging in thick tissues and labeling procedures, there are considerable analytical challenges associated with measuring rapid biological processes. While both Raman and infrared absorbance provide label-free chemical specificity, the infrared absorbance cross-section is typically six orders of magnitude larger than Raman cross-sections. This provides an advantage in signal-to-noise, and consequently, speed. In imaging applications, Raman scattering has historically been preferred despite this signal advantage due to the ability to use visible wavelengths. Visible illumination can leverage the rich body of literature from optical microscopy and has an inherently smaller diffraction limit. Recent advances in IR microscopy have enhanced resolution by improving upon IR transparent refractive optics in addition to refining experimental methods like photothermal imaging.[11-12] Such microscopies are experimentally complex, however, motivating the research of alternative modalities that can utilize data science to merge high resolution visible contrast with chemical specificity of IR imaging. To handle the issue of imaging speed, sparse-sampling strategies can be implemented. Chapter 7 will

discuss the development of an IR hyperspectral microscope where both sparse sampling and image fusion between visible and IR are studied.

The ability to predict anticipated experimental outcomes is central to all of the analyses described above. Theoretical models that successfully anticipate experimental outcomes enable causal mechanistic understanding of the physical chemistry underpinning observables in analytical chemistry. As both the methods for probing chemistry and the chemistry itself increases in complexity, construction of these models can be increasingly difficult. The classical paradigm of conducting experimental measurements and theoretical analysis as separate efforts may in some cases hamstring successful research. Chapter 8 of this thesis will describe multi-agent consensus equilibrium (MACE) for the application of chemical structure determination, where empirically measured moments of inertia will directly influence theoretical structure prediction. Future studies can leverage MACE to fuse more complex models, such as predictions of X-ray diffraction pattern or cryo-electron microscopy micrographs, improving capacity to bridge experiment with theory.

1.2 Nonlinear Optics

A large portion of this thesis will describe theory and experiment directly related to 2nd order nonlinear optics. Put simply, 2nd order nonlinear optics comprises the variety of optical effects that scale quadratically with the electric field. Most commonly this refers to sum frequency generation. Sum frequency generation is the general case where two incident fields coherently scatter from a noncentrosymmetry structure, generating a single field at the sum frequency. This thesis will focus upon the specific case of sum frequency generation where the incident fields share the same frequency known as second harmonic generation, shown in **Figure 1.1**. Both SHG and two-photon absorption were experimentally demonstrated for the first time in 1961, shortly after the development of the laser by Theodore Maiman.[13-14] The development of the laser was critical for the discipline due to the quadratic scaling on the incident field. This quadratic dependence serves as both an advantage and a disadvantage, in effect limiting signal but providing intrinsic axial confinement required for biomedical imaging applications.[15] Both SHG and TPEF provide a secondary benefit in biomedical

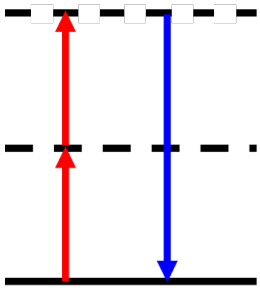

Figure 1.1 Jablonski diagram for SHG. Two incident photons coherently scatter from virtual states of a noncentrosymmetric structure, forming a single photon at the doubled frequency.

applications, allowing the use of near-IR illumination which can penetrate more deeply into tissue than visible wavelengths.[16]

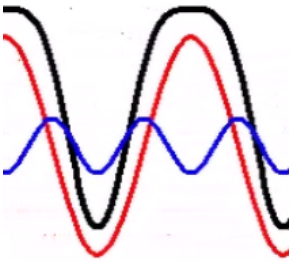

Figure 1.2 Plot of Energy or polarization versus time for electrons in an AC field.

To understand the utility of SHG as a contrast agent in imaging, it is useful to illustrate the fundamental origin of the NLO susceptibility and its relation to macroscopic observables. At the molecular level, SHG is described by the molecular hyperpolarizability. Taking the response of an electron cloud to an applied field as a Taylor series expansion, the hyperpolarizability is the second order term, i.e., it scales quadratically with the field. For the simple 1-dimensional case, the oscillatory motion of electrons in space follows an anharmonic potential. If the motion is plotted as energy versus time, corresponding to different positions within the trajectory, a flattened-out sine wave can be observed as shown in **Figure 1.2**. At the macroscopic scale, it is the coherent combination of molecular hyperpolarizabilities which governs overall nonlinear response. The presence of a center of inversion is analagous to flipping this 1D potential; generating a trace of energy versus time for this assembly results in a modulation 180˚ out of phase with the original. Consequently, assemblies of hyperpolarizable molecules with a center of inversion do not result in observable SHG due to destructive interference of the second harmonic. This symmetry selection rule makes SHG a powerful tool for measuring trace quantities of chiral crystals, allowing early protein crystal detection and detection of trace crystallinity in amorphous pharmaceutical formulations.[17] In biomedical imaging SHG enables highly selective imaging of collagen, microtubules, and myosin frameworks, which exhibit the correct symmetry to radiate SHG.[17]

Polarization analysis can further improve the value of SHG and TPEF as analytical tools. Intrinsically, SHG is a low-information measurement. The detection of SHG signal corresponds only to whether or not a noncentrosymmetric structure is present, but does not allow facile distinction between multiple SHG-active materials. Changes in intensity that could be attributed to the presence of multiple SHG-active materials could also be caused by orientation effects or the variations in . By leveraging the intrinsic polarization dependence of SHG, distinction between materials can be made. Even chemically identical crystal polymorphs can be distinguished using

polarization analysis.[18] In contrast to SHG, TPEF does provide an intrinsic method to separate fluorophores, either by varying excitation wavelength or by detecting the fluorescence spectrum rather than just the integrated intensity. The use of polarization dependence provides an additional analytical tool, however, informing upon local orientation of fluorophores.[19] This has potential application in protein structure determination where amorphous protein aggregates can be difficult to distinguish from protein crystals.

1.3 Polarization Analysis

Polarization analysis for linear and nonlinear optics enables recovery of structural parameters relating to the interaction of light with propagating optical fields. The simplest mathematical framework describing these interactions is the Jones framework, where fields are tracked with the Jones vector, a two element vector containing the relative amplitude and phase of the orthogonal field components. Equation (1.1) below defines the Jones vector, with the orthogonal field components denoted as H and V for horizontal and vertical.

$$\vec{e} = \begin{bmatrix} H \\ V \end{bmatrix} = \begin{bmatrix} |H| \\ |V| e^{i\phi} \end{bmatrix} \tag{1.1}$$

The definition of the Jones vector does not support the description of partially or wholly unpolarized light; future chapters will discuss the Stokes-Mueller calculus as an alternative and outline methods to bridge the generality of the Stokes vector with the intuitive nature of the Jones framework for interpreting the resulting measurements. Nondepolarizing linear processes involving the Jones vector can be represented by the product of the Jones vector and a square Jones matrix representing the optic in question, e.g, polarizers, waveplates, and mirrors.

$$\vec{e}_{out} = J \cdot \vec{e}_{in} \tag{1.2}$$

Second order nonlinear optical processes, such as two-photon excited fluorescence, sum frequency generation, and second harmonic generation require the interaction of multiple incident fields. Consequently, the optical process is modeled as a tensor product between the incident fields and the nonlinear optical susceptibility describing the change in phase and amplitude associated with

the NLO process. Equation (1.3) shows the general process of SFG, of which SHG is a special case.

$$\vec{e}^{\omega_{sum}} = \chi^{(2)} : \vec{e}^{\omega_1}\vec{e}^{\omega_2} \tag{1.3}$$

1.4 Thesis Overview

The focus of this dissertation is on the intersection between analytical methods development and theoretical approaches to model those measurements. Particular emphasis is placed upon polarization-dependent nonlinear optics, which provides additional structural information relative to intensity information alone.

Chapter 2 will provide a detailed overview of the Jones framework for polarization analysis applied to SHG. The macromolecular nonlinear susceptibility of collagen was modeled using a combination of *ab initio* chemical predictions of the model nucleic acid N-methylacetamide. Predictions from this model suggested a macromolecular susceptibility highly aligned along the collagen backbone. A method for video-rate NLO susceptibility tensor imaging termed nonlinear optical stokes ellipsometry (NOSE) will be described and applied to imaging collagenous tissues including porcine skin, ear, and mouse tail. The basis of this approach is in synchronizing an electro-optic modulator (EOM) with the laser of the microscope, such that ten images with unique polarization states incident to the sample are recorded at a time. Tensor imaging enabled the recovery of local collagen orientation as well, with detailed analysis of the polar tilt angle suggesting a bimodal distribution of collagen orientations within the tissue samples measured.

Chapter 3 will provide an alternative approach to NOSE microscopy, which substitutes a single fixed optic in the rear conjugate plane of the microscope for the EOM. The microretarding array is a simple thin film of birefringent liquid crystal sandwiched between glass windows. The fast axis of the birefringent media is rotated linearly across one axis of the optic, revealing a cosine modulated intensity pattern when imaged through a polarizer. When placed in the rear-conjugate plane this optic encoded varying polarization state across the field of view. Coupled with translation hardware common to most commercial microscopes, a series acquisition of several images enabled per-pixel NLO susceptibility tensor element mapping of collagenous thin tissues. Snapshot or shotgun polarimetry was achieved for SHG analysis of systems containing a single

SHG-active material by pooling intensities within the field of view and accounting for orientation differences via image analysis. This approach was applied both to thin Z-cut quartz samples and thin sections of mouse-tail tendon. In addition to SHG polarization analysis the power of this tool for differentiating amorphous and crystalline protein aggregates will be discussed. The patterned polarization within the image enabled data analysis in the Fourier domain. Fourier transforming the cosine pattern yielded a double-delta function in the Fourier domain, from which the Fourier coefficients that predict SHG and TPEF intensity as a function of incident polarization were extracted. Comparisons between the translation real-space analysis, snapshot approaches, and Fourier domain analysis will be discussed.

Chapter 4 will explore the consequences of imaging thick turbid systems on polarization analysis. Thick biological samples, exhibiting depths of greater than 10 μm, exhibit significant changes in refractive index as a function of position due to the presence of organelles and subcellular structures, as well as heterogeneity induced by a diverse population of cell types. Consequently, as light propagates through thick tissue, either in a section or for *in vivo* biological imaging, light at different positions along the plane orthogonal to the optical axis experiences unique phase shifts, birefringence effects, and scattering. Ultimately this results in depolarization of the beam, influencing detected intensity in NLO measurements such as SHG. In many measurements reported previously the nonballistic light which is incident to the sample plane has been neglected from polarization analysis. However, it is not trivially proven that neglecting the scattered and depolarized light is appropriate. In order to predict SHG behavior in such complex polarization scenarios, a theoretical framework connecting the intuitive Jones framework for mapping physical observables to the more general Stokes-Mueller framework for interpreting polarization states was developed. This framework is described in detail in Chapter 4 and tested in the extreme case of complete depolarization by placing a microretarding array in the Fourier plane of a beam-scanning NLO microscope. Theoretical predictions of SHG polarization dependence from this framework for Z-cut quartz anticipated unpolarized SHG when probed with unpolarized light, in excellent agreement with experimental measurements. Thin sections of collagenous mouse tail were then imaged using unpolarized incident laser light, enabling NLO susceptibility tensor imaging with recovery of local azimuthal and polar orientation from polarization analysis of the emitted SHG.

Chapter 5 will discuss the application of the theoretical framework described in Chapter 4 to thick tissue sections, where depolarization is induced by the sample and not by an optic integrated into the microscope. An instrument for imaging the Stokes vectors of both the transmitted laser and SHG emitted will be described. The instrument was used to image sections of collagenous mouse tail varying in thickness from 5 to 70 μm. Effects of depolarization and birefringence on the laser beam will be discussed. The nuanced interaction between collagen orientation and polarization of emitted SHG will also be examined, which can result in SHG either more or less polarized than the incident laser light.

Chapter 6 will take a departure from the discussion of nonlinear optics to explore polarization dependence in linear optics – in particular, fluorescence emission for uniaxial assemblies of chiral molecules. Work published by Barnes and coworkers reported an astoundingly large fluorescence detected circular dichroism from helicene.[20] Despite being reported in 2006, the precise mechanism of such a large dichroism was not clear, as the magnitude of the effect is inconsistent with a magnetic-dipole coupled mechanism that is commonly understood to govern electronic circular dichroism. This chapter will provide an alternate mechanism, which may give rise to electric-dipole allowed circular dichroism detected by fluorescence, coined fluorescence optical rotary dispersion (F-ORD).

Chapter 7 continues the focus on linear optics, describing the construction of a hyperspectral infrared microscope with a QCL-array laser source. Quantum cascade lasers provide high peak-power illumination in the infrared, and the flexible array architecture enabled rapid switching between wavelength channels with arbitrary patterning. The utility of infrared imaging is often hampered by slow speeds necessary with sample-scanned FTIR approaches and diffraction-limited resolution on the order of 5 μm. This chapter aims to address both of these challenges by leveraging sparse sampling techniques enabled by the QCL array and coupling a copropagating visible laser for digital merging of high-resolution optical images with the spectral information inherent to IR absorbance.

In the final chapter of this thesis a method for model fusion called Multi-Agent Consensus Equilibrium (MACE) will be discussed. Historically, physical chemistry has been conducted with theoreticians and experimentalists working from opposite ends of the same problem. Often, an

experimental outcome is observed, and theory is generated as a separate endeavor. This is most readily observed in structure determination problems, such as cold ion gas phase spectroscopy where the measured spectrum is intimately tied to molecular conformation. In these studies it is common to simulate many possible conformations with *ab initio* chemical methods and then to match the correct spectra to the experimental outcome, discerning structure. An alternative paradigm is proposed, whereby the experimental measurement can act as a constraint on structure determination by purely theoretical methods. Development of MACE for application to structural elucidation in chemistry will be discussed, with initial studies constraining molecular structure to empirical measurements of the inertia tensor for several small molecules. This chapter concludes the thesis, illustrating the complex intersection of theory and experiment for optically-probed chemical physics.

1.5 References

1. Bracegirdle, B., The History of Histology: A Brief Survey of Sources. *History of Science* **1977,** *15* (2), 77-101.

2. Titford, M., The long history of hematoxylin. *Biotechnic & Histochemistry* **2005,** *80* (2), 73-78.

3. Switzer, R. C., 3rd; Merril, C. R.; Shifrin, S., A highly sensitive silver stain for detecting proteins and peptides in polyacrylamide gels. *Anal Biochem* **1979,** *98* (1), 231-237.

4. Swiger, R. R.; Tucker, J. D., Fluorescence in situ hybridization: A brief review. *Environmental and Molecular Mutagenesis* **1996,** *27* (4), 245-254.

5. Phillips, R. B.; Reed, K. M., Application of fluorescence in situ hybridization (FISH) techniques to fish genetics: a review. *Aquaculture* **1996,** *140* (3), 197-216.

6. Ntziachristos, V.; Ripoll, J.; Wang, L. V.; Weissleder, R., Looking and listening to light: the evolution of whole-body photonic imaging. *Nature Biotechnology* **2005,** *23* (3), 313-320.

7. Bornhop, D.; Contag, C.; Licha, K.; Murphy, C., Advances in contrast agents, reporters, and detection. *Journal of Biomedical Optics* **2001,** *6* (2).

8. Boyd, R. W., *Nonlinear Optics, Third Edition*. Academic Press, Inc.: 2008.

9. Simpson, G. J., *Nonlinear Optical Polarization Analysis in Chemistry and Biology*. Cambridge University Press: Cambridge, 2017.

10. Muir, R. D.; Sullivan, S. Z.; Oglesbee, R. A.; Simpson, G. J., Synchronous digitization for high dynamic range lock-in amplification in beam-scanning microscopy. *Review of Scientific Instruments* **2014,** *85* (3), 033703.

11. Harada, M.; Iwamoto, K.; Kitamori, T.; Sawada, T., Photothermal microscopy with excitation and probe beams coaxial under the microscope and its application to microparticle analysis. *Analytical Chemistry* **1993,** *65* (20), 2938-2940.

12. Bhargava, R., Infrared Spectroscopic Imaging: The Next Generation. *Appl. Spectrosc.* **2012,** *66* (10), 1091-1120.

13. Franken, P. A.; Hill, A. E.; Peters, C. W.; Weinreich, G., Generation of Optical Harmonics. *Physical Review Letters* **1961,** *7* (4), 118-119.

14. Kaiser, W.; Garrett, C. G. B., Two-Photon Excitation in CaF_2:Eu^{2+}. *Physical Review Letters* **1961,** *7* (6), 229-231.

15. Zipfel, W. R.; Williams, R. M.; Webb, W. W., Nonlinear magic: multiphoton microscopy in the biosciences. *Nature Biotechnology* **2003,** *21* (11), 1369-1377.

16. Xu, C.; Zipfel, W.; Shear, J. B.; Williams, R. M.; Webb, W. W., Multiphoton fluorescence excitation: new spectral windows for biological nonlinear microscopy. *Proceedings of the National Academy of Sciences* **1996,** *93* (20), 10763.

17. Correa-Soto, C.; Trasi, N. S.; Schmitt, P. D.; Su, Y.; Liu, Z.; Miller, E.; Variankaval, N.; Marsac, P. J.; Simpson, G. J.; Taylor, L. S., Second harmonic generation microscopy as a tool for the early detection of crystallization in spray dried dispersions. *Journal of Pharmaceutical and Biomedical Analysis* **2017,** *146*, 86-95.

18. Schmitt, P. D.; DeWalt, E. L.; Dow, X. Y.; Simpson, G. J., Rapid Discrimination of Polymorphic Crystal Forms by Nonlinear Optical Stokes Ellipsometric Microscopy. *Analytical Chemistry* **2016,** *88* (11), 5760-5768.

19. Shternin, P. S.; Gericke, K.-H.; Vasyutinskii, O. S., The polarisation of two-photon excited fluorescence in rotating molecules. *Molecular Physics* **2010,** *108* (7-9), 813-825.

20. Hassey, R.; Swain, E. J.; Hammer, N. I.; Venkataraman, D.; Barnes, M. D., Probing the Chiroptical Response of a Single Molecule. *Science* **2006,** *314* (5804), 1437-1439.

CHAPTER 2. IMAGING THE NONLINEAR SUSCEPTIBILITY TENSORS OF COLLAGEN BY NONLINEAR OPTICAL STOKES ELLIPSOMETRIC MICROSCOPY

The contents of this chapter are adapted from the publication Imaging the Nonlinear Susceptibility Tensor of Collagen by Nonlinear Optical Stokes Ellipsometry, originally published in *Biophysical Journal* in 2016.[1]

2.1 Introduction

Second harmonic generation (SHG) microscopy has been used for the structural characterization of myosin, collagen and microtubule organizations for nearly two decades.[2] SHG has provided an attractive alternative to linear optical methods due to the ability to use near IR excitation which penetrates deeply into thick tissue samples and mitigates sample damage. As an instantaneous coherent phenomenon, SHG does not suffer from photobleaching that comparable multiphoton absorption and fluorescence techniques are plagued by. Furthermore, SHG methods are often devoid of an exogenous labelling agents, although previous reports have noted marked improvement in signal strength and background suppression through the use of dyes.[3]

Collagen is the most abundant structural element of the extracellular matrix (ECM) and methods for imaging collagen structure are consequently critical to tissue engineering efforts.[4] Disruptions in native collagen structure are correlated with pathogenesis; degree of supramolecular order has been utilized previously to study the microscopic effects of muscular dystrophy and osteogenesis imperfecta.[5, 6] Disruption of collagen order has also been correlated with non-small cell lung carcinoma and breast cancers through tissue stiffening via collagen crosslinking in the ECM.[7, 8] Probes which can span both molecular scale information and long-range structure at the tissue scale provide a key tool in potential diagnostic methods and may provide further insight on how pathogenic states affect cellular growth and metabolism. Consequently, spectroscopic imaging methods which can locally probe tissue structure, such as SHG, neatly fill the role of informing upon structure across length scales from sub-micron to tens of microns. Polarization analysis

provides information regarding macromolecular structure at the single-pixel level in SHG microscopy experiments, while the full image informs upon larger length scales.

Detection of second harmonic generation is a measurement containing only one observable: intensity. Despite this inherent limitation, previous works have explored the ability to improve information content by utilizing the polarization-dependence of the phenomenon. SHG measurements which directly access the hyperpolarizability tensor describing the second order response of a system's electron cloud to applied electric field have the capacity to recover a greater number of structural parameters than comparable linear optical techniques as the tensor may contain up to 18 unique elements. The use of polarization as a handle to increase information content in SHG microscopy is well founded. [9-11] Initial efforts were limited by large 1/f noise contributions due to the long measurement time associated with manual rotation of polarization optics. Recent advances in polarization controlling electronics enabled development of techniques like nonlinear optical Stokes ellipsometric microscopy which greatly reduce 1/f noise contribution.[12] In this chapter the application of NOSE microscopy to collagen is discussed.

In this chapter, the mathematical framework used for polarization analysis of SHG is described and applied to the model system of Z-cut quartz, which exhibits no birefringence and a well-characterized nonlinear optical susceptibility. To enhance signal-to-noise by suppressing the 1/f noise associated with polarization-modulation by rotating fixed optics, a microscope leveraging an electro-optic modulator for rapid polarization modulation is described. This approach is coined nonlinear optical Stokes ellipsometric microscopy (NOSE). The nonlinear optical susceptibility of collagen is predicted using the symmetry additive model, and predictions are contrasted with tensor element images obtained from NOSE microscopy. The contents of this chapter are adapted from my first publication during my Ph.D., "Imaging the Nonlinear Susceptibility Tensor of Collagen by Nonlinear Optical Stokes Ellipsometry".[1]

2.2 Theoretical Foundation

2.2.1 Nonlinear Optical Susceptibility and Detected Intensity

The NLO susceptibilty is the experimental observable in NLO microscopy accessible via polarization analysis, and is constructed from the macromolecular ensemble response of the molecular hyperpolarizability. Fundamentally, the susceptibility determines the polarization and amplitude of outgoing fields, given a polarization and amplitude of fields incident to the sample. The preceding notation is general for sum frequency generation, but will be applied in this chapter to the specific case of SHG, where both incident fields are of the same freqeuncy ($\omega^1 = \omega^2$). In the Cartesian frame, the nonlinear optical susceptibility formally contains 27 potentially unique elements, corresponding to a $3\times3\times3$ tensor. For SHG, the order of the incident fields is interchangeable by symmetry, reducing the number of unique nonzero elements to 18. Modeling NLO processes in the Jones framework involves the projection of the susceptibility onto the plane normal to the axis of propagation. The corresponding Jones tensor, $\chi_J^{(2)}$ is a $2\times2\times2$ structure, with 6 potential unique nonzero elements for SHG. For convenience in stacking multiple measurements it is often useful to vectorize the Jones tensor as $\vec{\chi}_J$. Equation (2.1) below illustrates how to model the process of SHG as a linear algebraic process.

$$\vec{e}^{\,sum} = E \cdot \vec{\chi}_J = \left(\begin{bmatrix} 1 & 0 \\ 0 & 1 \end{bmatrix} \otimes \vec{e}^{\,\omega_1} \otimes \vec{e}^{\,\omega_2} \right)^T \cdot \vec{\chi}_J \tag{2.1}$$

The Kronecker product of incident fields ($e^{\omega_1} \otimes e^{\omega_2}$) can be expanded to illustrate precisely how each component of the incident light interacts with the vectorized Jones tensor.

$$\vec{e}^{\,\omega_{sum}} = \begin{bmatrix} e_H^{\omega_1} e_H^{\omega_2} & e_H^{\omega_1} e_V^{\omega_2} & e_V^{\omega_1} e_H^{\omega_2} & e_V^{\omega_1} e_V^{\omega_2} & 0 & 0 & 0 & 0 \\ 0 & 0 & 0 & 0 & e_H^{\omega_1} e_H^{\omega_2} & e_H^{\omega_1} e_V^{\omega_2} & e_V^{\omega_1} e_H^{\omega_2} & e_V^{\omega_1} e_V^{\omega_2} \end{bmatrix} \cdot \begin{bmatrix} \chi_{HHH} \\ \chi_{HHV} \\ \chi_{HVH} \\ \chi_{HVV} \\ \chi_{VHH} \\ \chi_{VHV} \\ \chi_{VVH} \\ \chi_{VVV} \end{bmatrix} \tag{2.2}$$

Measured SFG signal is detected as intensity, corresponding to the product of the sum frequency's conjugate transpose with itself. The field vector shown in equation (2.2) consequently results in a sum of 16 terms, 5 of which are unique. Intensity of SFG emitted when modulating polarization incident to the sample, either via polarization rotation or modulated phase retardance (Δ), can be modeled as a sum of trigonometric functions weighted by these 5 Polynomial coefficients. Equation (2.3) shows the Polynomial function for phase retardance.

$$I_n^{2\omega}\left(\frac{\Delta}{2}\right) = A\cdot\cos^4\left(\frac{\Delta}{2}\right) + B\cdot\cos^3\left(\frac{\Delta}{2}\right)\cdot\sin\left(\frac{\Delta}{2}\right) + C\cdot\cos^2\left(\frac{\Delta}{2}\right)\cdot\sin^2\left(\frac{\Delta}{2}\right) + D\cdot\cos\left(\frac{\Delta}{2}\right)\cdot\sin^3\left(\frac{\Delta}{2}\right) + E\cdot\sin^4\left(\frac{\Delta}{2}\right) \quad (2.3)$$

For polarized detection of the NLO signal, the measured intensity can be predicted from the Jones tensor. A 5×16 matrix can be used to map the 16 tensor element products to the corresponding coefficients, or alternatively a simplified 5×9 matrix accounting for nonunique products known as P can be used. Equation (2.4) shows P and the unique tensor products corresponding to the set of Polynomial coefficients $\vec{A}$.

$$\begin{bmatrix} A \\ B \\ C \\ D \\ E \end{bmatrix}_n = P\cdot\begin{bmatrix} \chi^*_{nHH}\chi_{nHH} \\ \chi^*_{nHH}\chi_{nHV} \\ \chi^*_{nHH}\chi_{nVV} \\ \chi^*_{nHV}\chi_{nHH} \\ \chi^*_{nHV}\chi_{nHV} \\ \chi^*_{nHV}\chi_{nVV} \\ \chi^*_{nVV}\chi_{nHH} \\ \chi^*_{nVV}\chi_{nHV} \\ \chi^*_{nVV}\chi_{nVV} \end{bmatrix}_L = \begin{bmatrix} 1 & 0 & 0 & 0 & 0 & 0 & 0 & 0 & 0 \\ 0 & 2 & 0 & 2 & 0 & 0 & 0 & 0 & 0 \\ 0 & 0 & 1 & 0 & 4 & 0 & 1 & 0 & 0 \\ 0 & 0 & 0 & 0 & 0 & 2 & 0 & 2 & 0 \\ 0 & 0 & 0 & 0 & 0 & 0 & 0 & 0 & 1 \end{bmatrix}\begin{bmatrix} \chi^*_{nHH}\chi_{nHH} \\ \chi^*_{nHH}\chi_{nHV} \\ \chi^*_{nHH}\chi_{nVV} \\ \chi^*_{nHV}\chi_{nHH} \\ \chi^*_{nHV}\chi_{nHV} \\ \chi^*_{nHV}\chi_{nVV} \\ \chi^*_{nVV}\chi_{nHH} \\ \chi^*_{nVV}\chi_{nHV} \\ \chi^*_{nVV}\chi_{nVV} \end{bmatrix}_L \quad (2.4)$$

The polynomial coefficients provide a convenient method for interpreting the polarization dependence of detected intensity via the reduction in total number of observables describing the tensor product. Furthermore, the explicit contribution of underlying tensor elements to each coefficient can be evaluated. Equation (2.5) below illustrates the tensor element contribution to the polynomial coefficients.[13]

$$
\begin{aligned}
A_n &= \left|\chi^{(2)}_{nHH}\right|^2 \\
B_n &= -4\cdot \mathrm{Im}\left[\chi^{(2)}_{nHH}\cdot\chi^{(2)\,*}_{nVH}\right] \\
C_n &= 4\cdot\left|\chi^{(2)}_{nVH}\right|^2 - 2\cdot \mathrm{Re}\left[\chi^{(2)}_{nHH}\cdot\chi^{(2)\,*}_{nVV}\right] \\
D_n &= 4\cdot \mathrm{Im}\left[\chi^{(2)}_{nVV}\cdot\chi^{(2)\,*}_{nVH}\right] \\
E_n &= \left|\chi^{(2)}_{nVV}\right|^2
\end{aligned}
\tag{2.5}
$$

It is noteworthy that equation (2.3) is quartic in terms of some of the trigonometric functions; consequently, nonlinear fits to optimize intensity predicted as a function of Δ often carry a high uncertainty and covariance between recovered Δ. An alternative equation predicting intensity from the fundamental and second harmonic frequencies of Δ can reduce some uncertainty in the nonlinear fit, shown below.

$$
I_n^{2\omega}(\gamma) = a + b\cos(2\Delta) + c\cos(\Delta) + d\sin(\Delta) + e\sin(2\Delta) \tag{2.6}
$$

Mapping between the Polynomial coefficients $\vec{A}$ and the Fourier coefficients $\vec{a}$ in equation (2.6) is achieved via the linear transform T.

$$
\begin{bmatrix} a \\ b \\ c \\ d \\ e \end{bmatrix}_n = T\cdot\begin{bmatrix} A \\ B \\ C \\ D \\ E \end{bmatrix} = \frac{1}{8}\begin{bmatrix} 3 & 0 & 1 & 0 & 3 \\ 1 & 0 & -1 & 0 & 1 \\ 4 & 0 & 0 & 0 & -4 \\ 0 & 2 & 0 & 2 & 0 \\ 0 & 1 & 0 & -1 & 0 \end{bmatrix}\cdot\begin{bmatrix} A \\ B \\ C \\ D \\ E \end{bmatrix}_n \tag{2.7}
$$

2.2.2 Reference Frame Rotations

The preceding section has omitted discussion of any deviation in reference frame between the sample of interest and the laboratory reference frame defined by the instrument. Ordered materials, like those active for SHG and SFG, will display varying behaviors in intensity as a function of polarization according to their orientation with respect to the laboratory frame. Furthermore, any optical components within the beam path will also have a rotation defined by their orientation with respect to the laboratory frame. Accounting for the resulting intensity variation is rather

straightforward in principal but requires bookkeeping of all optical components and potentially adds in additional unknown parameters with respect to sample orientation.

The rotation between two reference frames can be achieved via the projection of each unique coordinate in one frame onto the other. The Euler angles θ, ϕ, and ψ defining the rotation correspond to the polar tilt, azimuthal, and twist. Through the remainder of this thesis the set of primed coordinates x'y'z' will refer to the local reference frame relative to the sample. **Figure 2.1** illustrates the effect of each Euler angle in rotating the local reference from the laboratory reference.

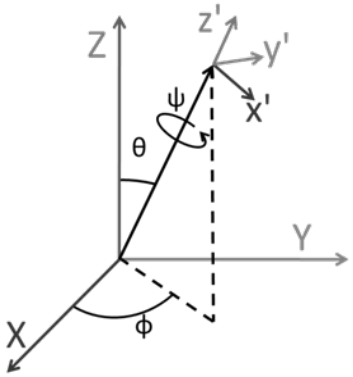

Figure 2.1 Depiction of the Euler angles involved in rotating a point from the x'y'z' coordinate system to the XYZ coordinate system or vice versa. ϕ is the azimuthal angle, θ is the polar angle, and ψ is the twist angle.

It is worth briefly discussing the difference between extrinsic and intrinsic rotations. Typically, in polarization analysis the optic or structure in question is rotated from the local frame to the laboratory frame. In this context, the projection operation onto the laboratory frame corresponds to extrinsic rotation. When track the polarization effects of multiple objects in the beam path, interaction with a given optic should be succeeded by intrinsic rotation to return the field to the original reference frame. Subsequent optics can then be treated by extrinsic rotation, operation with their corresponding Jones matrix, and intrinsic rotation. This procedure for Jones matrices is naturally extended to Jones tensors, as described in Equation (2.8).

$$\begin{aligned}
&\vec{\chi}_J = \boldsymbol{R}_{\theta\phi\psi} \cdot \vec{\chi}_l \\
&\boldsymbol{R}_{\theta\phi\psi} = R_{\theta\phi\psi} \otimes R_{\theta\phi\psi} \otimes R_{\theta\phi\psi} \\
&R_{\theta\phi\psi} = \begin{bmatrix} \cos\phi & -\sin\phi & 0 \\ \sin\phi & \cos\phi & 0 \\ 0 & 0 & 1 \end{bmatrix} \begin{bmatrix} \cos\theta & 0 & \sin\theta \\ 0 & 1 & 0 \\ -\sin\theta & 0 & \cos\theta \end{bmatrix} \begin{bmatrix} \cos\psi & -\sin\psi & 0 \\ \sin\psi & \cos\psi & 0 \\ 0 & 0 & 1 \end{bmatrix}
\end{aligned} \tag{2.8}$$

The NLO susceptibility in the local reference frame will be referred to as $\chi_l^{(2)}$ or $\vec{\chi}_l$, depending upon whether it is vectorized or not. The laboratory frame Jones tensor will be referred to as $\chi_J^{(2)}$ or $\vec{\chi}_J$. In the Jones frame, defined by the projection of the Cartesian laboratory frame onto the objective plane of the microscope, $\boldsymbol{J}_{\theta\psi\phi}$ simplifies to a projection on two dimensions. Following

any necessary reference frame rotations, the detected intensity in the Jones frame can be deduced by multiplication of the 2×3 projection matrix I_J defined below.

$$I_J = \begin{bmatrix} 1 & 0 & 0 \\ 0 & 1 & 0 \end{bmatrix} \tag{2.9}$$

Incorporating equations (2.8) and (2.9), a single rotation matrix $\boldsymbol{J}_{\theta\phi\psi}$ can be constructed.

$$\begin{aligned} \boldsymbol{J}_{\theta\phi\psi} &= \left(I_J \cdot R_{\theta\phi\psi}\right) \otimes \left(I_J \cdot R_{\theta\phi\psi}\right) \otimes \left(I_J \cdot R_{\theta\phi\psi}\right) \\ &= \left(\begin{bmatrix} 1 & 0 & 0 \\ 0 & 1 & 0 \end{bmatrix} \otimes \begin{bmatrix} 1 & 0 & 0 \\ 0 & 1 & 0 \end{bmatrix} \otimes \begin{bmatrix} 1 & 0 & 0 \\ 0 & 1 & 0 \end{bmatrix} \right) \cdot \left(R(\theta,\phi,\psi) \otimes R(\theta,\phi,\psi) \otimes R(\theta,\phi,\psi) \right) \end{aligned} \tag{2.10}$$

2.2.3 Symmetry and Parameter Reduction

While the Jones frame NLO susceptibility may contain only 8 elements, symmetry can often constrain this to a lesser number, reducing uncertainty in the measured parameters. For the specific case of SHG, for example, the interchangeability of the two incident fields reduces the number of potential unique nonzero elements to 6, or from 27 to 18 in the Cartesian frame. Local symmetry of the sample can further reduce the number of parameters by constraining some elements of the susceptibility to be equivalent. Nonlinear fits directly to the unique nonzero elements can be achieved by incorporating a symmetry matrix Q, which maps unique nonzero tensor elements contained in the primed $\vec{\chi}_l'$, to the full $\vec{\chi}_l$ susceptibility.

$$\vec{\chi}_l = Q \cdot \vec{\chi}_l' \tag{2.11}$$

Combining equations (2.1) with equation (2.10) and (2.11) yields equation (2.12), accounting for polarization changes both from symmetry and orientation effects.

$$\vec{e}^{\,\omega_{sum}} = E \cdot \boldsymbol{J}_{\theta\phi\psi} \cdot Q \cdot \vec{\chi}_l' \tag{2.12}$$

2.3 Modeling the Hyperpolarizability of Collagen

With the foundation for polarization analysis laid in section 2.2, considering the origin of second harmonic generation from a physical perspective will provide necessary context for interpreting subsequent measurements. At the molecular level it is the second order response of the valence

electrons to an applied field that generates the second harmonic. The hyperpolarizability tensor $\beta^{(2)}$ describes the change in polarization as a function of the second order of the field. In the Cartesian reference frame this hyperpolarizability is a $3\times3\times3$ tensor, where the last two indices map the polarization of the applied field and the first index maps the induced polarization. This structure is identical to the NLO susceptibility at the macromolecular scale.

Collagen is composed of a macromolecular assembly of tropocollagen molecules, largely composed of proline, glycine, and hydroxyproline. Tropocollagen is a triple helix of three polypeptide strands typically extending 300 nm in length and approximately 1.5 nm in diameter. Previous theoretical studies have reported the nonlinear optical response of tropocollagen to be dominated by the peptide backbone response. The overall hyperpolarizability is in large part contributed by the amide moiety connecting adjacent amino acids. Aromatic residues typically exhibit large hyperpolarizabilities as well, in accordance with the highly delocalized π electrons, but their abundance in collagen is low. Leveraging the assumption that the dominant contribution to the hyperpolarizability is the polyamide backbone, the tropocollagen molecular response can be predicted. Furthermore, far from resonance coupling between adjacent amide moieties is anticipated to be small, which suggests that quantum chemical calculations can be conducted upon the smallest building block of the tropocollagen molecule – the amide linkage itself. Using the model amino acid N-methyl acetamide (NMA) as a stand-in for individual residues, the total tropocollagen hyperpolarizability can be built from the coherent summation of monomers using the symmetry additive model.[14-16] **Figure 2.2** illustrates the additive behavior of the hyperpolarizability tensor of collagen, built up from monomeric NMA to tropocollagen helices. Tropocollagen assembles into fibrils, and fibrils further assemble into fibers, giving rise to the macromolecular susceptibility detectable in the laboratory frame of measurement.

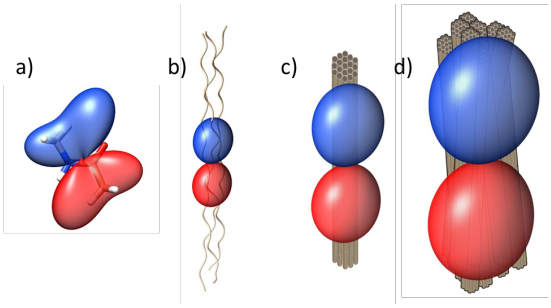

Figure 2.2 Hyperellipsoid representation of hyperpolarizability tensor of a) NMA b) a collagen triple helix c) a collagen fibril and d) the second order susceptibility tensor of collagen, which exhibits a distribution in fibril tilt angles.

In brief, the approach takes the hyperpolarizability tensor of each monomer and translates and rotates the tensor according to each monomer's position in the peptide structure. The cumulative

effect is an orientational average of the individual monomer's hyperpolarizability according to the orientations sampled within the peptide.

2.3.1 Connecting the Macromolecular and Laboratory Reference Frames

Formally, the macromolecular NLO susceptibility can have 27 unique nonzero elements in the Cartesian frame. Symmetry, as described in section 2.2.3, provides the means to further reduce this number for collagen. Considering local C_∞ symmetry about the central fiber axis, several equalities emerge, yielding seven unique tensor elements: $\chi_{zxx} = \chi_{zyy}$, $\chi_{xzx} = \chi_{yzy}$, $\chi_{xxz} = \chi_{yyz}$, $\chi_{xyz} = -\chi_{yxz}$, $\chi_{yzx} = -\chi_{xzy}$, $\chi_{zxy} = -\chi_{zyx}$, and χ_{zzz}. Considering the symmetry of the process of SHG itself further reduces the number of unique nonzero elements to four, as the incident fields are interchangeable. This yields the equalities: $\chi_{zxx} = \chi_{zyy}$, $\chi_{xzx} = \chi_{yzy} = \chi_{xxz} = \chi_{yyz}$, $\chi_{xyz} = -\chi_{yxz} = -\chi_{yzx} = \chi_{xzy}$. The symmetry matrix Q described in equation (2.11) provides the means to map from the remaining unique elements shown in (2.13) to the local frame vectorized NLO susceptibility.

$$\vec{\chi}_l = Q \cdot \begin{bmatrix} \chi_{xyz} \\ \chi_{yyz} \\ \chi_{zyy} \\ \chi_{zzz} \end{bmatrix} \tag{2.13}$$

The resulting local frame tensor is connected to the laboratory frame via the procedure described in section 2.2.2, and subsequently projected into the Jones frame during measurement. It is not immediately clear from the preceding theory how the local susceptibility arises from the molecular hyperpolarizability, however. In much the same way that the symmetry additive model builds the tropocollagen hyperpolarizability by summing the individual contributions of the NMA building blocks, the macromolecular response corresponds to the orientationally averaged molecular response. This is the origin of differing NLO susceptibilities for polymorphs of the same chemical and provides the mechanism by which polarization dependent SHG informs upon local collagen structure. As the distribution of orientations from individual tropocollagen monomers changes, so too does the macromolecular observable response.

2.3.2 Methods for Modeling NLO Activity of Collagen

The nonlinear optical polarizability of NMA was modeled via several quantum chemical methods. All quantum chemical calculations were performed with GAMESS (Version May.01.2014.R1) using the 6-311++G** basis set.[17] Initial NMA geometry was optimized using density functional theory with the B3LYP functional.[18] The time-dependent hyperpolarizability was then computed for an optical field of 800 nm using time-dependent Hartree-Fock (TD-HF) and time-dependent DFT (TD-DFT).[19] Several functionals were used to compute the time-dependent hyperpolarizability, including the long-range corrected Becke 88 exchange functional with Lee Yang Parr correlation functional (LC-BLYP) and Becke 88 exchange with one parameter progressive correlation (LC-BOP).[20] Range corrected functionals were implemented to reduce the effects of the local density approximation on computed hyperpolarizabilities.[21] The collagen-like peptide $(Pro\text{-}Pro\text{-}Gly)_{10}$ (Protein Data Bank ID 1K6F, PPG) was utilized as a model of the tropocollagen triple-helix, further simplifying the modeling procedure.[22, 23] Lastly, the symmetry additive model was applied and the monomeric amide linkage hyperpolarizabilities summed to generate the PPG response using NLOPredict in Chimera.[14, 22, 24]

2.4 Experimental Methods

2.4.1 Sample Preparation

The Purdue University Center for Cancer Research's Transgenic Mouse Core Facility provided mouse tails under Purdue Animal Care and Use Committee protocol 1111000314. Prof. Jonathan Wilker (Purdue University, West Lafayette, IN) provided porcine skin and ear samples; samples were obtained from the surface of the ear and were likely composed largely of skin tissue. All tissue was frozen and thinly cryosectioned at 5 μm and 10 μm to minimize effects from birefringence, and thaw mounted to glass microscope slides. Sections were stored at -20° C prior to analysis. Frozen sections were brought to room temperature and covered with 10 μL of phosphate buffer saline (PBS) before sealing with a coverslip to prevent sample dehydration during analysis.

2.4.2 Instrumentation

Nonlinear optical stokes ellipsometric microscopy was conducted with a custom-built microscope described previously, and shown in **Figure 2.3**.[12] For excitation, an 80 Mhz femtosecond pulsed Ti:sapphire tuneable solid state laser at 800 nm was used (MaiTai HP, SpectraPhysics). The laser passed through a beam expansion followed by an electro-optic modulator (EOM) (EOPC, Fresh Meadows, NY) operated at 8 MHz, yielding 10 unique polarization states per period of the EOM. Following the EOM, a Soleit-Babinet compensator (Thorlabs, Newton, NJ) corrected for change in polarization state from propagation through the reflective elements of the microscope. The beam then passed up a periscope to a scan-head composed of an 8.8 KHz resonant mirror coupled with a galvanometer mirror. A pair of lenses focused the scan pattern onto the back of the excitation objective while expanding the beam to fully fill the aperture (10x, 20x, and 40x, Nikon). Laser transmittance and SHG was collected via 10×, 0.3 NA OPTEM condenser, passed through a rotatable Glan-Taylor polarizer and separated with a dichroic mirror. A photomultiplier tube with a band pass filter centered at 400 nm served detected the SHG, while a photodiode detected the laser transmittance.

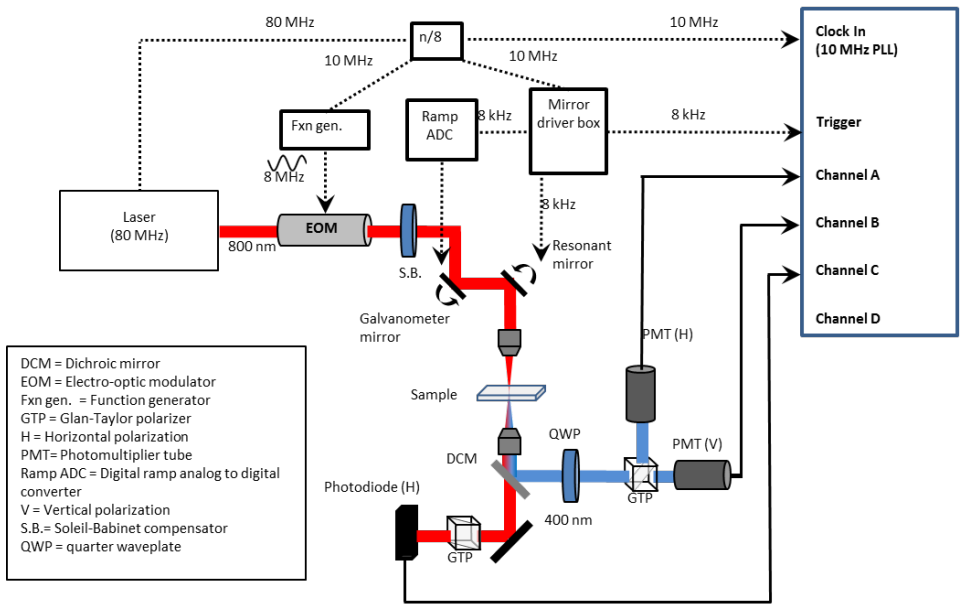

Figure 2.3 Instrument and timing schematic for NOSE instrumentation capable of rapid polarization modulation and synchronous digitization.

2.4.3 NOSE Imaging

NOSE measurements of Z-cut quartz were acquired via a linear fit to the polynomial coefficients shown above in Equation (2.3). This linear fit requires knowledge the value of Δ. During NOSE

data acquisition 30 images were gathered; 10 corresponding the to H and V components of the generated SHG, and 10 corresponding to bright-field laser transmittance images with a polarizer oriented to pass H-polarized light in front of the photodiode. Using the 10 bright field images, a pixel-by-pixel nonlinear fit to the function describing an electro-optic modulator recovered the value of Δ for each of the 10 recorded frames. Then, a linear fit to equation (2.3) on a pixel-by-pixel basis recovered the SHG polynomial coefficients in five separate images.

For tissue analysis, images were acquired with porcine skin, porcine ear, and mouse tail. Images were acquired with laser powers varying from 60-140 mW and acquisition times between 30 and 100 s and at either 40× or 10× magnification. For each image acquisition, 30 images were acquired as described above.

2.5 Results with a Model System – Z-cut Quartz

Prior to direct analysis of collagen tissue samples, theoretical validation of the NOSE measurement was conducted. Quartz cut along the Z axis is a readily available model system which exhibits a large hyperpolarizability with zero birefringence. Additionally, Z-cut quartz adopts C_3 symmetry which reduces the number of unique nonzero elements to three. Previous studies have elucidated the relative magnitude of each of these tensor elements, shown in equation (2.14) below.[12]

$$\chi_{zzz} = -\chi_{zxx} = -\chi_{xzx} \tag{2.14}$$

Combining equation (2.5) and (2.14), the laboratory frame observable polynomial coefficients giving rise to SHG intensity can be predicted. **Figure 2.4** below demonstrates the predicted polynomial coefficients overlaid with experimental measurements for Z-cut quartz in the laboratory frame. These results were generated via reference frame rotation of the Jones tensor elements followed by direct evaluation of the relations indicated in equation (2.5). Only the coefficients A, C, and E are plotted for clarity; coefficients B and D go to zero in the limit of non-resonant excitation for phase modulated excitation.

Figure 2.4 shows good agreement between the predicted polynomial coefficients and the measured values, with two notable deviations. First, the maximum amplitude observed in the C coefficient does not match the predicted intensity. While theory predicts zero-valued B and D coefficients, the measured results contain small nonzero values for these coefficients. The intensity associated with coefficients B and D accounts for this discrepancy in totality; the sum of their magnitudes averages to 0.41±0.01 over the course of all 60 degrees, and the maximum value measured for C is 3.59. Experimental error due to the high number of low signal-to-noise measurements conducted to implement this fit may explain the origin of nonzero B and D coefficients. An alternative explanation may include imperfect cuts along the z-axis of the quartz, either due to change in the structure of the NLO susceptibility tensor or due to birefringence of the scattered second harmonic. The deviation near 47-degrees is likely caused by an imperfection in the quartz crystal, dust, or a scratch; a small heterogeneity in the face of the crystal could cause a sharp change in measured coefficients due to either blocked SHG signal or additional SHG that occurs from a dust particle. The overall good agreement between predicted coefficients and those recovered via linear fitting lends credence to the use of NOSE for quantification of hyperpolarizability tensor elements.

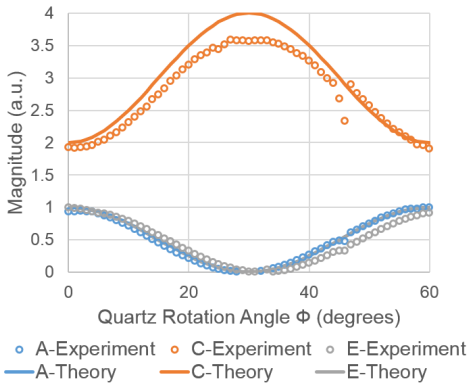

Figure 2.4 Predicted values of Polynomial coefficients of Z-cut quartz overlaid with experimentally determined values.

It is worth briefly discussing the sign ambiguity associated with fitting to the Polynomial coefficients. This is particularly relevant between coefficients A and E – the recovered A coefficient trace may swap amplitude with the E coefficient in subsequent fits to quartz at varying angles. Recall that A and E correspond directly to the co-parallel and cross-polarized linear intensity. The origin is purely due to local minima in the fit to intensity; shifting the trace of Δ by π produces the equivalent result as swapping the amplitudes of A and E. This can be artificially corrected by simply swapping the A and E coefficients when the amplitudes swap according to the trend line.

2.6 NOSE Microscopy of Collagenous Tissue

The polarization analysis pipeline used for collagenous tissue is shown in **Figure 2.5**. First, bright field laser transmittance images are treated to determine the phase of the EOM for each polarization detected; the plot of intensity versus delta is shown in **Figure 2.5b**, with fit overlaid upon intensity values from a representative single pixel. The EOM is modeled as a variable retarder oriented at 45˚ relative to the incident polarization. Intensity as a function of time is plotted for each pixel, and the detected intensity is fit to five parameters corresponding to amplitude of modulation, phase shift in the waveform, DC offset in driving voltage for the EOM, intensity scaling factor, and detector DC offset. The intensity scaling and detector DC both correspond to parameters of detection, while the remaining parameters model the induced retardance from the EOM as a sine wave in time. The corresponding values of Δ recovered from this analysis can be used to conduct single-pixel linear fits to the Fourier coefficients described in equation (2.6), shown in **2.5c**. Each coefficient can then be treated as a single channel in an RGBCM colormap, yielding **Figure 2.5d**. Note in this image that coefficient *a* is scaled by 0.5, due to its larger overall magnitude.

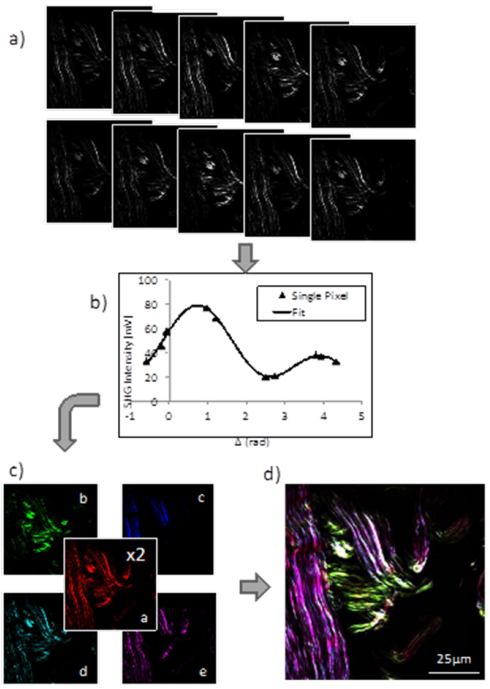

Figure 2.5 The process of linear fitting to recover Fourier coefficients for collagen fibers in a porcine ear sample. A set of 10 unique polarization-dependent images for the vertical PMT are shown in a) and a representative linear fit to recover Fourier coefficients for a single pixel is shown in b). The five Fourier coefficient images were assigned a unique color (red, green, blue, cyan and magenta) c) before being merged into a single five-color image, shown in d).

While the Fourier coefficients provide a convenient approach for visualizing differences in NLO properties, contrast is largely due to variation in collagen orientation across the field of view, as shown in **Figure 2.6**. Recovering local frame structure in the form of $\bar{\chi}_l$ can provide additional insight into structural variation in collagenous tissue. Recovery of local frame information implies

some knowledge of collagen orientation. The in-plane orientation ϕ can be recovered from the image analysis plugin OrientationJ in the ImageJ software package.[25, 26] Validation of OrientationJ for recovering azimuthal orientation on the basis of polarization analysis can be found in Chapter 4. Prior to analysis for recovery of local frame tensor information, recovered Fourier coefficient were mapped to the Polynomial coefficients by the inverse of the transform shown in equation (2.7). Two approaches to recover local-frame NLO susceptibility are reported herein.

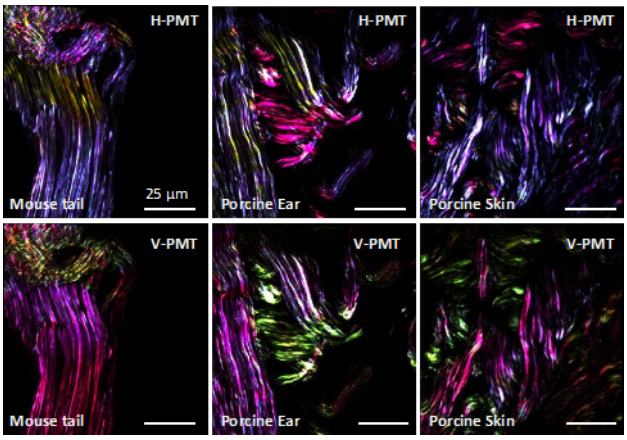

Figure 2.6 Fourier coefficient color maps for mouse tail, porcine ear and porcine skin for the horizontal and vertical detectors (H-PMT and V-PMT, respectively).

2.6.1 Pooled Analysis for Global $\chi_l^{(2)}$ Recovery

The pooled procedure was designed to identify the single most probable set of tensor elements which might give rise to all SHG activity recorded within a single field of view. This approach implies that at the macromolecular level, all collagen fibers within the field of view exhibit the same NLO susceptibility, and any variation in detected intensity arises from measurement error or variation in collagen orientation. This approach iterates between solving for orientation (in-plane azimuthal angle ϕ and the out-of-plane tilt angle θ) and local tensor elements (χ_{xxz}, χ_{zxx}, and χ_{zzz}). For the initial optimization, values for the nonzero tensor elements were assumed based on previous literature reports.[27-30] A nonlinear least-squares fit on a per-pixel basis then minimizes the difference between intensities predicted by this $\chi_l^{(2)}$ and the measured intensity by adjusting ϕ and θ, with guess values determined by OrientationJ and the

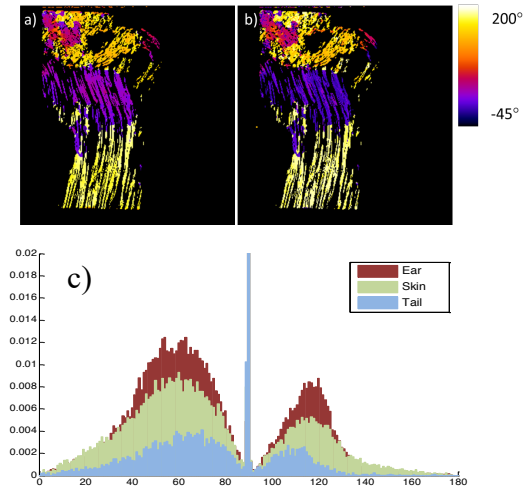

Figure 2.7 Orientation images of the azimuthal angle ϕ for a single FOV of mouse tail section a) from OrientationJ and b) from the iterative analysis are shown. The histogram of out-of-plane tilt angle θ is from iterative analysis is reported in c).

arbitrary choice of 40˚. Following the initial minimization, the recovered orientation values were fixed, and subsequent minimization of the same cost function was conducted, allowing $\chi_l^{(2)}$ to vary. This procedure was repeated twice, yielding full field of view orientation images and a single set of global tensor elements describing SHG of collagen within the field of view.

Representative orientations recovered from OrientationJ analysis are shown in **Figure 2.7a**, with ϕ from the iterative analysis shown in **Figure 2.7b**. Good agreement is observed between the two methods for all three tissue types. The histogram of θ shown in **Figure 2.7c** indicates that mouse tail tissue exhibits modal tilt angles near 90˚, with 79% of pixels containing an out-of-plane tilt angle between 85 ˚ and 95˚. In contrast, the porcine ear and skin tissues, which exhibit a larger total collagen II content than tendon-rich tissue like mouse tail, exhibit 28% amd 43% of pixels in this same range. This is likely due to the variation in tissue function – collagen found in ear and skin tissues provide structural stability to the tissue, protecting underlying cells in the animal body. In contrast, the tail tissue contains collagen-rich tendons which are instrumental to tail motion, and are organized in such a way to sustain longitudinal force across the tendon. Such a function benefits more greatly from more highly aligned collagen fibers.

The set of non-zero elements of $\chi_l^{(2)}$ recovered from the pooled analysis is shown in **Figure 2.8** with 95% confidence intervals overlaid according to variance between each field of view measured. Relative standard deviations were on the order of 17%, with recovered tensor element ratios of elements χ_{zzz}/χ_{zxx} and χ_{xxz}/χ_{zxx} for tail, ear and skin samples of (1.45, 1.04), (1.55, 1.18), and (1.65,1.24). The results of the pooled analysis displayed in **Figure 2.8a** are in good agreement previously reported values.[23, 31,32] The pooled analysis provides a robust avenue for signal averaging to improve reproducibility in the measurement, but may not be appropriate for all samples. For example, if the tissue is largely heterogeneous due to a variety of collagenous structures within the field of view, either endogenously occurring or present due to pathogenesis, then differing subpopulations of collagen

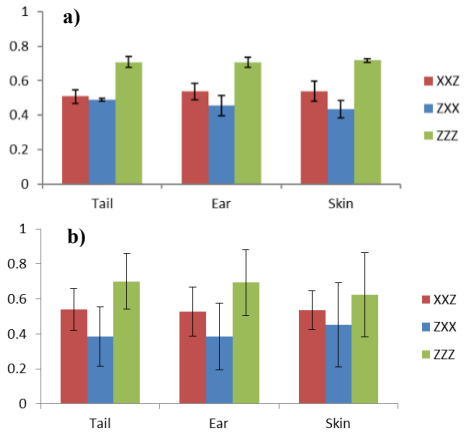

Figure 2.8 Normalized local- frame tensor elements for the three tissue types for a) pooled analysis and b) pixel-by-pixel analysis. Error bars indicate 95% CI within each sample set.

structure will alter the recovered tensor values. In such cases, it is more appropriate to consider analysis of single-pixel results, so that variation in structure across the field of view can be characterized. **Figure 2.8b** illustrates recovered tensor element values for the single-pixel approach described in section 2.6.2.

2.6.2 Single Pixel Analysis of $\chi_l^{(2)}$ for Heterogeneous Samples

To evaluate intra-sample variation in collagen structure, a noniterative approach differing from the pooled analysis was conducted. In this method, values for ϕ and θ from the pooled analysis were utilized and a nonlinear optimization to $\chi_l^{(2)}$ was conducted at each pixel based on the minimization of the difference between predicted and measured intensity. The tensor elements χ_{xxz}, χ_{zxx},and χ_{zzz} were retrieved for each pixel in the image. Measured relative standard deviations were on the order of 60% for the single pixel analysis (error propagation from uncertainty in orientation is reflected in this uncertainty), likely attributed to the lower degree of signal averaging present in the approach. Typical data acquisition times were on the order of 1.5 μs per pixel, corresponding to a maximum acquisition time of 150 ns for a single polarization at video-rate. Synchronous digitization, i.e., digitization of a single voltage value at the maximum of the photodiode/photomultiplier tube voltage transient, significantly reduces 1/f noise, enabling sufficient signal-to-noise ratios for single pixel analysis.[33]

Performance of the single pixel analysis can be contrasted with the pooled approach in **Figure 2.7.** Aside from differences in uncertainty, the major deviation between the two approaches is the relative amplitude of the χ_{xxz} and χ_{zxx} elements, yielding χ_{xxz}/χ_{zxx} ratios of 1.19, 1.40, and 1.37 on average for the tail, ear, and skin samples – a slight increase from the values of 1.04, 1.18, and 1.24 observed in the pooled analysis. Retrieved values for the ratio χ_{zzz}/χ_{zxx} were 1.38, 1.82, and 1.80, also slightly larger than the values recovered in the pooled analysis. This is possibly an artifact of the higher uncertainty for recovered tensor elements in the single pixel analysis - the distribution of both tensor elements in the ratio is a normally distributed random variable, however the ratio of those random variables does not follow a Gaussian distribution. The values reported above correspond to the ratio of the average tensor elements, rather than the average of the ratio

of per-pixel tensor elements. Ultimately, both approaches yield good agreement with previously reported tensor ratios.[34]

Figure 2.9 shows RGB color maps for the χ_{xxz}, χ_{zxx}, and χ_{zzz} tensor elements, where each color channel represents a single tensor element. Brightness is scaled by the raw detected SHG intensity while hue maps relative tensor element amplitudes. The maps of NLO susceptibility in **Figure 2.9** provide evidence of structural variation in collagen across each field of view. This heterogeneity raises the question of origin – how does the assembly of tropocollagen or collagen fibrils vary to produce the resulting distribution of susceptibilities? Furthermore, how does the modeling described in section 2.3 inform upon the structure of collagen observed via NOSE imaging?

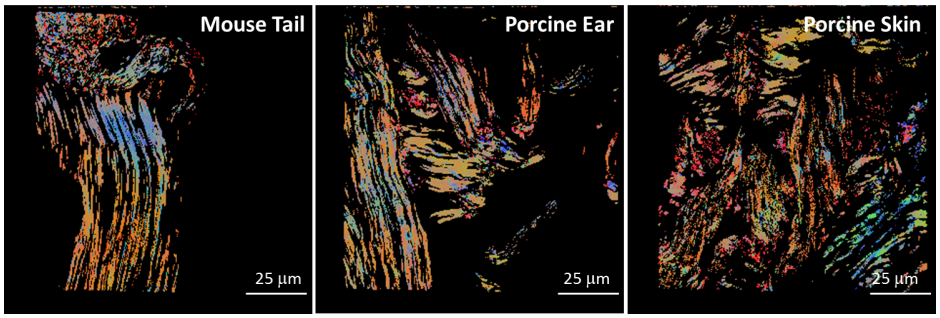

Figure 2.9 Images representing the relationships between the three unique local frame tensor elements, $\chi^{(2)}_{xxz}$, $\chi^{(2)}_{zxx}$ and $\chi^{(2)}_{zzz}$ for the three tissue types. Images were created by assigning each tensor image acquired from the pixel-by-pixel analysis a unique color (green, blue and red for $\chi^{(2)}_{xxz}$, $\chi^{(2)}_{zxx}$ and $\chi^{(2)}_{zzz}$ respectively) and overlaying them on the same intensity scale. Image brightness represents overall SHG intensity and the hue of the image represents the relative magnitudes of $\chi^{(2)}_{xxz}$, $\chi^{(2)}_{zxx}$ and $\chi^{(2)}_{zzz}$.

2.6.3 Ab initio predictions of tropocollagen hyperpolarizability

Table 2.1 relates several modeled ratios β_{zzz}/β_{zxx} obtained from the symmetry additive approach. The results reported here are in qualitative agreement with previously reported calculations for collagen fibers.[21,23] The hybrid method B3LYP TD-DFT performs most closely to previously reported methods. It was anticipated that the small degree of exchange computed from the local density approximation may introduce some error in computation of molecular hyperpolarizability which involves significant electron delocalization about the molecule. Long-range corrected functionals were tested to see if this was true, however reported values from the LC-BLYP and

Table 2.1 The ratios of molecular tensors recovered from *ab initio* calculation. ONIOM results adapted from de Wergifosse et al.

	$\beta^{(2)}_{zzz}/\beta^{(2)}_{zxx}$
TDDFT-B3LYP	4.5
TDHF	-25
LC-BLYP	-14
LC-BOP	-13
ONIOM*	2.97

LC-BOP methods were more similar to TD-HF results which neglect correlation entirely. Regardless of difference in magnitude, β_{zzz} is shown universally to be the dominant contributor to the nonlinear optical response of tropocollagen, while β_{zxx} and β_{xxz} contribute significantly less.

It is worth briefly discussing the significance of dominant β_{zzz} character, as this will have relevance in later chapters. β_{zzz} dominance has direct implications on the macromolecular NLO susceptibility in the laboratory frame. All nonzero tensor elements in the macromolecular frame are the result of a projection of β_{zzz}. Correspondingly, this indicates an interchangeability in indices at the ensemble level; the projections of β_{zzz} onto χ_{zxx} and χ_{xxz} are identical. This model holds experimentally for type I collagen samples, but varying values of χ_{zxx} and χ_{zxx} have been reported for type II collagen, which is more abundant in cartilage and within the vitreous humor of the eye.[34] The general trend of $\chi_{zxx} = \chi_{zxx}$ provides a convenient method for reducing the number of unknown parameters when fitting to the tensor elements of collagen, and will be utilized in subsequent chapters to reduce uncertainty in fits to recover $\chi_l^{(2)}$.

The overall dominant character of β_{zzz} at the tropocollagen level provides context with which to interpret the tensor ratios reported in sections 2.6.1 and 2.6.2. By modeling the tropocollagen subunit as a β_{zzz} dominant structure, varying orientation distributions can be considered to evaluate the most probable macromolecular assembly which gives rise to the observable signal.

2.6.4 Interpreting χ_{zzz}/χ_{zxx} in the Context of Fibrillar Orientation

Interpreting measured SHG intensities and tensor element ratios in the context of macromolecular collagen assembly provides some insight on sub-micron structure within collagenous tissue. The most straightforward possible orientation distribution function describing tropocollagen alignment within a collagen fibril and subsequent fibrillary alignment is a delta function distribution. In the case of perfect alignment, i.e., all tropocollagen molecules are oriented parallel to the primary fiber

axis, the tensor element ratios at the molecular frame and macromolecular frame are anticipated to be proportional. Equivalency of the β_{zzz}/β_{zxx} and χ_{zzz}/χ_{zxx} ratios is not observed, however, with ONIOM modeling predicting a β_{zzz}/β_{zxx} and TD-DFT/B3LYP yielding a ratio of 4.5, in contrast with the observed χ_{zzz}/χ_{zxx} of 1.4-1.8.[21] Allowing the mean of the orientation distribution to rotate off-axis yields varying ratios as a function of tilt angle shown in **Figure 2.10**. In order to achieve a ratio on the order of 1.5, fibrillary tilt angle distributions would exceed an angle of 50 degrees. Previous experimental probes of collagen fibril structure indicate this angle is unlikely. Electron tomography of corneal collagen showed tilt angles on the order of 15˚, while NMR of sheep tendon yielded tilt angle distributions near 19˚.[35, 36] Scanning electron microscopy probes of rat tail tendon showed heterogeneous distributions of collagen fibril orientation, including both interweaved and random alignment in addition to the modal observation of highly aligned fibrils.[37,38] Note, however, that these probes do not have the sufficient resolution to assess tropocollagen distribution within individual fibrils. Regardless, it is clear based on the body of the literature that a delta

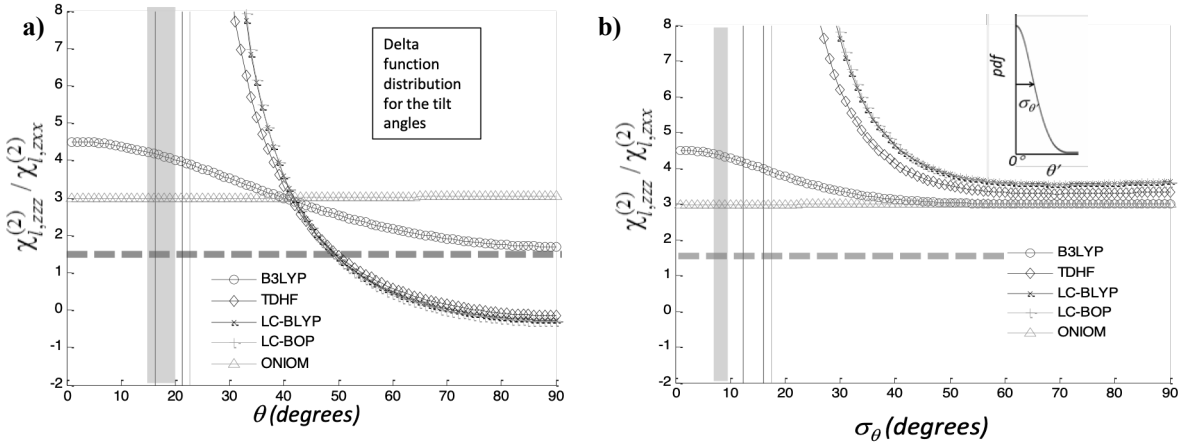

Figure 2.10 a) The ratio of χ_{zzz}/χ_{zxx} as a function of tilt angle of triple helices given different input values of β_{zzz}/β_{zxx} b) The ratio of χ_{zzz}/χ_{zxx} as a function of the spread of the tilt angle distribution of triple helices given different input values of β_{zzz}/β_{zxx}. Note: χ_{zzz}/χ_{zxx} is equivalent to $\chi^{(2)}_{l,zzz}/\chi^{(2)}_{l,zxx}$; notation variance is due to the reproduction of this figure from reference 1.

function distribution is insufficient to describe the measured polarization dependence.

Modeling the predicted tensor ratio χ_{zzz}/χ_{zxx} as a function of a Gaussian distribution of fibrillary tilt angles yields the set of traces in **Figure 2.10b**. Here, the spread of the distribution $\sigma_{\theta,}$ is plotted versus the tensor ratio; the vertical bar between 5-8˚ delineates $\sigma_{\theta,}$ angles of high probability for the tilt angle of 15-20˚ indicated by prior experiment. The asymptotic behavior of the Gaussian

predi cctions contrasts with predicted ratios by the delta function distribution. In the broadly disordered limit this model predicts a fixed ratio $\chi_{zzz}/\chi_{zxx} = 3$, which can be rationalized in the weak order limit where $\chi_{zzz} \cong \chi_{zxx} + \chi_{xzx} + \chi_{xxz}$.[39] Since the ONIOM model yields the weak-order result for a delta-function distribution, it is unsurprising that the predicted ratio is insensitive to broadness of the Gaussian distribution. However, there is at present no feasible explanation for the experimentally measured ratio on the order of 1.4-1.8 for a monotonic distribution of tilt angles.

Previous reports have indicated that fibrous collagen domains may orient in an alternating fashion across the tissue. Local order may be preserved, enabling the measurement of SHG, but over longer periods the fiber orientation may flip 180˚, resulting in domains of varying orientation. [40] SEM measurements have also observed collagen fibrils twisting at the fibrillary crimp on the order of 180˚.[41] These studies indicate modeling the orientation distribution with a bimodal distribution may be appropriate, and that experimental measurements provide some evidence for subpopulations of higher and lower relative order. Within this regime, if it is assumed the less-ordered component adheres to the weak-order limit ($\chi_{zzz}/\chi_{zxx} = 3$), then the net distribution can be represented as a linear combination of a narrow distribution and a broad antiparallel distribution. Using the experimentally determined tilt angle of ~17˚ as the anticipated modal outcome, the unknown parameters of the resulting distribution correspond only to the relative volume fraction within each subpopulation by utilizing the coparallel χ_{zzz}/χ_{zxx} recovered from NOSE microscopy. The resulting analysis indicates volume fractions of 0.43, 0.43, and 0.42 coparallel collagen fibrils for the tail, ear, and skin samples, yielding on average 57% of fibrils adopting antiparallel orientations. Note that this analysis was unable to recover experimentally observed tensor element ratios using the literature reported value $\beta_{zzz}/\beta_{zxx} = 2.97$ from ONIOM.[21] A visual representation of the net orientation distribution can be found in **Figure 2.11**.

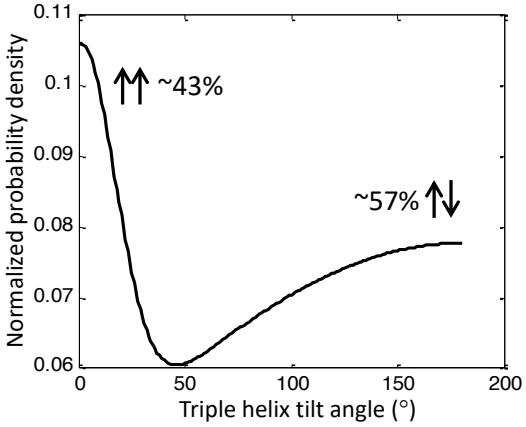

Figure 2.11 Bimodal distribution of collagen triple helix tilt angles with respect to the fiber axis.

2.7 Conclusions

This chapter discussed the polarization-resolved measurement of nonlinear optical susceptibility spanning study from theoretical modeling at the molecular level up to ensemble-level measurements, relating the laboratory frame observables back to local structure in the sample. This architecture was applied to both thin non-birefringent Z-cut quartz samples as well as collagenous tissues. Theoretical methods for modeling polarization transfer in linear and nonlinear optics using the Jones framework were summarized; key to this discussion was the lack of depolarization induced by the sample. The framework maps polarization transfer beginning at the local susceptibility which can be reduced in complexity by symmetry and in turn mapped to a laboratory-frame response through proper use of Euler rotation matrices.

An instrument for NOSE microscopy was described and applied to measure the polarization dependent SHG from Z-cut quartz and to image collagen-rich thin tissue sections. Multiple incident polarization states as well as polarization-resolved detection facilitated measurement of the local frame susceptibility $\chi_l^{(2)}$. The approach described in this chapter leveraged rapid polarization modulation enabled by an electro-optic modulator to suppress 1/f noise commonly associated with rotating fixed optic modulation approaches. This method enabled single-pixel recovery of azimuthal and tilt angles, as well as NLO susceptibility tensors for each pixel in the field of view. Measured tensor ratios χ_{zzz}/χ_{zxx} on the order of 1.4-1.8 and χ_{zxx}/χ_{xxz} of 1.0-1.4 agree in large part with previous reports.

To generate a model of the structure of collagen, the molecular hyperpolarizability $\beta^{(2)}$ of tropocollagen was modeled using *ab initio* methods. The model amino acid NMA was utilized as a stand-in for native amino acids in the tropocollagen molecule, due to the dominant character of the amide bond in generating the overall hyperpolarizability. The symmetry additive model then provided a mechanism by which the coherent summation of individual amino acid residues could form the tropocollagen nonlinear optical response. Using this approach, β_{zzz} was found to be the dominant contributor to tropocollagen hyperpolarizability and this observation was used as a basis for building a model of orientation distributions for collagen fibrils about the collagen fiber axis.

Both the *ab initio* predictions of molecular hyperpolarizability and measured macromolecular susceptibility $\chi_l^{(2)}$ served as the basis for building a model of collagen fibril orientation. Previous experimental efforts utilizing SEM, NMR, and electron tomography found collagen fibril tilt angles on the order of 14-18˚. However, models based on monotonic distributions were unable to reproduce the macromolecular observed χ_{zzz}/χ_{zxx} on the order of 1.4-18 under such constraints. Evidence for multidomain collagenous structures incorporating regions of higher and lower order has been reported from X-ray diffraction of collagen fibers, while polarization-resolved SFG has indicated presence of antiparallel collagen fibrils contributing to the overall collagen structure.[42] Cumulatively these two observations served as a basis for modeling the macromolecular response as a net effect from a bimodal distribution of fibril tilt angles. The global orientation distribution was modeled as a sum of a narrow Gaussian distribution, predicting co-parallel oriented fibrils and a broad Gaussian consisting of largely antiparallel oriented fibers. Within the scope of this analysis the measured ratio χ_{zzz}/χ_{zxx} was found to coincide with a predicted volume fraction of 43% of collagen fibrils orienting narrowly about the fiber axis, with a much larger portion of fibrils orienting broadly antiparallel (57%).

This chapter lays the foundation for chapters 3-5, where additional efforts in polarization dependent NLO microscopy will be explored. Furthermore, the detailed analysis of collagen structure and orientation will serve as critical background for future discussions, such as in chapter 5 where collagen orientation will interplay with polarization and contributions to SHG from depolarized light in thick, turbid tissues. In the subsequent chapter, alternative methods of polarization modulation are explored utilizing a patterned microretarding array to spatially modulate polarization across the field of view of an NLO microscope.

2.8 References

1. Dow, Ximeng Y.; DeWalt, Emma L.; Sullivan, Shane Z.; Schmitt, Paul D.; Ulcickas, James R. W.; Simpson, Garth J., Imaging the Nonlinear Susceptibility Tensor of Collagen by Nonlinear Optical Stokes Ellipsometry. *Biophysical Journal* **2016,** *111* (7), 1361-1374.

2. Campagnola, P. J.; Loew, L. M., Second-harmonic imaging microscopy for visualizing biomolecular arrays in cells, tissues and organisms. *Nature Biotechnology* **2003,** *21* (11), 1356-1360.

3. Newman, J. A.; Scarborough, N. M., Intercalating dyes for enhanced contrast in second-harmonic generation imaging of protein crystals. *... Section D: Biological ...* **2015**.

4. Kolacna, L.; Bakesova, J.; Varga, F., Biochemical and biophysical aspects of collagen nanostructure in the extracellular matrix. *Physiological ...* **2007**.

5. Nadiarnykh, O.; Plotnikov, S.; Mohler, W. A., Second harmonic generation imaging microscopy studies of osteogenesis imperfecta. *... of biomedical optics* **2007**.

6. Plotnikov, S. V.; Kenny, A. M., Measurement of muscle disease by quantitative second-harmonic generation imaging. *Journal of ...* **2008**.

7. Golaraei, A.; Cisek, R.; Krouglov, S.; Navab, R.; Niu, C.; Sakashita, S.; Yasufuku, K.; Tsao, M.-S.; Wilson, B. C.; Barzda, V., Characterization of collagen in non-small cell lung carcinoma with second harmonic polarization microscopy. *Biomedical Optics Express* **2014,** *5* (10), 3562.

8. Levental, K. R.; Yu, H.; Kass, L.; Lakins, J. N.; Egeblad, M., Matrix crosslinking forces tumor progression by enhancing integrin signaling. *Cell* **2009**.

9. Petralli-Mallow, T.; Wong, T. M.; Byers, J. D.; Yee, H. I., Circular dichroism spectroscopy at interfaces: a surface second harmonic generation study. *Journal of physical ...* **1993**.

10. Tiaho, F.; Recher, G.; Rouede, D., Estimation of helical angles of myosin and collagen by second harmonic generation imaging microscopy. *Optics express* **2007**.

11. Amat-Roldan, I.; Psilodimitrakopoulos, S., Fast image analysis in polarization SHG microscopy. *Optics ...* **2010**.

12. DeWalt, E. L.; Sullivan, S. Z.; Schmitt, P. D.; Muir, R. D.; Simpson, G. J., Polarization-Modulated Second Harmonic Generation Ellipsometric Microscopy at Video Rate. *Analytical Chemistry* **2014,** *86* (16), 8448-8456.

13. Simpson, G. J., *Nonlinear Optical Polarization Analysis in Chemistry and Biology*. Cambridge University Press: Cambridge, 2017.

14. Moad, A. J.; Moad, C. W.; Perry, J. M.; Wampler, R. D.; Begue, N. J.; Shen, T.; Goeken, G. S.; Heiland, R.; Simpson, G., J., NLOPredict: Visualization and data analysis software for nonlinear optics. *J. Comput. Chem.* **2007,** *28*, 1996-2002.

15. Perry, J. M.; Moad, A. J.; Begue, N. J.; Wampler, R. D.; Simpson, G. J., Electronic and Vibrational Second-Order Nonlinear Optical Properties of Protein Secondary Structural Motifs. *The Journal of Physical Chemistry B* **2005,** *109* (42), 20009-20026.

16. Wampler, R. D.; Moad, A. J.; Moad, C. W.; Heiland, R.; Simpson, G. J., Visual Methods for Interpreting Optical Nonlinearity at the Molecular Level. *Accounts of Chemical Research* **2007,** *40* (10), 953-960.

17. Gordon, M. S.; Schmidt, M. W., Advances in electronic structure theory: GAMESS a decade later. In *Theory and applications of computational chemistry*, Elsevier: 2005; pp 1167-1189.
18. Becke, A. D., A new mixing of Hartree-Fock and local-density-functional theories. *J. Chem. Phys.* **1993,** *98* (2), 1372-7.

19. Karna, S. P.; Dupuis, M., Frequency dependent nonlinear optical properties of molecules: formulation and implementation in the HONDO program. *J. Comput. Chem.* **1991,** *12* (4), 487-504.

20. Kamiya, M.; Sekino, H.; Tsuneda, T.; Hirao, K., Nonlinear optical property calculations by the long-range-corrected coupled-perturbed Kohn–Sham method. *The Journal of chemical physics* **2005,** *122* (23), 234111.

21. de Wergifosse, M.; de Ruyck, J.; Champagne, B., How the Second-Order Nonlinear Optical Response of the Collagen Triple Helix Appears: A Theoretical Investigation. *The Journal of Physical Chemistry C* **2014,** *118* (16), 8595-8602.

22. Loison, C.; Simon, D., Additive Model for the Second Harmonic Generation Hyperpolarizability Applied to a Collagen-Mimicking Peptide (Pro-Pro-Gly)(10). *Journal of Physical Chemistry A* **2010,** *114* (29), 7769-7779.

23. Tuer, A. E.; Krouglov, S.; Prent, N.; Cisek, R.; Sandkuijl, D.; Yasufuku, K.; Wilson, B. C.; Barzda, V., Nonlinear Optical Properties of Type I Collagen Fibers Studied by Polarization Dependent Second Harmonic Generation Microscopy. *The Journal of Physical Chemistry B* **2011,** *115* (44), 12759-12769.

24. Haupert, L. M.; DeWalt, E. L.; Simpson, G. J., Modeling the SHG activities of diverse protein crystals. *Acta Crystallogr., Sect. D: Biol. Crystallogr.* **2012,** *68* (11), 1513-1521.

25. Püspöki, Z.; Storath, M.; Sage, D.; Unser, M., Transforms and Operators for Directional Bioimage Analysis: A Survey. In *Focus on Bio-Image Informatics*, De Vos, W. H.; Munck, S.; Timmermans, J.-P., Eds. Springer International Publishing: Cham, 2016; pp 69-93.

26. Schneider, C. A.; Rasband, W. S.; Eliceiri, K. W., NIH Image to ImageJ: 25 years of image analysis. *Nature Methods* **2012,** *9* (7), 671-675.

27. Yew, E. Y. S.; Sheppard, C. J. R., Second harmonic generation polarization microscopy with tightly focused linearly and radially polarized beams. *Opt. Commun.* **2007,** *275* (2), 453-457.

28. Tuer, A. E.; Krouglov, S.; Prent, N.; Cisek, R.; Sandkuijl, D.; Yasufuku, K.; Wilson, B. C.; Barzda, V., Nonlinear Optical Properties of Type I Collagen Fibers Studied by

Polarization Dependent Second Harmonic Generation Microscopy. *Journal of Physical Chemistry B* **2011,** *115* (44), 12759-12769.

29. Su, P.-J.; Chen, W.-L.; Chen, Y.-F.; Dong, C.-Y., Determination of collagen nanostructure from second-order susceptibility tensor analysis. *Biophysical journal* **2011,** *100* (8), 2053-2062.

30. Tuer, Adam E.; Akens, Margarete K.; Krouglov, S.; Sandkuijl, D.; Wilson, Brian C.; Whyne, Cari M.; Barzda, V., Hierarchical Model of Fibrillar Collagen Organization for Interpreting the Second-Order Susceptibility Tensors in Biological Tissue. *Biophysical Journal* **2012,** *103* (10), 2093-2105.

31. Hovhannisyan, V. A.; Su, P.-J.; Lin, S.-J.; Dong, C.-Y., Quantifying thermodynamics of collagen thermal denaturation by second harmonic generation imaging. *Applied Physics Letters* **2009,** *94* (23), 233902.

32. Tiaho, F.; Recher, G.; Rouede, D., Estimation of helical angles of myosin and collagen by second harmonic generation imaging microscopy. *Optics express* **2007,** *15* (19), 12286-12295.

33. Muir, R. D.; Sullivan, S. Z.; Oglesbee, R. A.; Simpson, G. J., Synchronous digitization for high dynamic range lock-in amplification in beam-scanning microscopy. *Review of Scientific Instruments* **2014,** *85* (3), 033703.

34. Romijn, E. I.; Finnøy, A.; Lilledahl, M. B., Analyzing the feasibility of discriminating between collagen types I and II using polarization-resolved second harmonic generation. *Journal of Biophotonics* **2019,** *12* (1), e201800090.

35. Fechete, R.; Demco, D. E.; Blumich, B.; Eliav, U.; Navon, G., Anisotropy of collagen fiber orientation in sheep tendon by 1H double-quantum-filtered NMR signals. *Journal of magnetic resonance (San Diego, Calif. : 1997)* **2003,** *162* (1), 166-75.

36. Holmes, D. F.; Gilpin, C. J.; Baldock, C.; Ziese, U.; Koster, A. J.; Kadler, K. E., Corneal collagen fibril structure in three dimensions: Structural insights into fibril assembly, mechanical properties, and tissue organization. *Proc Natl Acad Sci* **2001,** *98* (13), 7307-7312.

37. Provenzano, P. P.; Vanderby, R., Collagen fibril morphology and organization: implications for force transmission in ligament and tendon. *Matrix Biology* **2006,** *25* (2), 71-84.

38. Kannus, P., Structure of the tendon connective tissue. *Scandinavian journal of medicine & science in sports* **2000,** *10* (6), 312-20.

39. Simpson, G. J.; Rowlen, K. L., An SHG magic angle: dependence of second harmonic generation orientation measurements on the width of the orientation distribution. *Journal of the American Chemical Society* **1999,** *121* (11), 2635-2636.

40. Han, Y.; Raghunathan, V.; Feng, R.-r.; Maekawa, H.; Chung, C.-Y.; Feng, Y.; Potma, E. O.; Ge, N.-H., Mapping molecular orientation with phase sensitive vibrationally resonant sum-frequency generation microscopy. *The Journal of Physical Chemistry B* **2013,** *117* (20), 6149-6156.

41. Franchi, M.; Ottani, V.; Stagni, R.; Ruggeri, A., Tendon and ligament fibrillar crimps give rise to left-handed helices of collagen fibrils in both planar and helical crimps. *Journal of anatomy* **2010,** *216* (3), 301-309.

42. Hulmes, D.; Wess, T. J.; Prockop, D. J.; Fratzl, P., Radial packing, order, and disorder in collagen fibrils. *Biophysical Journal* **1995,** *68* (5), 1661.

CHAPTER 3. SPATIALLY ENCODED POLARIZATION DEPENDENT NONLINEAR OPTICS

The contents of this chapter are adapted from the paper Spatially encoded polarization-dependent nonlinear optics, originally published in *Optics Letters* in 2018.[1]

3.1 Introduction

Polarization-dependent nonlinear optical processes, including second harmonic generation (SHG) and two-photon excited fluorescence (TPEF), provide unique mechanisms of contrast for biological and pharmaceutical imaging. Polarization analysis provides information on scales of molecular dimension, complementing the micron-scale information accessible by microscopy. SHG provides a highly specific imaging modality with excellent signal to noise to investigate these systems by virtue of the noncentrosymmetric symmetry requirement, power scaling of the square of incident light reducing out of plane signal contribution, and compatibility with near-IR excitation, which has long penetration depth in biological tissue. These properties in general have led to utilization of SHG microscopy for imaging biological structures such as collagen and myosin, with specific application in quantifying renal fibrosis as well as burn tissue recovery.[1–4]

Of particular note is the application of polarization dependent SHG for analysis of collagen structure in tissue diagnostics. Collagen organization is a commonly cited biomarker for cancers such as non-small cell lung carcinoma, and ovarian and breast cancers due to associated extracellular fibrosis and reduced metabolism of collagen.[5–7] While the majority of pathology diagnostics have centered on the microscopic collagen arrangement as determined from image analysis, polarization-dependent SHG measurements provide complementary information on length scales smaller than the wavelength of light. To demonstrate polarization-dependent SHG microscopy, the simplest approach to modulate polarization is with fixed optics such as quarter and half waveplates, rotated between each image acquired to generate a polarization-dependent image stack.[8–10]

In this work, a 25.4 mm diameter microretarder array (μRA) compatible for retrofitting into both beam-scanning and wide-field illumination microscopes was placed in the rear-conjugate plane of a microscope to rapidly and passively modulate the polarization state of light during beam-scanning imaging. The optic

consisted of an array of a liquid crystal designed for ½ wave retardance with a 2° increase in the angle of the fast axis across every 25 µm strips along diameter of the array. When placed in the rear-conjugate plane, the polarization rotation introduced by the µRA was mapped one-to-one to the corresponding pixel in the field of view (FoV). The resulting image contains "stripes" of varying polarization co-parallel with the modulation axis of the µRA. Translation of the sample through one period of this polarization-dependent pattern allows access of each sample position to each polarization state. Subsequent digital image registration is conducted via cross-correlation, such that each pixel in the resulting image stack contains a vector of different incident polarizations onto the sample. Retrieval of tensor elements on a per-pixel basis was performed by fitting to this image stack.

3.2 Experimental Methods

The experiment instrument is illustrated in **Figure 3.1**. The laser source was a Spectra-Physics MaiTai HP operating at 800 nm, with the µRA (DPP-25, Thorlabs) placed in the rear conjugate plane of the beam scanning microscope with horizontally polarized incident light. The µRA was used to spatially encode the polarization as a function of position with an embedded thin layer of liquid crystal with a retardance set at half wave for 800 nm light. Along the vertical axis of the optic, the fast axis of retardance was rotated linearly. During beam-scanning imaging, a smoothly modulated polarization with a period of approximately 60 pixels (~105 µm with 10x objective) was encoded parallel to the vertical (V) axis of the image plane (**Figure 3.1** inset), with the constant polarization along the horizontal (H) axis. The H and V polarized SHG responses were acquired sequentially by rotation of a polarizer prior to the detector. Although sample translation versus polarization rotation is comparable in speed, translation leverages the existing components for sample positioning inherent to virtually all microscope stages.

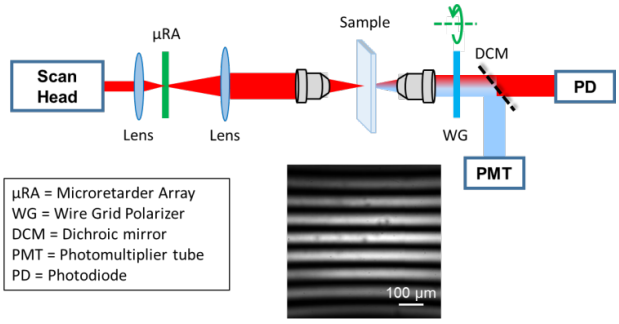

Figure 3.1 Instrument schematic. Placement of the µRA in the rear-conjugate plane enables polarization encoding across the FoV. Insert image: laser transmittance with no sample and the analyzer passing horizontally polarized light.

The polarization modulation along the FoV was determined by a single transmittance image detected at H-polarization with no sample. The polarization rotation angle γ at each position within the FoV was

determined from nonlinear fit. To achieve polarization dependent measurement for each pixel, the sample was translated 18 times along V direction with a step size of 5 μm, giving a total translation of 90 μm, about 1 full period of the modulated polarization. Pixel-to-pixel registry between the images in the stack was determined by cross-correlation after removing background pixels. The translation increment was determined as about 2 pixels per frame with cross-correlation for the total 19 frames, yielding a final 512×476×19 data cube. It should be noted that translation increments were not identical from frame to frame but were measured via cross-correlation. The laboratory nonlinear optical (NLO) tensor elements at each pixel were then recovered by fitting the 19 element vector as a function of γ. Independently determining the azimuthal angle using *OrientationJ* enabled the coordinate transformation from laboratory to local frame responses on a per pixel basis using methods identical to previous reports.[11,12]

3.3 Theoretical Foundation

This approach for polarization modulated SHG analysis was first performed using z-cut quartz, which has well-established nonlinear optical properties consistent with 3-fold rotational symmetry and no linear birefringence for light propagating coparallel with the z-axis. The uniform structure of z-cut quartz simplified the translation measurement. The quartz was inserted in an automated rotation stage to adjust the orientation between the local-frame and the laboratory frame. SHG images were taken for twenty unique rotation angles of quartz with 3-degree increments (**Figure 3.2**). The images were averaging along the horizontal axis due to a theoretically uniform response for SHG from quartz. The resulting set of vectors was then reshaped as a pseudo-image with axes corresponding to spatially varying polarization (γ) and z-cut quartz rotation angle (α). This procedure was performed on both the bright field (BF) and the SHG intensity images. The resulting pseudo-image showed no variation in BF intensity as a function of quartz rotation angle. In contrast, the polarized SHG intensity exhibited modulation with a period of 60 degrees, as predicted by the 3-fold symmetry of the quartz crystal. The position of the polarization rotation angle γ was determined from a global fit of the bright field images to the equation $I(\gamma) \propto \cos(\gamma + \delta) + DC$, in which δ is the phase offset and γ is the polarization rotation angle. Because the μRA will not generally be perfectly aligned along either the horizontal or vertical axes, the position-dependent polarization is given by $\gamma(x, y) = ax + by$, in which the peak-to-peak period of modulation c is given by $c = \sqrt{a^2 + b^2}$. Should the unique axis of the μRA happen to be placed exactly coparallel with the vertical axis, a would equal zero and the modulation would be entirely along the y-coordinate. The laboratory-frame nonlinear optical

properties of the sample can be expressed through five polynomial coefficients given in Eq. (3.1), which in turn are analytically connected to the sample orientation and intrinsic nonlinear optical response, as detailed in our former work.[13] The five polynomial coefficients for *n*-polarized SHG are related to the laboratory NLO tensor elements as $A = \left|\chi_{nHH}^{(2)}\right|^2$, $B = 4 \cdot \mathrm{Re}\left(\chi_{nHH}^{(2)*} \cdot \chi_{nHV}^{(2)}\right)$, $C = 4 \cdot \left|\chi_{nHV}^{(2)}\right|^2 + 2 \cdot \mathrm{Re}\left(\chi_{nHH}^{(2)*} \cdot \chi_{nVV}^{(2)}\right)$, $D = 4 \cdot \mathrm{Re}\left(\chi_{nVV}^{(2)*} \cdot \chi_{nHV}^{(2)}\right)$, and $E = \left|\chi_{nVV}^{(2)}\right|^2$.

$$I_n = A\cos^4\gamma + B\cos^3\gamma\sin\gamma + C\cos^2\gamma\sin^2\gamma + D\cos\gamma\sin^3\gamma + E\sin^4\gamma \tag{3.1}$$

3.4 Measuring the NLO Susceptibility of Z-cut Quartz

As a model system, Z-cut quartz provides two distinct advantages for evaluating the technique. First, as a single crystal sample orientation effects on SHG intensity can easily be evaluated by rotating the quartz mechanically. Second, the homogeneous nature of the crystal enables averaging across the unmodulated axis of the image, as shown in **Figure 3.2**. For the bright field image, no modulation in signal intensity was observed as a function of quartz rotation angle. The same process was performed for SHG (bottom), in which modulation of the SHG intensity was observed as a function of quartz orientation.

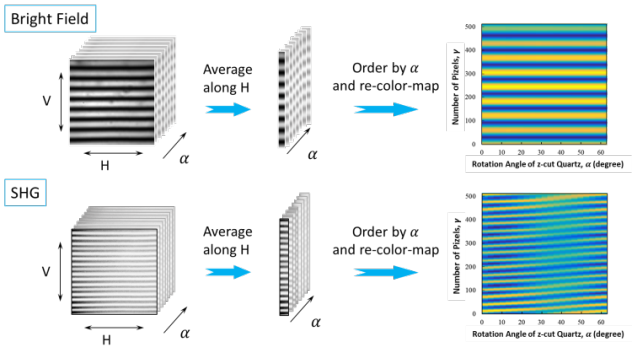

Figure 3.2 Illustration of data treatment for Z-cut quartz. Bright field images (top) are organized by rotation angle of the quartz, α. Images are averaged along the fast axis (H), forming a set of vectors which were reordered into a pseudo-image with one spatial dimension (V) and the angle of quartz as the second dimension.

The local-frame symmetry-allowed tensor elements for quartz accessible in this configuration correspond to $\chi_{yyy} = -\chi_{yxx} = -\chi_{xyx} = -\chi_{xxy}$, in the local frame with the quartz *z*-axis oriented coparallel with the optical axis. The corresponding set of polynomial coefficients expected in the laboratory

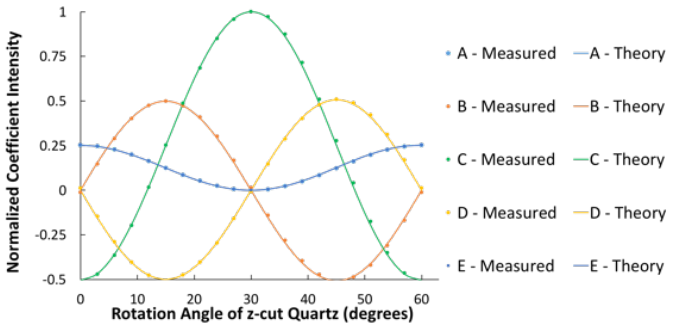

Figure 3.3 Overlay of measured polynomial coefficients (dots) with predicted coefficients (solid lines) calculated with no adjustable parameters from the known symmetry and tensor elements of z-cut quartz.

frame can be predicted for a known azimuthal orientation with no adjustable parameters and compared with the experimentally observed set of coefficients, shown in Figure 3.[13] It is worth emphasizing that the solid traces in **Figure 3.3** are *NOT* fits to the data (dots), but the independent prediction of the anticipated results with no adjustable parameters. The agreement between the measured and prediction is excellent. This analysis recovered the tensor ratio $\chi_{zzz}/\chi_{zxx} = -1.0 \pm 0.1$, in excellent agreement with the theoretical ratio $\chi_{zzz}/\chi_{zxx} = -1$ demanded by the 3-fold symmetry of z-cut quartz. This agreement supports the validity of the mathematical framework for polarization analysis and the accuracy of the presumed polarization state delivered to the sample as a function of position.

3.5 Imaging the NLO Susceptibility of Collagen

Measurements of heterogeneous collagenous samples were made by translation of the sample across the polarization modulation (**Figure 3.4**). The position of the μRA remained fixed in the rear conjugate plane while the sample was translated within the image plane of the microscope, such that each frame of the images produced a unique combination of polarization-position mappings of the sample. The SHG image (**Figure 3.4A**) shows polarization modulation from the μRA. The yellow box serves as a fiducial marker to identify a feature relative to the modulation induced by translation through the polarization modulation pattern. As described previously, SHG images were stacked with pixel-to-pixel spatial correlation and unique polarization in each frame. The polarization-dependent SHG activity was recorded for each SHG-active pixel with a representative trace shown in **Figure 3.4C**, overlaid with a plot of intensity predicted by the fitted tensor elements.

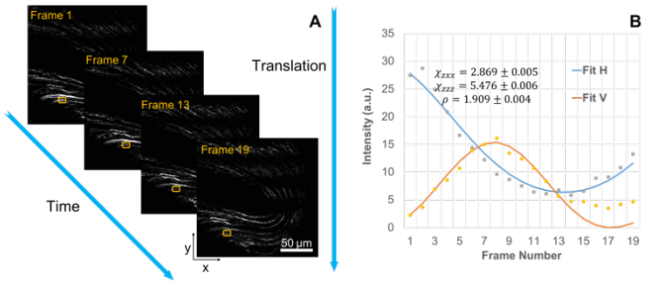

Figure 3.4 Translation-based spatially encoded polarization dependent NLO imaging. A) H-polarized SHG image of collagenous tissue in the first frame shown top left in the original location, with nominal translation of 30 μm increments to the final image. Each frame corresponds to a unique incident polarization on the same location in the tissue sample. B) Fit to the intensity of a single representative pixel as a function of frame number/polarization state. The highlighted box is intended to guide the eye for visualization of the intensity modulation. Dwell time for each pixel was 1.8 μs.

At each SHG-active location, the fitting procedure yielded the three nonzero independent local frame tensor elements accessible for collagen oriented within the FoV: χ_{zzz}, χ_{zxx}, and χ_{xxz}. The chiral element χ_{yzx}, while formally allowed by symmetry, is much smaller in magnitude than the other elements and becomes

completely inaccessible for collagen oriented with the Z axis (unique axis) flat within the image plane. Consistent with previous observations for collagen, approximation of $\chi_{zxx} \cong \chi_{xxz}$ has been made.[14–17]

Figure 3.5 contains the images obtained for the ratio of unique tensor elements $\rho \equiv \chi_{zzz} / \chi_{zxx}$, which serves as a metric for evaluating the degree of ordering within collagen fibers in disease diagnostics studies.[18,19] The distribution of measured ρ values exhibited a modal value of 1.2 and mean value of 1.46. These values are in close agreement with previously reported mouse tail tissue measured with rapid polarization modulation, supporting the general validity of the μRA for spatially-encoded polarization modulation SHG microscopy. [20,21]

The distribution of measurements values contains a long tail towards higher ratios of ρ, consistent with taking the ratio between random variables where measurement noise causes the denominator to approach zero. To evaluate the contribution of measurement noise to the recovered distribution of ρ, the relative uncertainty in the fitting parameters χ_{zzz} and χ_{zxx} were used as the standard deviations of simulated normal distributions with a ratio of means equal to 1.5. This ratio was chosen as it was the mean ρ value for tendon tissue in reference 21.[21] The recovered distribution of ρ for normally distributed parameters χ_{zzz} and χ_{zxx} are plotted and overlaid with the recovered distribution from the measurements. Measurement noise disproportionately affect the recovered distribution for a ratio of random numbers, however it is also true that the recovered distribution of ρ is sufficiently broad as to not be fully described by noise contributions. The resulting uncertainty due to the spread of the simulated distribution is 0.2. For these particular data, minimal thresholding for selection of high SNR pixels was employed; pixels containing at least 0.5% of the maximum intensity and with greater than 80% of recorded frames containing signal are used. As a result, low SNR single-pixels for the 19-frame stack may have an additive effect on the recovery of the parameter ρ. It is also possible for two colocalized distributions of ρ

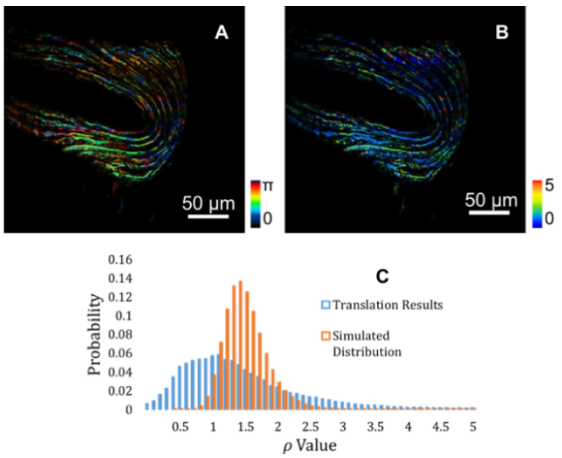

Figure 3.5 A) Converged orientation angle of collagen fibers within the FoV. B) Image of $\rho = \chi_{zzz}/\chi_{zxx}$, with a mean value of 1.46 and modal value of 1.2. C) Plot of the measured distribution of ρ, overlaid with a simulated distribution generated by taking the ratio of normal distributions with relative uncertainties equal to those recovered from the fit to the tensor elements.

to be present within the FoV, consistent with previous reports of collagen I and collagen III.[6] It is anticipated that the dominant source of SHG signal in the mouse tail tendon tissue analyzed is collagen I.

As polarization-dependent NLO microscopy is often utilized in thick samples that necessitate epi-imaging, it is worth discussing the compatibility of this approach with epi-detection. Dichroic mirrors inserted into the beam path for epi-detection will have perturbative effects on the polarization of light propagating to and from the sample plane. Fortunately, the corrections for the polarization perturbation are straight forward through the addition of two Jones matrices representing the dichroic mirror and its polarization transfer matrices for light propagating to and returning from the sample.

3.6 Conclusions

A novel SHG imaging method utilizing spatially encoded polarization modulation compatible with commercial beam-scanning microscopes was demonstrated. By placing a μRA in the rear-conjugate plane of a beam-scanning microscope, each pixel within the image plane was encoded with a polarization state distinct from its neighbors, varying in a sinusoidal pattern across the vertical axis of the image. Complementary image analysis techniques were used to extract local orientation of SHG-active structures. The experimental design leverages translation stages common to most microscopes to move the sample within the FoV, encoding a new polarization state on each position within the sample for each frame. This approach provides pixel-level tensor information, enabling tissue analysis for disease diagnostics with submicron-scale resolution. The method was applied to the model systems of z-cut quartz and rat tail tendon; good agreement with theory and previous experiment was observed. Although the present study focused on large field-of-view measurements using low NA objectives, extension to polarization analysis with high NA can be performed by incorporating position-dependent transformation matrices under conditions of tight focusing.[22] Irrespective of the tightness of focus, μRA measurements of polarization can simultaneously recover both conventional Mueller matrix and nonlinear optical images.

Future work will aim to reduce 1/f noise in the measurement by implementing image segmentation methods coupled with single frame acquisition in a snapshot type measurement. Imaging speed is a shared weakness between the polarization-rotation method and the spatially encoded approach demonstrated herein. The spatially encoded approach, however, has the ability to leverage spatial correlations within images for pooling of polarization analysis. Images are generally overdetermined, such that measurements at every

pixel are not necessarily required to recover high-quality image reconstructions. Consequently, in-painting can enable polarization analysis from a single image containing NLO-active structures large enough to span multiple polarizations. This approach would allow the evaluation of the NLO susceptibility for a single crystal or, e.g., collagen fiber, at speeds comparable to those attained with electro-optic modulators but is compatible to retrofitting within a commercial instrument.

3.7 References

1. Ranjit, S.; Dobrinskikh, E.; Montford, J.; Dvornikov, A.; Lehman, A.; Orlicky, D.; Nemenoff, R.; Gratton, E.; Levi, M.; Furgeson, S. Label-Free Fluorescence Lifetime and Second Harmonic Generation Imaging Microscopy Improves Quantification of Experimental Renal Fibrosis. *Kidney international* **2016**, *90* (5), 1123–1128.

2. Strupler, M.; Hernest, M.; Fligny, C.; Martin, J.; Tharaux, P.; Schanne-Klein, M. Second Harmonic Microscopy to Quantify Renal Interstitial Fibrosis and Arterial Remodeling. *Journal of biomedical optics* **2008**, *13* (5), 054041. https://doi.org/10.1117/1.2981830.

3. Hase, E.; Tanaka, R.; Fukushima, S.; Tasui, T. In Vivo Time-Series Monitoring of Dermal Collagen Fiber during Skin Burn Healing Using Second-Harmonic-Generation Microscopy. *Biomedical Imaging and Sensing Conference* **2018**, *10711*, 107111B.

4. Tanaka, R.; Fukushima, S.; Sasaki, K.; Tanaka, Y.; Murota, H.; Matsumoto, K.; Araki, T.; Yasui, T. In Vivo Visualization of Dermal Collagen Fiber in Skin Burn by Collagen-Sensitive Second-Harmonic-Generation Microscopy. *Journal of biomedical optics* **2013**, *18* (6), 061231. https://doi.org/10.1117/1.JBO.18.6.061231.

5. Golaraei, A.; Cisek, R.; Krouglov, S.; Navab, R.; Niu, C.; Sakashita, S.; Yasufuku, K.; Tsao, M.-S.; Wilson, B. C.; Barzda, V. Characterization of Collagen in Non-Small Cell Lung Carcinoma with Second Harmonic Polarization Microscopy. *Biomedical Optics Express* **2014**, *5* (10), 3562. https://doi.org/10.1364/BOE.5.003562.

6. Tilbury, K.; Lien, C.-H. H.; Chen, S.-J. J.; Campagnola, P. J. Differentiation of Col I and Col III Isoforms in Stromal Models of Ovarian Cancer by Analysis of Second Harmonic Generation Polarization and Emission Directionality. *Biophys. J.* **2014**, *106* (2), 354–365. https://doi.org/10.1016/j.bpj.2013.10.044.

7. Levental, K.; Yu, H.; Kass, L.; Lakins, J.; Egeblad, M.; Erler, J.; Fong, S.; Csiszar, K.; Giaccia, A.; Weninger, W.; et al. Matrix Crosslinking Forces Tumor Progression by Enhancing Integrin Signaling. *Cell* **2009**, *139* (5), 891–906.

8. Nadiarnykh, O.; Plotnikov, S.; Mohler, W. A.; Kalajzic, I.; Deborah, R.-B.; Campagnola, P. J. Second Harmonic Generation Imaging Microscopy Studies of Osteogenesis Imperfecta. *J Biomed Opt* **2007**, *12* (5), 051805. https://doi.org/10.1117/1.2799538.

9. Psilodimitrakopoulos, S.; Santos, S.; Amat-Roldán, I.; Nair, A.; Arigas-García, D.; Loza-Alvarez, P. In Vivo, Pixel-Resolution Mapping of Thick Filaments' Orientation in Nonfibrilar Muscle Using Polarization-Sensitive Second Harmonic Generation Microscopy. *Journal of Biomedical Optics* **2009**, *14* (1), 014001.

10. Hu, P.-S.; Ghazaryan, A.; Hovhannisyan, V.; Chen, S.-J.; Chen, Y.-F.; Kim, C.-S.; Tsai, T.-H.; Dong, C.-Y. Imaging of Biological Tissues with Pixel-Level Analysis of Second-Order Susceptibility. *J Biomed Opt* **2013**, *18* (3), 031102–031102. https://doi.org/10.1117/1.JBO.18.3.031102.

11. Schneider, C.; Rasband, W.; Elliceiri, K. NIH Image to ImageJ: 25 Years of Image Analysis. *Nature methods* **2012**, *9* (7), 671.

12. Rezakhaniha, R.; Agianniotis, A.; Schrauwen, J.; Griffa, A.; Sage, D.; Bouten, C.; van de Vosse, F.; Unser, M.; Stergiopulos, N. Experimental Investigation of Collagen Waviness and Orientation in the Arterial Adventitia Using Confocal Laser Scanning Microscopy. *Biomechanics and modeling in mechanobiology* **2012**, *11* (3–4), 461–473. https://doi.org/10.1007/s10237-011-0325-z.

13. Dow, X. Y.; L, D., Emma; Newman, J. A.; Dettmar, C. M.; Simpson, G. J. Unified Theory for Polarization Analysis in Second Harmonic and Sum Frequency Microscopy. *Biophys J* **2016**, *111* (7), 1553–1568. https://doi.org/10.1016/j.bpj.2016.04.019.

14. Gusachenko, I.; Tran, V.; Houssen, Y.; Allain, J.-M.; Marie-Claire, S.-K. Polarization-Resolved Second-Harmonic Generation in Tendon upon Mechanical Stretching. **2012**, *102* (9), 2220–2229.

15. L, D., Emma; Sullivan, S. Z.; Schmitt, P. D.; Muir, R. D.; Simpson, G. J. Polarization-Modulated Second Harmonic Generation Ellipsometric Microscopy at Video Rate. *Anal Chem* **2014**, *86* (16), 8448–8456. https://doi.org/10.1021/ac502124v.

16 Burke, M.; Golaraei, A.; Atkins, A.; Akens, M.; Barzda, V.; Whyne, C. Collagen Fibril Organization within Rat Vertebral Bone Modified with Metastatic Involvement. *Journal of structural biology* **2017**, *199* (2), 153–164.

17. Ding, C.; Ulcickas, J.; Deng, F.; Simpson, G. Second Harmonic Generation of Unpolarized Light. *Physical review letters* **2017**, *119* (19), 193901.

18. Tokarz, D.; Cisek, R.; Golaraei, A.; Krouglov, S.; Navab, R.; Niu, C.; Sakashita, S.; Yasufuku, K.; Tsao, M.-S.; Asa, S. L. Tumor Tissue Characterization Using Polarization-Sensitive Second Harmonic Generation Microscopy. **2015**, *9531*, 95310C.

19. Su, P.-J.; Chen, W.-L.; Hong, J.-B.; Li, T.-H.; Wu, R.-J.; Chou, C.-K.; Chen, S.-J.; Hu, C.; Lin, S.-J.; Dong, C.-Y. Discrimination of Collagen in Normal and Pathological Skin Dermis through Second-Order Susceptibility Microscopy. *Opt Express* **2009**, *17* (13), 11161. https://doi.org/10.1364/OE.17.011161.

20. Dow, X. Y.; L, D., Emma; Sullivan, S. Z.; Schmitt, P. D.; Ulcickas, J.; Simpson, G. J. Imaging the Nonlinear Susceptibility Tensor of Collagen by Nonlinear Optical Stokes Ellipsometry. *Biophys J* **2016**, *111* (7), 1361–1374. https://doi.org/10.1016/j.bpj.2016.05.055.

21. Romijn, E.; Finnøy, A.; Lilledahl, M. Analyzing the Feasibility of Discriminating between Collagen Type I and II Using Polarization Resolved Second Harmonic Generation. *Journal of biophotonics* **2018**, e201800090. https://doi.org/10.1002/jbio.201800090.

22. Simpson, G. *Nonlinear Optical Polarization Analysis in Chemistry and Biology*; Cambridge University Press, 2017.

CHAPTER 4. SECOND HARMONIC GENERATION OF UNPOLARIZED LIGHT

The contents of this chapter are in large part adapted from the paper Second Harmonic Generation Of Unpolarized Light, originally published in *Physical Review Letters* in 2017.[1]

4.1 Introduction

The previous chapters of this thesis have applied the Jones formalism for interpreting polarization-dependent NLO methods. The Jones framework is relatively intuitive, but lacks the ability to characterize partially or wholly unpolarized fields which are common when measuring optical response in turbid media. Depolarization induced by the sample is common in biomedical imaging, particularly for interpretation of *in vivo* measurement, and complicates subsequent polarization analysis. Fundamentally this depolarization occurs from cumulative scattering, birefringence, and linear and circular dichroism effects. [2-4] Different methods have been explored to counter these effects. Samples can be prepared with optical clearing methods to mitigate the effects of scattering on polarization via refractive index matching.[5]. In thick tissue samples up to depths of 100 μm, strategies that track changes in linear polarization state have attempted to reduce bias in the recovered tensor elements.[2-4]While largely successful, these methods do not account for the influence of depolarization which occurs as light propagates to the focal plane. Mathematical frameworks based upon foundational work by Mclain and Shi, such as the one introduced by Barzda and coworkers, have been proposed to address this problem.[6-8] Application of the super-Mueller matrix approach has been successful in measuring polarization dependent SHG from crystals and collagen fibrils, but the approach requires the direct measurement of all 36 unique elements within the super-Mueller matrix.[9-10] An alternative approach proposed by Simpson bridges the Mueller tensor architecture capable of tracking polarization for partially polarized fields.[11] This approach greatly simplifies analysis of Mueller tensors by mapping them back to the Jones tensor.

This chapter will lay out the fundamentals of the Stokes-Mueller formalism for polarization analysis. The Stokes-Mueller formalism is a general linear algebra for tracking polarization transfer through an optical system. Contrary to the Jones framework described in chapter 2 which

transfer through an optical system. Contrary to the Jones framework described in chapter 2 which is incapable of describing depolarized fields, the Stokes framework can describe depolarized states. Furthermore, by leveraging this generality in the Stokes framework complex polarization states can be described as a linear combination of purely polarized and fully depolarized components with a single adjustable parameter. Bridging these two frameworks will be key to interpreting polarization-dependent measurements with partial depolarization, as the Stokes framework will provide robustness to depolarization while the Jones framework will provide a more intuitive context in which to interpret the underlying nonlinear optical properties.

4.2 Connection of the Stokes and Mueller Calculus to the Jones Calculus

4.2.1 Stokes Vectors and Mueller Matrices

Analogous to the Jones framework of polarization analysis, the Stokes-Mueller formalism allows for the mathematical treatment of polarization changes as light propagates through an optical system. The Stokes vector maps polarization through a series of intensity values, enabling the treatment of poorly defined polarization states, but as a consequence is a more complex structure for mapping polarization. Equation (5.1) defines the Stokes vector.

$$\vec{s} = \begin{pmatrix} I_H + I_V \\ I_H - I_V \\ I_{+45} - I_{-45} \\ I_R - I_L \end{pmatrix} \tag{5.1}$$

The Stokes vector can be constructed from the Jones vector using the transformation matrix A, defined in equation (5.2) below. The $\otimes$ symbol denotes a Kronecker product.

$$\vec{s} = \begin{bmatrix} 1 & 0 & 0 & 1 \\ 1 & 0 & 0 & -1 \\ 0 & 1 & 1 & 0 \\ 0 & i & -i & 0 \end{bmatrix} \cdot \begin{pmatrix} \vec{e}_0^{\,*}\vec{e}_0 \\ \vec{e}_0^{\,*}\vec{e}_1 \\ \vec{e}_1^{\,*}\vec{e}_0 \\ \vec{e}_1^{\,*}\vec{e}_1 \end{pmatrix} = A \cdot \left(\vec{e}^{\,*} \otimes \vec{e} \right) \tag{5.2}$$

Polarization changes due to linear processes can be mapped using Mueller matrices. Equation (5.3) below illustrates.

$$\vec{s}_{out} = M \cdot \vec{s}_{in} \tag{5.3}$$

For nondepolarizing linear processes the Mueller matrix can be constructed directly from the Jones matrix for an analogous optic. This process is a linear extension of the mapping from Jones vectors to Stokes vectors in higher dimension. Equation (5.4) below illustrates.

$$M = A \cdot \left(J^* \otimes J \right) \cdot A^{-1} \tag{5.4}$$

As a brief illustration of the procedure, consider the modeling of a quarter waveplate. A quarter waveplate can be defined in the Jones formalism according to equation (5.5).

$$J_{QWP} = \begin{pmatrix} 1 & 0 \\ 0 & e^{-i\frac{\pi}{2}} \end{pmatrix} \tag{5.5}$$

Constructing the Mueller matrix M_{QWP} can be achieved as shown in equation (5.4), demonstrated below.

$$M_{QWP} = A \cdot \left({J_{QWP}}^* \otimes J_{QWP} \right) \cdot A^{-1} = \begin{bmatrix} 1 & 0 & 0 & 0 \\ 0 & 1 & 0 & 0 \\ 0 & 0 & 0 & -1 \\ 0 & 0 & 1 & 0 \end{bmatrix} \tag{5.6}$$

Inspecting the resulting matrix in the context of equation (5.1), it can be observed that total intensity and relative intensity of the H and V polarized light is conserved, while the intensity of s_3 is exchanged with the negative of s_4.

4.2.2 Mueller Tensors

Mapping polarization transfer in nonlinear optics requires the interaction of multiple fields, as described in Chapter 2. Just as in the case for Jones tensors, the Mueller tensor $\boldsymbol{M}^{(2)}$ maps the outgoing polarizations by taking a tensor product with the incident polarization vectors. Equation (5.7) below demonstrates for the specific case of SHG, where $\vec{s}^{\,\omega}$ corresponds to the Stokes vector of the incident light, and $\vec{s}^{\,2\omega}$ corresponds to the second harmonic.

$$\vec{s}^{\,2\omega} = \boldsymbol{M}^{(2)} : \vec{s}^{\,\omega}\vec{s}^{\,\omega} \tag{5.7}$$

Where the 2nd rank tensor $M^{(2)}$ can be constructed from the Jones tensor $\chi_J^{(2)}$ as shown in (5.8).

$$\boldsymbol{M}^{(2)} = A \cdot \left(\chi_J^{(2)*} \otimes \chi_J^{(2)} \right) : A^{-1}A^{-1} \tag{5.8}$$

The tensor product describing 2nd order nonlinear processes is convenient from a mathematical perspective for modeling the phenomena, but in practice vectorising the Mueller tensor provides a more convenient method for analysis. This approach is exactly analogous to that described in C Chapter 2 for the Jones tensor. Each separate dimension of the Mueller tensor can be stacked, transforming the tensor from a $4\times4\times4$ to a 64×1. Once vectorized, the polarization transfer process can be modeled as in equation (5.9).

$$\vec{s}^{\,2\omega} = \left[I_4 \otimes \left(\vec{s}^{\,\omega}\right)^T \otimes \left(\vec{s}^{\,\omega}\right)^T \right] \cdot \vec{\boldsymbol{M}}_L \tag{5.9}$$

Note that in equation (5.9) a subscript L indicates the Mueller tensor probed within the laboratory reference frame. Section 5.3 below will discuss reference frame rotation which will enable some key insights upon which tensor elements contribute to SHG under specific symmetry constraints. A permutation matrix E enables mapping of the vectorized Jones tensor to the vectorized Mueller tensor. This matrix serves the purpose of reordering the Kronecker product $\vec{\chi}_J^{\,*} \otimes \vec{\chi}_J$ such that the correct tensor element product order occurs within the vectorized Mueller tensor; this result is equivalent to vectorising the Kronecker product $\chi_J^{(2)*} \otimes \chi_J^{(2)}$.[12] The complete expression connecting the Jones tensor to the incident and exiting Stokes vectors is shown in equation (5.10). Direct linear fitting to the tensor products can be obtained by including the symmetry matrix Q and invoking the identity $(A\cdot B)\otimes(A\cdot B) = (A\otimes A)\cdot(B\otimes B)$. Alternatively, equation (5.10) can be fit using a nonlinear optimization of the tensor values, such as one invoking the Levenberg-Marquardt algorithm.[13]

$$\begin{aligned} \vec{s}^{\,2\omega} &= \left[I_4 \otimes (\vec{s}^{\,\omega} \otimes \vec{s}^{\,\omega})^T \right] \cdot [A \otimes (A^{-1})^T \otimes (A^{-1})^T] \cdot E \cdot (\vec{\chi}_J^{\,*} \otimes \vec{\chi}_J) \\ &= \left[I_4 \otimes (\vec{s}^{\,\omega} \otimes \vec{s}^{\,\omega})^T \right] \cdot [A \otimes (A^{-1})^T \otimes (A^{-1})^T] \cdot \overline{\left(\chi_J^{(2)*} \otimes \chi_J^{(2)} \right)} \end{aligned} \tag{5.10}$$

4.2.3 Reference Frame Rotation

In Chapter 2, reference frame rotation was discussed in the context of the Jones framework for polarization analysis. This section serves as an extension of that work. All changes in reference frame handled within the Stokes-Mueller framework is equivalent to that discussed in section 2.1.3; refer to chapter 2 for Jones-frame rotation definitions. For simplicity, only the azimuthal orientation of the sample will be considered here. Handling tilt and twist angles can be achieved

in the the Mueller-Stokes framework through the same procedure described in section 2.1.2. Rotating a Mueller tensor in its vectorized form can be achieved as shown in equation (5.11).

$$\vec{\boldsymbol{M}}_L = \left(\boldsymbol{\mathcal{R}}_\phi \otimes \boldsymbol{\mathcal{R}}_\phi \otimes \boldsymbol{\mathcal{R}}_\phi\right) \cdot \vec{\boldsymbol{M}}_l \tag{5.11}$$

The matrix $\boldsymbol{\mathcal{R}}_\phi$ describes rotation about the azimuthal angle, rotating the Mueller tensor from the local reference frame of the sample to the laboratory reference frame probed by the instrument. $\boldsymbol{\mathcal{R}}_\phi$ is defined below.

$$\boldsymbol{\mathcal{R}}_\phi = A \cdot \left(R_\phi \otimes R_\phi\right) \cdot A^{-1} \tag{5.12}$$

R_ϕ is the Jones-frame rotation matrix for azimuthal orientation (see section 2.1.3). Substituting equation (5.11) into (5.10) yields (5.13).

$$\bar{s}^{2\omega} = \tfrac{1}{4}\left[I_4 \otimes \left(\bar{s}^{\omega}\right)^T \otimes \left(\bar{s}^{\omega}\right)^T\right] \cdot \left(\boldsymbol{\mathcal{R}}_\phi \otimes \boldsymbol{\mathcal{R}}_\phi \otimes \boldsymbol{\mathcal{R}}_\phi\right) \cdot \left[A \otimes \left(A^{-1}\right)^T \otimes \left(A^{-1}\right)^T\right] \cdot \overrightarrow{\left(\chi_l^{(2)*} \otimes \chi_l^{(2)}\right)} \tag{5.13}$$

Rearranging the Kronecker products in the middle terms as shown below

$$\left(\boldsymbol{\mathcal{R}}_\phi \otimes \boldsymbol{\mathcal{R}}_\phi \otimes \boldsymbol{\mathcal{R}}_\phi\right) \cdot \left[A \otimes \left(A^{-1}\right)^T \otimes \left(A^{-1}\right)^T\right] = \left[\left(\boldsymbol{\mathcal{R}}_\phi \cdot A\right) \otimes \left(\boldsymbol{\mathcal{R}}_\phi \cdot \left(A^{-1}\right)^T\right) \otimes \left(\boldsymbol{\mathcal{R}}_\phi \cdot \left(A^{-1}\right)^T\right)\right] \tag{5.14}$$

This rearrangement facilitates the following substitution.

$$\boldsymbol{\mathcal{R}}_\phi A = \left[A \cdot \left(R_\phi \otimes R_\phi\right) \cdot A^{-1}\right] A = A \cdot \left(R_\phi \otimes R_\phi\right) \tag{5.15}$$

This allows the simplification in (5.16).

$$\begin{aligned} &\left(\boldsymbol{\mathcal{R}}_\phi \otimes \boldsymbol{\mathcal{R}}_\phi \otimes \boldsymbol{\mathcal{R}}_\phi\right) \cdot \left[A \otimes \left(A^{-1}\right)^T \otimes \left(A^{-1}\right)^T\right] \\ &= \left[A \otimes \left(A^{-1}\right)^T \otimes \left(A^{-1}\right)^T\right] \cdot \left[R_\phi \otimes R_\phi \otimes R_\phi \otimes R_\phi \otimes R_\phi \otimes R_\phi\right] \end{aligned} \tag{5.16}$$

Equation (5.17) is the ultimate result of implementing the above simplification.

$$\begin{aligned} \bar{s}^{2\omega} = \tfrac{1}{4}&\left[I_4 \otimes \left(\bar{s}^{\omega}\right)^T \otimes \left(\bar{s}^{\omega}\right)^T\right] \cdot \left[A \otimes \left(A^{-1}\right)^T \otimes \left(A^{-1}\right)^T\right] \\ &\cdot \left[R_\phi \otimes R_\phi \otimes R_\phi \otimes R_\phi \otimes R_\phi \otimes R_\phi\right] \cdot \overrightarrow{\left(\chi_l^{(2)*} \otimes \chi_l^{(2)}\right)} \end{aligned} \tag{5.17}$$

4.2.4 Binary Count Indexing of Tensors

In the subsequent sections, a binary counting approach will be utilized to track the contribution of Jones tensor elements to the Mueller tensor. The primary utility in this approach occurs because only a subset of entries in the Kronecker product $\overrightarrow{\left(\chi_J^{(2)*} \otimes \chi_J^{(2)}\right)}$ contribute to the measured Stokes vector. Binary notation provides a convenient manner of tracking their ordering, due to the permutation that occurs when constructing the vectorized Mueller tensor from the Jones tensors.[14] It should be noted, however, that the vector $\overrightarrow{\left(\chi_J^{(2)*} \otimes \chi_J^{(2)}\right)}$ is not equivalent to the vector $\vec{\chi}_J^* \otimes \vec{\chi}_J$; the former places polarization permutations in ascending order with respect to binary counting, whereas the latter follows the block-matrix convention dictated by the Kronecker product process. **Figure 4.1** illustrates the difference between these two permutations. Considering the example in the figure, the tensor product with binary ordering 001011 (HHVHVV) is the 11th element of the product vector. If placed in ascending order, such that the binary count can be directly converted to a decimal position, this would correspond to a binary count of 000111. Permuting the indices of each binary representation as illustrated by the arrows in **Figure 4.1** enables mapping between these two formats. Practically this is achieved by incorporating the matrix E as described in reference 2.[12]

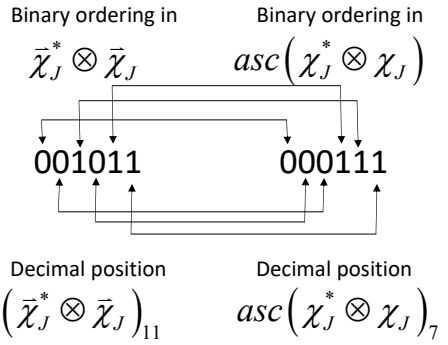

Figure 4.1 Illustration of permutative differences between Kroneckering the vectorized $\vec{\chi}_J$ and vectorising the Kroneckered tensor.

4.3 Application of the Framework for Depolarized Light

While the subsequent sections provide some context for applying Mueller tensor to polarization analysis, they do not clarify how one can leverage the framework practically. Recovery of the full Mueller tensor would be experimentally prohibitive, with a potential 64 unknown elements. Instead, this chapter aims to exploit some key attributes of the model to provide a framework for polarization analysis in both the extreme limit of fully depolarized light, as well as the continuum of partial polarizations that are typically accessible when measuring SHG in turbid media.

For depolarized light the Stokes vector of light is defined as in equation 7 below, with the only nonzero element corresponding to total intensity.

$$\vec{s}_{depol} = \begin{pmatrix} I_H + I_V \\ I_H - I_V \\ I_{+45} - I_{-45} \\ I_R - I_L \end{pmatrix} = \begin{pmatrix} 1 \\ 0 \\ 0 \\ 0 \end{pmatrix} \tag{5.18}$$

The depolarized stokes vector $\vec{s}_{depol}$ has direct implications upon the anticipated polarization of SHG. Using the first term in equation (5.10), it can be seen that depolarized light only probes four elements of the Mueller tensor. Using a counting approach to index, these elements are the M_{000}, M_{100}, M_{200}, and M_{300} elements.

$$\vec{s}^{\,2\omega}_{depol} = \boldsymbol{M}^{(2)} : \vec{s}^{\,\omega}_{depol}\vec{s}^{\,\omega}_{depol} = \begin{bmatrix} M_{000} \\ M_{100} \\ M_{200} \\ M_{300} \end{bmatrix}_{depol} \tag{5.19}$$

With the location of the relevant Mueller tensor elements defined according to the fixed value of the depolarized Stokes vector, these elements can be traced back to their origin in the Jones tensor using equation (5.8) or (5.10). Equation (5.10) can be rewritten using the identity $(A \cdot B) \otimes (A \cdot B) = (A \otimes A) \cdot (B \otimes B)$ and the associative properties of Kronecker products, yielding the following.

$$\vec{s}^{\,2\omega} = A \cdot \left\{ (I_4) \otimes \left[\left(\vec{s}^{\,\omega}\right)^T \otimes \left(\vec{s}^{\,\omega}\right)^T \cdot \left(A^{-1}\right)^T \otimes \left(A^{-1}\right)^T \right] \right\} \cdot \overline{\left(\chi_J^{(2)*} \otimes \chi_J^{(2)} \right)} \tag{5.20}$$

Regrouping the transpose operation outside of the curly braces in equation (5.20) and invoking the same Kronecker identity highlighted above yields the following.

$$\vec{s}^{\,2\omega} = A \cdot \left\{ I_4 \otimes \left(A^{-1} \cdot \vec{s}^{\,\omega} \right) \otimes \left(A^{-1} \cdot \vec{s}^{\,\omega} \right) \right\}^T \cdot \overline{\left(\chi_J^{(2)*} \otimes \chi_J^{(2)} \right)} \tag{5.21}$$

Recalling the matrix A first defined in equation (5.2), the product $A^{-1} \cdot \vec{s}^{\,\omega}$ can be calculated as $\frac{1}{2}\begin{bmatrix} 1 & 0 & 0 & 1 \end{bmatrix}^T$, while the Kronecker $\left(A^{-1} \cdot \vec{s}^{\,\omega} \right) \otimes \left(A^{-1} \cdot \vec{s}^{\,\omega} \right)$ yields a 16 element vector with nonzero entries in elements 0, 3, 12, and 15. Kroneckering by the identity I_4 reveals that the same 4 tensor element products contribute to each element of the outgoing Stokes vector $\vec{s}^{\,2\omega}$. Mapping these indices to their corresponding binary representation yields 000000, 000011, 001100, 001111,

respectively, which can then be interpreted in the context of $\overline{\left(\chi_J^{(2)*} \otimes \chi_J^{(2)}\right)}$. In binary notation, the rightmost digit corresponds to the rightmost index of $\chi_J^{(2)}$ and the 2nd from the right to the rightmost index of the complex conjugate $\chi_J^{(2)*}$. Each subsequent digit counts right to left in this same manner, such that 000011 corresponds to $\chi_{001}^{*}\chi_{001}$. Following this logic, 000000 maps to $\chi_{000}^{*}\chi_{000}$, 001100 to $\chi_{010}^{*}\chi_{010}$, and 001111 to $\chi_{011}^{*}\chi_{011}$. Explicit evaluation of the vectorized tensor element product yields equation (5.22) below. It is worth at this point acknowledging the mapping of binary notation back to the convention of H and V polarized light. This is as straightforward as replacing 0s with H, and 1s with V.

$$\vec{S}^{2\omega} = \tfrac{1}{4}\begin{bmatrix} 1 & 0 & 0 & 1 \\ 1 & 0 & 0 & -1 \\ 0 & 1 & 1 & 0 \\ 0 & i & -i & 0 \end{bmatrix}\begin{bmatrix} \chi_{000}^{*}\chi_{000} + \chi_{001}^{*}\chi_{001} + \chi_{010}^{*}\chi_{010} + \chi_{011}^{*}\chi_{011} \\ \chi_{000}^{*}\chi_{100} + \chi_{001}^{*}\chi_{101} + \chi_{010}^{*}\chi_{110} + \chi_{011}^{*}\chi_{111} \\ \chi_{100}^{*}\chi_{000} + \chi_{101}^{*}\chi_{001} + \chi_{110}^{*}\chi_{010} + \chi_{111}^{*}\chi_{011} \\ \chi_{100}^{*}\chi_{100} + \chi_{101}^{*}\chi_{101} + \chi_{110}^{*}\chi_{110} + \chi_{111}^{*}\chi_{111} \end{bmatrix} \tag{5.22}$$

A direct consequence of the deterministic nature of probing with depolarized light is that the scattered second harmonic is likely to be more polarized than the incident fundamental fields. Of course, this is dependent upon the system in question, but in general the NLO susceptibility will have some defined structure with varying amplitudes for the elements within. The interpretation becomes more nuanced when considering partially polarized fields. Ultimately, whether the process of SHG is depolarizing or hyperpolarizing is highly specific to the structure of $\boldsymbol{M}^{(2)}$, as well as the orientation of the sample with respect to the laboratory reference frame, and is discussed in detail in chapter 7. The Stokes vector of the second harmonic in such cases can be interpreted as a linear combination of responses from the purely polarized Mueller tensor $\boldsymbol{M}_{pol}^{(2)}$ and the depolarized contribution shown in equation (5.23) below.

$$\vec{S}^{2\omega} = \alpha \cdot \vec{S}_{depol}^{2\omega} + (1-\alpha)\cdot \vec{S}_{pol}^{2\omega} = \alpha \cdot \begin{bmatrix} M_{000} \\ M_{100} \\ M_{200} \\ M_{300} \end{bmatrix}_{depol} + (1-\alpha)\cdot \boldsymbol{M}_{pol}^{(2)} : \vec{S}_{in}^{\omega}\vec{S}_{in}^{\omega} \tag{5.23}$$

4.3.1 Specific Case: Uniaxial Symmetry with Fixed Orientation

Equation (5.22) is written in the reference frame of the measurement, or the laboratory frame, in which all six combinations of Jones tensor elements will generally be nonzero and unique for SHG. In the specific case of collagen oriented with the unique fiber axis coparallel with the laboratory horizontal axis, further reductions can be made. Inspection reveals only four nonzero contributing tensor products: $\left|\chi_{000}\right|^2$, $\left|\chi_{011}\right|^2$, $\left|\chi_{101}\right|^2$, and $\left|\chi_{110}\right|^2$. The degeneracy of incident fields in SHG brings further simplification, and the contributing unique nonzero elements reduce to $\chi_{000} = \chi_{z'z'z'}$, $\chi_{011} = \chi_{z'x'x'}$, and $\chi_{110} = \chi_{101} = \chi_{x'x'z'}$ Consistent with previous chapters, the primed notation indicates local reference frame coordinates; the z′ coordinate corresponds to the unique axis of the collagen fiber. Substituting these values into equation (5.22) yields (5.24).

$$\begin{bmatrix} S_0 \\ S_1 \\ S_2 \\ S_3 \end{bmatrix}^{2\omega} = \tfrac{1}{4}\begin{bmatrix} \left|\chi_{z'z'z'}\right|^2 + \left|\chi_{z'x'x'}\right|^2 + 2\left|\chi_{x'x'z'}\right|^2 \\ \left|\chi_{z'z'z'}\right|^2 + \left|\chi_{z'x'x'}\right|^2 - 2\left|\chi_{x'x'z'}\right|^2 \\ 0 \\ 0 \end{bmatrix}_{\phi=0} \tag{5.24}$$

The above expression can be generalized for arbitrary azimuthal angle. Explicit evaluation of terms to the left of the tensor product in equation (5.17) in combination with the nonzero values indicated in equation (5.22) yield the following equality.

$$\begin{bmatrix} \chi^*_{000}\chi_{000} + \chi^*_{001}\chi_{001} + \chi^*_{010}\chi_{010} + \chi^*_{011}\chi_{011} \\ \chi^*_{000}\chi_{100} + \chi^*_{001}\chi_{101} + \chi^*_{010}\chi_{110} + \chi^*_{011}\chi_{111} \\ \chi^*_{100}\chi_{000} + \chi^*_{101}\chi_{001} + \chi^*_{110}\chi_{010} + \chi^*_{111}\chi_{011} \\ \chi^*_{100}\chi_{100} + \chi^*_{101}\chi_{101} + \chi^*_{110}\chi_{110} + \chi^*_{111}\chi_{111} \end{bmatrix}$$

$$= \begin{bmatrix} \cos^2\phi & \cos^2\phi & \sin^2\phi & \sin^2\phi \\ \sin\phi\cos\phi & \sin\phi\cos\phi & -\sin\phi\cos\phi & -\sin\phi\cos\phi \\ \sin\phi\cos\phi & \sin\phi\cos\phi & -\sin\phi\cos\phi & -\sin\phi\cos\phi \\ \sin^2\phi & \sin^2\phi & \cos^2\phi & \cos^2\phi \end{bmatrix} \cdot \begin{bmatrix} \left|\chi_{z'z'z'}\right|^2 \\ \left|\chi_{z'x'x'}\right|^2 \\ \left|\chi_{x'z'x'}\right|^2 \\ \left|\chi_{x'x'z'}\right|^2 \end{bmatrix} \tag{5.25}$$

Substituting this relation into equation (5.22) and evaluating the product of the A matrix yields an expression which can be simplified using the trigonometric identities $2\sin\phi\cos\phi=\sin(2\phi)$ and $\cos^2\phi-\sin^2\phi=\cos(2\phi)$. Furthermore, noting $\left|\chi_{x'x'z'}\right|^2=\left|\chi_{x'z'x'}\right|^2$ yields the following equation.

$$\begin{bmatrix} s_0 \\ s_1 \\ s_2 \\ s_3 \end{bmatrix}^{2\omega} = \frac{1}{4}\begin{bmatrix} 1 & 1 & 1 \\ \cos(2\phi) & \cos(2\phi) & -\cos(2\phi) \\ -\sin(2\phi) & -\sin(2\phi) & \sin(2\phi) \\ 0 & 0 & 0 \end{bmatrix}\begin{bmatrix} \left|\chi_{z'z'z'}\right|^2 \\ \left|\chi_{z'x'x'}\right|^2 \\ 2\left|\chi_{x'x'z'}\right|^2 \end{bmatrix} \tag{5.26}$$

The equation detailed in (5.26) should be carefully considered. First, it is remarkable that for systems of uniaxial symmetry a fixed relationship between the nonlinear optical susceptibility and polarization of the resulting SHG exists. This fixed relationship between the Stokes vector of SHG produced from an unpolarized source has important implications for the utility of unpolarized light as a probe of material structure. If a relationship between the nonzero tensor elements is known *a priori*, only orientation is unknown in the above equation. Similarly, if orientation can be recovered by an orthogonal method, such as image analysis, only the relationship between the nonzero tensor elements governs the polarization of the second harmonic. Lastly, this result implies that unpolarized light may be used as a probe when the sample is anticipated to depolarize light, mitigating the effects of sample perturbation on the incident laser light yet still retaining structural information from polarization analysis of the second harmonic.

4.4 Experimental Methods

Imaging was conducted on a custom-built microscope utilizing an 80 MHz 100 fs Mai Tai Ti:Sapphire laser (SpectraPhysics) operating at 800nm as source. Beam-scanning microscopy was performed by pairing a resonant mirror operating at 8.8kHz (EOPC) with a galvanometer mirror synced such that 512 repetitions of the resonant mirror path occur for one ramp from the galvo mirror. The beam was then expanded to overfill the back of the objective and focused through a 10× 0.3 NA objective

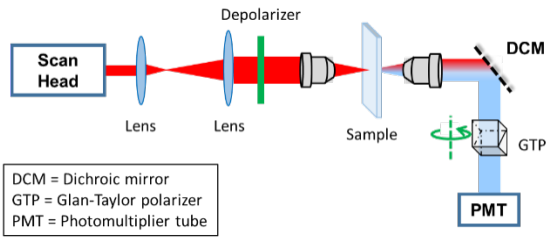

Figure 4.2 Instrument schematic for SHG transmittance measurements with depolarized excitation. Removal of the depolarizer results in pure linear excitation.

(Nikon) for measurements of Z-cut quartz and a 20× 0.4 NA (Nikon) objective for measurements of mouse tail sections. Scattered and transmitted light is collected by a 0.3 NA 10× condenser, and passed through a 4f configuration to deliver collimated light to the detection optics. Following collection through the condenser, light passes through a broadband wire grid depolarizer (0.2-2um, Thorlabs) placed in precision automated rotation stages (Universal Motion Controller, ESP300 and rotation mount, SR50CC, Newport). A dichroic mirror reflects the frequency doubled light, passing through a band pass filter (HQ 400/20m-2p Chroma Technology) and is detected on a photomultiplier tube (PMT, Hamamatsu H12310-40). The fundamental passes through the dichroic and is detected on a photodiode (DET10, Thorlabs). **Figure 4.2** portrays an abbreviated schematic.

4.5 Unpolarized Second Harmonic Generation from Z-cut Quartz

Z-cut quartz, as previously discussed in Chapter 2, is a convenient model system for exploring the consequences of the above predictions for SHG produced from an unpolarized source. For a thin crystal, the Euler angles θ is fixed, normal to the sample plane, while ψ is orientationally averaged for a uniaxial assembly. Consequently, only the azimuthal angle ϕ remains unknown and the equation (5.26) can be utilized to predict SHG intensity from Z-cut quartz. Furthermore, previous work has demonstrated the local frame tensor equality $\chi_{z'z'z'} = -\chi_{z'x'x'} = -\chi_{x'z'x'}$ for Z-cut quartz.[15] The equivalence $\left|\chi_{z'x'x'}\right| \cong \left|\chi_{x'x'z'}\right|$ enables the use of the tensor element ratio $\rho \equiv \chi_{z'z'z'} / \chi_{z'x'x'}$ to simplify the expression found in equation (5.26). The specific case of Z-cut quartz further reduces the total number of unknowns to 2, as ρ is fixed in this case.

$$\begin{bmatrix} s_0 \\ s_1 \\ s_2 \\ s_3 \end{bmatrix}^{2\omega} = \frac{\left|\chi_{z'x'x'}\right|^2}{4} \begin{bmatrix} 1 & 1 & 1 \\ \cos(2\phi) & \cos(2\phi) & -\cos(2\phi) \\ -\sin(2\phi) & -\sin(2\phi) & \sin(2\phi) \\ 0 & 0 & 0 \end{bmatrix} \begin{bmatrix} |\rho|^2 \\ 1 \\ 2 \end{bmatrix} \tag{5.27}$$

Note that the above expression also holds for thin sections of collagen, where the approximate equality $\left|\chi_{z'x'x'}\right| \cong \left|\chi_{x'x'z'}\right|$ has also been previously observed. The application of this framework for thin sections will be discussed in section 5.8.

SHG intensity detected through a rotating polarizer can then be modeled through equation (5.28); the constant C serves to normalize s_0 to unity, while the projection of the s_1 and s_2 elements onto the detector is purely a function of polarizer angle.

$$I^{2\omega}(\phi_{pol}) = \frac{C}{2}\left[s_0 + s_1\cos\left(2\phi_{pol}\right) - s_2\sin\left(2\phi_{pol}\right)\right] \tag{5.28}$$

The combination of equations (5.27) and (5.28) produces a function of both sample and polarizer orientation, shown below.

$$I^{2\omega}\left(\phi_{pol}\right) = \frac{C}{8}\left[\left(|\rho|^2 + 3\right) + \left(|\rho|^2 - 1\right)\cos\left(2\phi_{pol} - 2\phi\right)\right] \tag{5.29}$$

For Z-cut quartz the equality $\rho \equiv \chi_{z'z'z'}/\chi_{z'x'x'} = -1$ holds. Most interestingly, this has the direct consequence of removing the cosine term from equation (5.29) , suggesting constant SHG intensity as a function of analyzer angle. In other words, this theory predicts Z-cut quartz will radiate unpolarized light. Before exploring this consequence experimentally, it is important to distinguish this behavior from the polarization-dependent SHG radiated by Z-cut quartz when stimulated with linearly polarized light. Equation (5.30) details the anticipated SHG intensity as a function of analyzer and quartz orientation.[16]

$$I^{2\omega}\left(\phi, \phi_{pol}\right) = C \cdot \sin^2\left(3\phi - \phi_{pol}\right) \tag{5.30}$$

The 3-fold rotational symmetry within the Z-cut quartz gives rise to the factor of 3 inside of the sine modulated intensity profile, while overall intensity is scaled by a constant C. To evaluate the predicted intensity behavior for both linear and unpolarized incident light to Z-cut quartz, quartz was placed in a mechanical rotation stage and inserted into the sample plane of a beam-scanning nonlinear optical transmittance microscope. The instrument schematic can be found in **Figure 4.1**. Images were acquired for individual rotation angles of Z-cut quartz and the analyzer in increments of 3˚. Signal was averaged across the entire field of view.

Experimentally measured intensities and the corresponding fit to equation (5.30) are shown in **Figure 4.3**. In both experiments where the quartz is rotated **(Figure 4.3A)** and experiments where the polarizer is rotated (**Figure 4.3B**) the ratio $\rho = -1$ predicts zero modulation of SHG intensity when probed with unpolarized light. The solid purple line in each figure is a prediction based on this theory, and is not a fit to the experimental data. This response is consistent with the second harmonic generation of unpolarized light, despite the slight offset in predicted intensity for the depolarized light when rotating the quartz. This offset was attributed to uncertainty in the amplitude determined from the fits of the traces observed with a purely polarized incident field. Overall, excellent agreement between the observed and predicted intensity trends supports the validity of assumptions made in deriving equation (5.29).

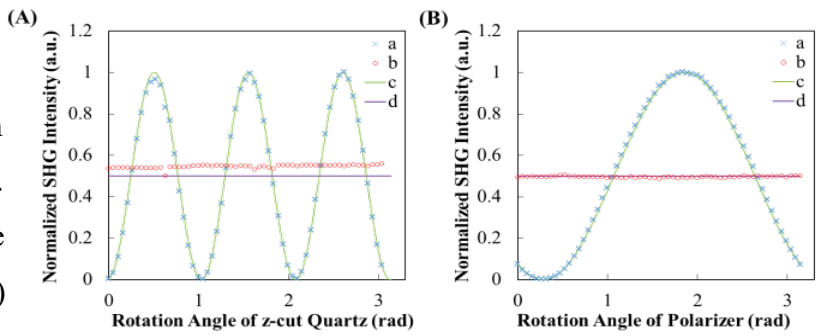

Figure 4.3 (A) Polarization dependent measurement of SHG signal from z-cut quartz at an arbitrary angle under (a) vertically polarized and (b) depolarized incident light overlay with theoretical (c) fitting and (d) prediction. (B) Measurements of horizontally polarization SHG signals from z-cut quartz at different azimuthal angle under (a) vertically polarized and (b) depolarized incident light, with theoretical (c) fitting and (d) prediction.

4.6 Application to Thin Collagenous Tissue

With the theoretical predictions of the model corroborated by experiment for the relatively simple system of Z-cut quartz, the framework was applied to the more complex system of collagen, where the ratio $\rho \equiv \chi_{z'z'z'} / \chi_{z'x'x'}$ is not predicted to be unity. Inspection of equation (5.29) shows intensity in a single pixel is a function of both local tensor ratio (ρ) and collagen orientation (ϕ); fitting to equation (5.29) yields the images shown in **Figure 4.4A-B**.

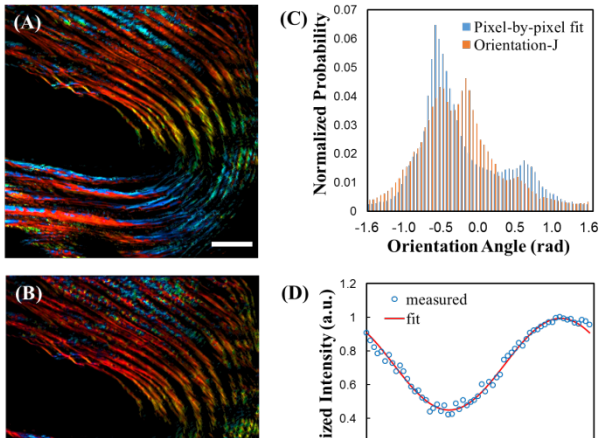

Figure 4.4 Orientation images of the azimuthal angle for a single FoV of mouse tail section from (A) the pixel-by-pixel nonlinear fit analysis and (B) *OrientationJ*. Scale bar: 100 μm. (C) The histogram of the orientation distribution achieved from pixel-by-pixel fit and *OrientationJ*. (D) Nonlinear fitting results of depolarized light excitation SHG for signal random pixel.

Unlike the trends observed from Z-cut quartz in **Figure 4.4**, **Figure 4.4D** shows clear intensity differences as a function of polarizer angle, consistent with $\rho \neq 1$.

In addition to fitting directly to collagen orientation, a separate measure of azimuthal orientation as assessed by image analysis through *OrientationJ* in ImageJ was conducted.[17-18] *OrientationJ* retrieves local orientation for structures within the image via contextual analysis with adjacent pixels, allowing orientation to be measured from either bright field or SHG images. Comparison of the recovered orientation distributions through both methods is shown in **Figure 4.5C**, yielding overall good agreement between the two orthogonal methods.

The origin of subtle differences between *OrientationJ* and polarization analysis in the recovered orientation distribution is worth discussing. The depolarizer functions by imposing a sinusoidal modulation in polarization state across the cross-section of the propagating laser beam. When this beam subsequently passes through an objective it undergoes a spatial Fourier transform, yielding a double-delta function at the object plane of the microscope. This double-delta is a horizontally offset two-spot point spread function, which produces slight doubling in the recorded image. This doubling can be noted in **Figure 4.4A-B**. For homogeneous samples like Z-cut quartz, this introduces no additional complexity into the measurement. However, for structures of finite thickness, such as collagen, if the dual-focus probes two adjacent fibers, or only probes a fiber with one of the two spots at a time, the resultant SHG may not be occurring from a fully depolarized source. In the above experiments the depolarizer was carefully aligned within the microscope to induce the offset along the horizontal axis of the image. This configuration enabled polarization analysis for fibers that were aligned horizontally or vertically with respect to the field of view, and comparison of recovered ϕ provided a probe for the existence of potential bias. If the double-focus were systematically biasing measured ϕ, then perturbations to recovered orientation should be greater for the vertically aligned fibers relative to results obtained from *OrientationJ*. Comparable deviations in recovered ϕ were observed for both sets of fibers, suggesting a lack of systematic bias induced by the double-focus. The overall agreement between *OrientationJ* image analysis and polarization analysis to recover fiber orientation provides evidence for its validity in previous chapters.

Polarization analysis provides a measure of ρ, the modal value of which was recovered to be 1.69 for the field of view in **Figure 4.4A**.This result is in good agreement with previous reports of structural collagen in mouse tail, chicken wing, and human dermis. [4, 19] The implicit assumption in the above analysis of polar tilt angle $\theta = \pi/2$, i.e., fibers lay flat within the focal plane, may provide one additional explanation for deviations between orientations obtained from *OrientationJ* and those retrieved from polarization analysis. Practically it is quite improbable to obtain a section which bisects all fibers parallel to the unique axis. While image analysis does not provide a method to assess polar tilt, polarization-dependent SHG may provide a probe sensitive to polar orientation.

While direct fitting to retrieve ρ, θ, and ϕ is complicated by covariance associated with each parameter, a stepwise approach can be taken to retrieve polar angle. In the preceding analysis, azimuthal orientation and ρ were both taken as unknowns. Assuming a fixed local frame tensor ratio ρ_l enables the interpretation of measured intensities as the result of projecting the local frame ratio ρ_l onto the laboratory frame ratio ρ. In terms of the Jones tensor elements, these projections from $\chi_{z'z'z'}$ and $\chi_{z'x'x'}$ onto laboratory frame χ_{XXX} and χ_{XYY} are shown below.

$$\begin{aligned} \chi_{XXX} &= \chi_{z'z'z'} \cdot \sin^3\theta + 3\chi_{x'x'z'} \cdot \sin\theta \cdot \cos^2\theta \\ \chi_{XYY} &= \chi_{x'x'z'} \cdot \sin\theta \end{aligned} \tag{5.31}$$

The laboratory frame ratio $\rho \equiv \chi_{XXX} / \chi_{XYY}$ can then be computed. Noting that $\rho_l \equiv \chi_{z'z'z'} / \chi_{z'x'x'}$, the ratio can be simplified to equation (5.32).

$$\sin^2\theta = \frac{\rho - 3}{\rho_l - 3} \tag{5.32}$$

Solving this equation for θ yields the following.

$$\theta = \arcsin\left(\sqrt{\frac{\rho - 3}{\rho_l - 3}}\right) \tag{5.33}$$

A per-pixel fit to equation (5.33) was conducted assuming a local-frame susceptibility ratio $\rho_l = 1.7$ based on previously reported values of $\rho_l = 1.7$ in the literature and aligning closely with the most probable value recorded in the current assessment.[15, 20] **Figure 4.5A-B** show the image of recovered laboratory frame ratio ρ and out-of-plane tilt angle θ retrieved from fitting to equation (5.33). A large subset of the population was observed to adopt a tilt angle of $\theta = \pi/2$. Note that the measurement contains an implicit bias against tilt angles of $\theta = 0$, because fibers aligned parallel with the optical axis are symmetry forbidden for production of coherent SHG. Qualitatively similar results were observed for fits to θ with an assumed $\rho_l = 1.4$ derived from other reports of local-frame tensor measurement.

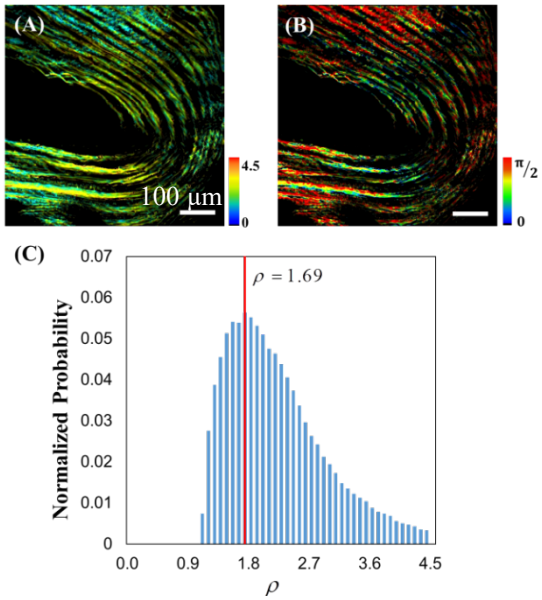

Figure 4.5 (A) The measured laboratory-frame ratio images for a single FoV of mouse tail section from the per-pixel fit analysis. (B) The polar tilt angle image recovered from the measured laboratory-frame ratio ρ for the same FoV with $\rho_l = 1.7$. (C) The distribution of the ratio ρ, with the maximum peak marked at 1.69.

4.7 Conclusions

The connection of the Stokes-Mueller calculus to the Jones calculus outlined in this chapter provides a handle for interpreting SHG in the presence of depolarization. The limiting case of fully depolarized incident fields was explored from both a predictive theoretical perspective and experimentally. An instrument for imaging SHG produced from unpolarized light was described, where unpolarized light was generated by placing a microretarding array in the Fourier plane of a beam scanning microscope, which induced varying rotation of the incident fields across the cross-section of the beam; focusing this pattern of intensities down to a point in the focal plane results in a spot with many field orientations superimposed. Most intriguingly, SHG of unpolarized light was predicted and observed from thin Z-cut quartz crystals exhibiting limited birefringence. The unique case of $\rho \equiv \chi_{z'z'z'}/\chi_{z'x'x'} = -1$ for Z-cut quartz gives rise to this phenomenon, which was

not observed for collagen in mouse tail sections. In contrast, the non-unity value of $\|\rho\|^2$ for collagen yields polarized SHG when unpolarized laser light is incident to the sample. A model predicting SHG intensity as a function of the tensor element ratio ρ and azimuthal orientation ϕ was generated for structures of uniaxial symmetry and fitting to this model enabled single-pixel recovery of both parameters. Relaxing the assumption of a fixed polar tilt angle θ, but subsequently applying the assumption of a single population mean ρ_1 allowed single-pixel recovery of θ. Analysis of θ revealed the modal fiber was oriented in-plane, with $\theta = \pi/2$, but significant portions of the tissue exhibited out-of-plane tilt. Crimped fibers found near bends in the tendon structure exhibited the largest out-of-plane tilt. This approach, despite reducing the potential information content of polarized SHG by scrambling the incident polarizations, showed great utility in probing the local structure of collagen fibers.

Arguably the most intriguing aspect of the experiments reported within this chapter is the generation of SHG from unpolarized light. Previous work utilizing SHG in turbid media, such as in *in vivo* or thick tissue segments, has largely ignored the contribution of scattered and depolarized light incident to the focal plane to detected SHG signal. This result has interesting implications, in using unpolarized light as a probe which is not affected by heterogeneity and depolarizing induced as light propagates to the focal plane. In thick tissues birefringence may repolarize the light as it propagates to the object plane. However, depolarization induced by varying phase delays across the cross-section of the beam incurred by refractive index changes associated with organelles and subcellular structures can be mitigated in this regime.

The framework described and applied in this chapter is not limited to the fully unpolarized case, however, as alluded to with equation (5.23). This chapter has served to lay the foundation for polarization analysis in nonlinear optics with partially polarized light. The subsequent chapter will leverage this framework and apply it to real samples where depolarization is not artificially induced, but rather caused by the sample itself.

4.8 References

1. Ding, C.; Ulcickas, J. R. W.; Deng, F.; Simpson, G. J., Second Harmonic Generation of Unpolarized Light. *Physical Review Letters* **2017,** *119* (19), 193901.

2. Gusachenko, I.; Latour, G.; Schanne-Klein, M. C., Polarization-resolved Second Harmonic microscopy in anisotropic thick tissues. *Opt Express* **2010,** *18* (18), 19339-52.

3. Gusachenko, I.; Tran, V.; Goulam Houssen, Y.; Allain, J. M.; Schanne-Klein, M. C., Polarization-resolved second-harmonic generation in tendon upon mechanical stretching. *Biophys J* **2012,** *102* (9), 2220-9.

4. Dow, X. Y.; DeWalt, E. L.; Sullivan, S. Z.; Schmitt, P. D.; Ulcickas, J. R.; Simpson, G. J., Imaging the Nonlinear Susceptibility Tensor of Collagen by Nonlinear Optical Stokes Ellipsometry. *Biophys J* **2016,** *111* (7), 1361-1374.
5. Nadiarnykh, O.; Campagnola, P. J., Retention of polarization signatures in SHG microscopy of scattering tissues through optical clearing. *Optics express* **2009**.

6. Samim, M.; Krouglov, S.; Barzda, V., Nonlinear Stokes-Mueller polarimetry. *Physical Review A* **2016**.

7. Shi, Y. M.; Mcclain, W. M.; Harris, R. A., An Extension of the Mueller Scattering Matrix to Nonlinear Light-Scattering. *Chem Phys Lett* **1993,** *205* (1), 91-95.

8. Shi, Y. M.; Mcclain, W. M.; Harris, R. A., Generalized Stokes-Mueller Formalism for 2-Photon Absorption, Frequency-Doubling, and Hyper-Raman Scattering. *Phys Rev A* **1994,** *49* (3), 1999-2015.

9. Burke, M.; Golaraei, A.; Atkins, A.; Akens, M.; Barzda, V.; Whyne, C., Collagen fibril organization within rat vertebral bone modified with metastatic involvement. *J Struct Biol* **2017,** *199* (2), 153-164.

10. Cisek, R.; Tokarz, D.; Steup, M.; Tetlow, I. J.; Emes, M. J.; Hebelstrup, K. H.; Blennow, A.; Barzda, V., Second harmonic generation microscopy investigation of the crystalline ultrastructure of three barley starch lines affected by hydration. *Biomedical Optics Express* **2015,** *6* (10), 3694-3700.

11. Simpson, G. J., Connection of Jones and Mueller Tensors in Second Harmonic Generation and Multi-Photon Fluorescence Measurements. *J Phys Chem B* **2016,** *120* (13), 3281-302.

12. Simpson, G. J., Connection of Jones and Mueller Tensors in Second Harmonic Generation and Multi-Photon Fluorescence Measurements. *The Journal of Physical Chemistry B* **2016,** *120* (13), 3281-3302.

13. Levenberg, K., A METHOD FOR THE SOLUTION OF CERTAIN NON-LINEAR PROBLEMS IN LEAST SQUARES. *Quarterly of Applied Mathematics* **1944,** *2* (2), 164-168.

14. Azzam, R. M. A.; Bashara, N. M., *Ellipsometry and Polarized Light*. Elsevier: Amsterdam, 1987.

15. Dow, Ximeng Y.; DeWalt, Emma L.; Sullivan, Shane Z.; Schmitt, Paul D.; Ulcickas, James R. W.; Simpson, Garth J., Imaging the Nonlinear Susceptibility Tensor of Collagen by Nonlinear Optical Stokes Ellipsometry. *Biophysical Journal* **2016,** *111* (7), 1361-1374.

16. Dow, Ximeng Y.; DeWalt, Emma L.; Newman, Justin A.; Dettmar, Christopher M.; Simpson, Garth J., Unified Theory for Polarization Analysis in Second Harmonic and Sum Frequency Microscopy. *Biophysical Journal* **2016,** *111* (7), 1553-1568.

17. Püspöki, Z.; Storath, M.; Sage, D.; Unser, M., Transforms and Operators for Directional Bioimage Analysis: A Survey. In *Focus on Bio-Image Informatics*, De Vos, W. H.; Munck, S.; Timmermans, J.-P., Eds. Springer International Publishing: Cham, 2016; pp 69-93.

18. Schneider, C. A.; Rasband, W. S.; Eliceiri, K. W., NIH Image to ImageJ: 25 years of image analysis. *Nature Methods* **2012,** *9* (7), 671-675.

19. Chen, W.; Li, T.; Su, P.; Chou, C.; Fwu, P. T.; Lin, S.; Kim, D.; So, P. T. C.; Dong, C., Second harmonic generation χ tensor microscopy for tissue imaging. *Applied Physics Letters* **2009,** *94* (18), 183902.

20. Burke, M.; Golaraei, A.; Atkins, A.; Akens, M.; Barzda, V.; Whyne, C., Collagen fibril organization within rat vertebral bone modified with metastatic involvement. *Journal of Structural Biology* **2017,** *199* (2), 153-164.

CHAPTER 5. MUELLER TENSOR NONLINEAR OPTICAL POLARIZATION ANALYSIS IN TURBID MEDIA

The contents of this chapter are adapted from the publication Mueller Tensor Nonlinear Optical Polarization Analysis in Turbid Media, originally published in *The Journal of Physical Chemistry B* in 2019.[1]

5.1 Introduction

Nonlinear optical microscopies including second harmonic generation (SHG) and two-photon excited fluorescence (TPEF) provide high contrast within turbid media, supporting analysis of biologically relevant systems. The quadratic power dependence of signal on the incident intensity generally confines the emitted signal to the focal plane, enabling optical sectioning without confocal detection. The ability to use near infrared (IR) incident light further reduces scattering losses for imaging deeply within biological structures i.e., tissue samples. Endogenous expression of mutants hybridized with fluorescent proteins has lent itself to imaging a variety of protein targets, including mBlueberry1, EGFP, and mCherry, among others, as well as its use with Ca^{2+} binding fluorescent tags for monitoring neural activity.[2,3] The intrinsic fluorescence of aromatic amino acid residues has enabled its routine use in *in vivo* imaging of microvasculature, as well as NADH metabolism.[4,5] While the generality of TPEF makes it a flexible imaging modality for biologically relevant systems, SHG provides a symmetry specific contrast mechanism with lower background without the need for labeling. The selection rules for SHG necessitate a noncentrosymmetric structure, as can be found in the form of collagen networks in the extracellular matrix and myosin assemblies in muscle fibers. SHG has been employed to study the organization of collagen, which has been previously demonstrated to correlate with expression of several diseases, including lung, ovarian, and breast cancers.[6–8]

Polarization dependence allows the expansion of these methods to unique chemical problems, for example, polarization-resolved TPEF has been utilized previously to distinguish amorphous from crystalline proteins in the field of structural biology.[9] Polarization resolved SHG has been utilized to image biological structures such as collagen and myosin while obtaining information about molecular organization.[10,11] Collagen is the primary structural element of the extracellular matrix,

composed of a supramolecular assembly of collagen triple helices oriented uniaxially to form a fibril, with many fibrils contained in a single fiber. The relative orientation of collagen triple helices with respect to the fibril axis, and consequently, fiber axis, dictates the relative contribution of the molecular hyperpolarizability to the NLO susceptibility tensor. It has previously been demonstrated that the local order, i.e., distribution of triple helix tilt angles with respect to fiber axis, is altered with pathological expression of certain disease states and can thus be probed by polarization sensitive SHG microscopy.[6,7,12]

Despite the clear benefits of polarization analysis in SHG and TPEF microscopy, implementation in vivo is frustrated by turbidity and birefringence, which complicate polarization analysis in multiple ways. In the case of both protein crystal imaging and thick tissue imaging, the sample plane may lie embedded within the scattering medium. Thus, propagation of light to the sample plane may cause depolarization to occur prior to SHG due to mixing of polarization states. Furthermore, for backscattering imaging geometries or cases where the nonlinear signal must propagate through a substantial path length of tissue prior to detection, the SHG can be further depolarized. Several methods have been developed to combat this complication. In 2010, Schanne-Kleine and coworkers utilized simultaneous detection of backscattered and transmitted SHG and fundamental to quantify the interplay between birefringence and collagen structure, however, this work did not address the effect of homogeneous scattering.[13] More recently, adaptive optics and phase-only wavefront shaping have been employed to shape the polarization of the incident light to deliver pure polarizations at the sample plane beneath turbid media to account for scattering occurring prior to SHG.[14] Alternative methods utilize theoretical modeling to predict NLO signal in the presence of depolarization, such that changes in polarization due to structure of the NLO susceptibility tensor may be disentangled from scattering and birefringence effects upon the incident beam. The classical Jones framework to describe linear, and later, nonlinear optics is insufficient to describe the polarization state of partially polarized light. To account for this deficiency, Shi, McClain, and Harris extended the more general Stokes-Mueller framework to nonlinear optics.[15,16] Recent efforts by Barzda have extended these theoretical models to account for depolarization induced by the sample during measurement with the double Mueller matrix approach, which has been applied to studies of collagen.[17,18] Recently, a complementary framework was developed by Simpson and coworkers, connecting the intuitive

Jones framework to the more general Stokes framework.[19] This latter Mueller tensor framework provides the means to bridge measured Stokes vectors with the Jones tensor describing the NLO susceptibility. The complexity of the vectorized tensor determining SHG activity is thus reduced from 64 in the Mueller framework to 8 in the Jones framework. We have demonstrated the validity of the Jones/Mueller framework in the limit of a completely depolarized fundamental, showing excellent predictive capacity for the model system of Z-cut quartz and enabling the recovery of the tensor element ratio ρ as well as orientation of collagen fibers in a thin tissue section of mouse tail.[20]

The work detailed herein utilizes the Mueller tensor framework for recovering structural information from SHG microscopy in thick tissue sections, where depolarization is significant. SHG produced from collagen embedded in 5, 40, and 70 μm thick mouse tail tendon sections was measured and its polarization analyzed via a rotating quarter wave plate (QWP) and wire grid polarizer. As light propagates to the focal plane through the tissue, scattering and birefringence alter the incident polarization and mix the orthogonal polarization components. Fitting to recover the Stokes vectors describing polarization of the fundamental and second harmonic enables the recovery of Jones tensor elements through the Mueller tensor mathematical framework. Full tensor element images were obtained for χ_{zzz} and χ_{zxx}, enabling recovery of the tensor element ratio $\rho = \chi_{zzz} / \chi_{zxx}$. This ratio offers a measure of molecular-scale disorder within the collagen fiber, which can act as a quantitative probe to changes in extracellular structure associated with expression of pathologies such as lung, breast, and ovarian cancers.[6–8] Images of ρ for collagen embedded in thick tissue showed good agreement with previous measurements of mouse tail tendon in thin sections.

5.2 Theoretical Foundation

The Jones formalism describes the polarization state of an electric field in a basis set of the two orthogonal field components, most commonly horizontal and vertical or more generally transverse electric and transverse magnetic. Equation (6.1) below indicates the general form for a Jones vector and the application of a linear optical process by matrix multiplication, i.e., interaction with a generalized nondepolarizing optical element represented by the 2×2 Jones matrix *J*.

$$\vec{e}_{out} = J \cdot \vec{e}_{in} \tag{6.1}$$

In contrast, the Stokes vector describes polarization through a four element vector, in which each element is determined by the relative intensity of different polarization components. The first element contains the total integrated intensity, such that a normalized Stokes vector has a first element equal to 1. Equation (6.2) below defines the Stokes vector $\vec{s}$, and relates it to the Jones vector $\vec{e}$. Intensity information is obtained by the Kronecker product of the field components, in combination with the transfer matrix *A*, which maps those intensities in appropriate combination to the elements of $\vec{s}$. Note that the definition of $\vec{s}$ is such that unpolarized light is described by the Stokes vector $\vec{s} = \begin{bmatrix} 1 & 0 & 0 & 0 \end{bmatrix}^T$.

$$\vec{S} = \begin{pmatrix} I_H + I_V \\ I_H - I_V \\ I_{+45} - I_{-45} \\ I_R - I_L \end{pmatrix} = \begin{bmatrix} 1 & 0 & 0 & 1 \\ 1 & 0 & 0 & -1 \\ 0 & 1 & 1 & 0 \\ 0 & i & -i & 0 \end{bmatrix} \cdot \begin{pmatrix} \vec{e}_H^* \vec{e}_H \\ \vec{e}_H^* \vec{e}_V \\ \vec{e}_V^* \vec{e}_H \\ \vec{e}_V^* \vec{e}_V \end{pmatrix} = A \cdot \left(\vec{e}^* \otimes \vec{e} \right) \tag{6.2}$$

In much the same way that nondepolarizing optical components can be represented by Jones matrices in the Jones framework, the Stokes framework utilizes Mueller matrices *M* to indicate linear processes that can include partial or complete depolarization. The Mueller matrix for any generalized nondepolarizing optical element can again be constructed from the Jones matrix for that same optic in combination with the transfer matrix *A*.

$$\vec{S}_{out} = A \cdot \left(J^* \otimes J \right) \cdot A^{-1} \cdot \vec{S}_{in} = M \cdot \vec{S}_{in} \tag{6.3}$$

For quadratic nonlinear processes such as SHG or TPEF, the output polarization and amplitude are functions of two input fields, and not one. As a result, propagating polarization in the Jones frameowrk for these systems is most intuitively represented by the tensor product of the incident fields with the NLO susceptibility $\chi_J^{(2)}$. Once again, an analagous Mueller tensor, $M^{(2)}$, can be constructed utilizing the transfer matrix *A* and the corresponding Jones tensor.[19] The Jones tensor, $\chi_J^{(2)}$,is formally a 2x2x2 tensor in the laboratory reference frame, while $M^{(2)}$ is a 4x4x4. The mapping between Jones and Mueller tensors represented in Equation (6.4) below allows the generality of the Stokes-Mueller framework to be employed for compatibility with partially depolarized incident light, with simpler interpretation afforded by the Jones framework.

$$M^{(2)} = A \cdot \left(\chi_J^{(2)*} \otimes \chi_J^{(2)} \right) : A^{-1} A^{-1} \tag{6.4}$$

Equation 4 holds provided that the NLO process itself is intrinsically nondepolarizing, in which case the Mueller tensor $M^{(2)}$ allows prediction of the partially polarized state of the SHG produced by partially polarized incident light. The validity of this framework has been supported previously utilizing SHG measurements of z-cut quartz and thin collagen sections.[20] It was shown that for fully depolarized incident fields, resultant SHG followed intensity trends predicted by the Stokes-Mueller framework.

The theoretical treatment underpinning equations 1-4 assumes that the measurement of the second harmonic is in the same reference frame as the harmonophore. In practice, this is not necessarily the case. A reference frame rotation is often included to connect the incident field in the laboratory frame to the local frame, followed by subsequent rotation from the local frame back to the laboratory frame. This procedure is done in the Jones framework by multiplication of 2×2 Jones rotation matrices R_ϕ, and analogous 4×4 Mueller rotation matrices $\mathbf{R}_\phi$ may be produced following the procedure described in equation (6.3). Equation (6.5) below connects the observed laboratory frame (indicated by the subscript "L") Stokes vectors to the local frame (indicated by the subscript "*l*") Mueller tensor $M_l^{(2)}$, which can be connected to the underlying Jones tensor through equation (6.4). Measured Stokes vectors for the fundamental and second harmonic enable recovery of Jones tensor elements by fitting to equation (6.5).

$$\vec{S}^{2\omega} = M_L^{(2)} : \vec{S}^{\omega}\vec{S}^{\omega} = \mathbf{R}_{-\phi} M_l^{(2)} : \left(\mathbf{R}_\phi \vec{S}^{\omega}\right)\left(\mathbf{R}_\phi \vec{S}^{\omega}\right) \tag{6.5}$$

Note that while the mathematical framework formally incorporates all three Euler angles to describe the reference frame rotation from laboratory to local frames, for the specific case of collagen accounting for ψ is unnecessary due to cylindrical symmetry. Furthermore, due to the mouse tail sectioning approach utilized where tissue segments were taken parallel to the primary axis of tendon fibers, θ is assumed to be negligible.

5.3 Methods

Figure 5.1 illustrates the experimental apparatus. Polarization resolved SHG microscopy was conducted by modulating incident polarization with an electro-optic modulator (EOM) and analyzing the exiting polarization via combination of a quarter wave plate (QWP) and polarizer. For a given incident polarization state, the QWP was rotated from 0° to 45° in 22.5° increments, while the polarizer was rotated from 0° to 135° in 45° increments, yielding 12 total measurements. The recorded intensity vector for each pixel was linearly fit to recover the Stokes vector for both the transmitted IR as measured on the photodiode, as well as the SHG intensity on the PMT. The EOM operating at 8 MHz (synchronously clocked to the IR light source, a pulsed 80 MHz TiSapphire at 800 nm) yielded precisely 10 unique polarization states for the incident field, independently interrogated by synchronizing the EOM with the laser and the digital oscilloscope card as described previously.[21] The 10 separate polarizations allowed an overdetermined fit to recover local frame tensor elements of the sample at every signal carrying pixel within the field of view.

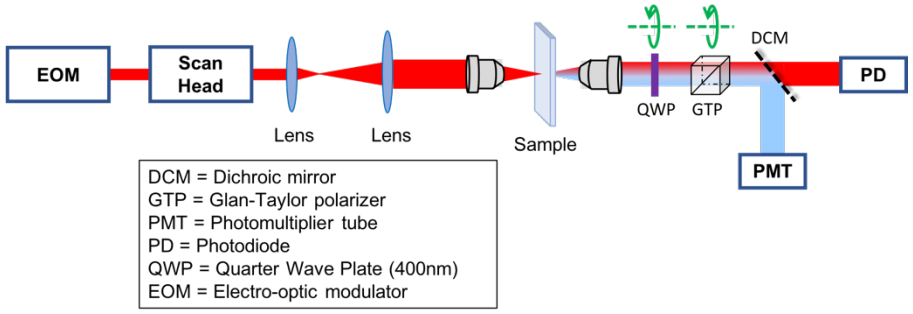

Figure 5.1. Instrument schematic. 800 nm light from an 80 MHz pulsed Ti Sapphire propagates through an EOM operating at 8 MHz, generating 10 unique polarization states. The scan head rasters the beam across the field of view, while a rotating QWP and polarizer serve as the analyzer for Stokes vector evaluation.

Mouse tail samples were obtained from the laboratory of Prof. Philip Low (Purdue University, West Lafayette, IN) and fixed in 10% neutral buffered formaline. The tail was subsequently decalcified in solution of Formical-4 (StatLab) for 5 hours, then placed in a 15% sucrose solution in PBS overnight, followed by a 30% sucrose solution in phosphate buffered saline overnight for cryoprotection. The use of sucrose for cryoprotection in preparing these tissue samples may have the secondary effect of acting as an index-matching medium, reducing the scattering measured within these samples relative to measurement of untreated tissue. Despite this, significant depolarization and birefringence was still observed, representing a lower bound for the degree of

turbidity expected in untreated tissue. The tails were then embedded in optimal cutting temperature compound (OCT) and frozen using isopentane chilled with liquid nitrogen. Tissue sections were taken from the central region of the tail, cut longitudinally using a Leica CM 1860 cryostat. Cryosectioning full thick tissue segments enabled measurement of collagen fibers in their natural environment relative to other structures in the tissue. When imaging, the beam was focused on the rear plane of the sample, such that SHG produced underwent minimal Rayleigh scattering prior to collection. This approach simplified polarization analysis as all depolarization was reasonably assumed to occur on the incident light only. Prior to polarization analysis, the resulting images were blurred with a Gaussian filter ($\sigma = 2$) for signal averaging with adjacent pixels.

For each pixel in the 12 collected images, a vector of intensities was used to conduct a linear fit to the Stokes vector using equation (6.6) below, where γ is the angle between the laboratory frame and the fast axis of the wave plate, and ϕ_{pol} is the angle of the fast axis of the polarizer relative to the laboratory frame. The fit matrix **F** was constructed from the known Mueller matrices for the detection QWP and polarizer. In principal, the Stokes vector can be constructed from direct measurement of I_H, I_V, I_{+45}, I_{-45}, I_R and I_L. In practice, a single wave plate was used for both the 400 nm and 800 nm light, thus the fundamental wavelength was not probed directly for I_R and I_L. Regardless, the right and left elliptical components were measured, which may be considered as a superposition of I_R and I_L with linearly polarized light, and enabled recovery of the Stokes vector by constructing the fit matrix with the appropriate quarter wave retarder Mueller matrix.

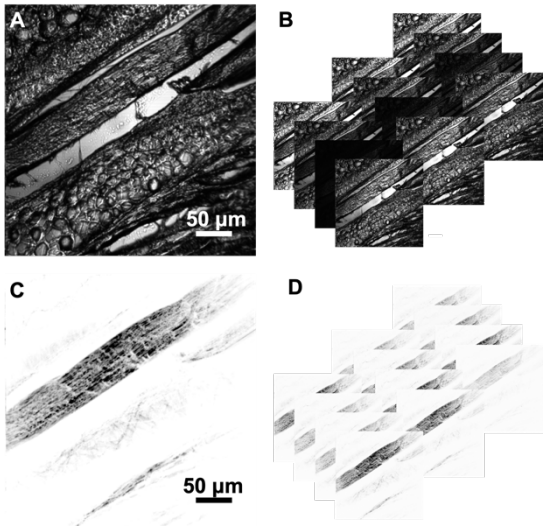

Figure 5.2 Images display total integrated intensity across all polarizations and analyzer configurations of laser transmittance (A) and SHG (C) for 40 m thick tissue. Stack of 12 images acquired with different analyzer configurations for polarization 1 for laser transmittance (B) and SHG (D).

$$
\begin{aligned}
I_{\text{det}} &= \begin{bmatrix} 1 & 0 & 0 & 0 \end{bmatrix} \cdot M_{pol} \cdot R(\phi_{pol}) \cdot R(-\gamma) \cdot M_{WP} \cdot R(\gamma) \cdot \vec{S}_{out} \\
&= F_{\gamma,\phi_{pol}} \cdot \vec{S}_{out}
\end{aligned} \tag{6.6}
$$

For each of the ten incident polarization states, 12 images were acquired as illustrated in **Figure 5.2**, corresponding to 4 unique polarizer angles and 3 unique quarter wave plate angles for the detection optics. For a single pixel, stacking each intensity from the unique analyzer configurations into a single vector expanded the dimensionality of the linear transform F in equation **Error! Reference source not found.** above from a 1×4 to a 12×4 matrix, **F** in equation (6.7) below.

$$\begin{aligned} I_{\text{det}} &= \mathbf{F}\vec{S}_{out}; \\ \vec{S}_{out} &= \left(\mathbf{F}^T\mathbf{F}\right)\mathbf{F}^T I_{\text{det}} \end{aligned} \tag{6.7}$$

Figure 5.2, above, shows the total integrated intensity of detected laser transmittance (A) and SHG (C) and the 12 unique images for polarization 1 (B, D) for 40 μm thick tissue. For both SHG and laser transmittance, a per-pixel linear fit was conducted to equation 7, reducing the set of 120 input images to 40 images corresponding to the Stokes vector elements for each of the 10 polarization states. This process was performed for both the transmitted infrared beam and the frequency doubled SHG light.

5.4 Results & Discussion

Figure 5.3 (right) shows the total integrated laser transmittance intensity for each of the three tissue thicknesses measured and demonstrates broadening of the distribution of degree of polarization (DoP) for pixels used in the polarization analysis. DoP is defined as $\text{DoP} = \sqrt{s_1^2 + s_2^2 + s_3^2}/s_0$. Tissue samples contain many refractive index changes associated with membranes surrounding structures like cells, nuclei, and organelles. Consequently, as light propagates through inhomogeneous tissue, the phase delay introduced to different cross sectional areas of the beam can vary. These spatially varying shifts result in partial depolarization of the

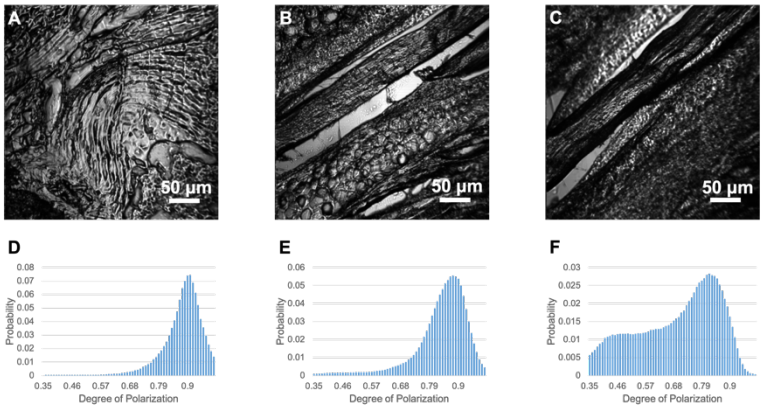

Figure 5.3 Laser transmittance images integrated across all polarizations and analyzer configurations for 5 (A), 40 (B), and 70 μm (C) thick tissue samples are displayed. Histograms of the degree of polarization for pixels used in polarization analysis are plotted, showing increased depolarization as a function of tissue thickness (D-F).

incident light upon combination in the focal plane. As the total number of refractive index changes scales with the thickness of tissue, it is expected that increasing thickness will result in increased depolarization induced by interaction with the sample. A DoP near 1 indicates a purely polarized field, while a DoP of zero corresponds to the limit of complete depolarization, (i.e., the only nonzero Stokes element is s_0). The mean DoP value for pixels used in polarization analysis in the measured samples shifted from 0.88 for 5 μm tissue, to 0.83 for 40 μm and 0.69 for 70 μm thickness. More striking, however, is the increased width in the distribution of recovered DoP values. Depolarization, as demonstrated here for the transmitted infrared beam, is not compatible the Jones calculus and the more general Stokes framework enables more accurate polarization analysis.

While scattering and depolarization are a significant challenge in polarization analysis, they do not represent the only perturbation of polarization induced by the sample itself. Birefringence can also significantly alter the polarization of the fundamental, further complicating analysis. **Figure 5.4** shows the change in polarization state ΔS as a function of position, measured by taking the difference between the incident Stokes vector in regions without tissue with every pixel in the field of view. ΔS_1, shown in **Figure 5.4A-C**, highlights regions of linear rotation within the field of view while **Figure 5.4D-F** map ΔS_3, corresponding to changes in ellipticity. In both

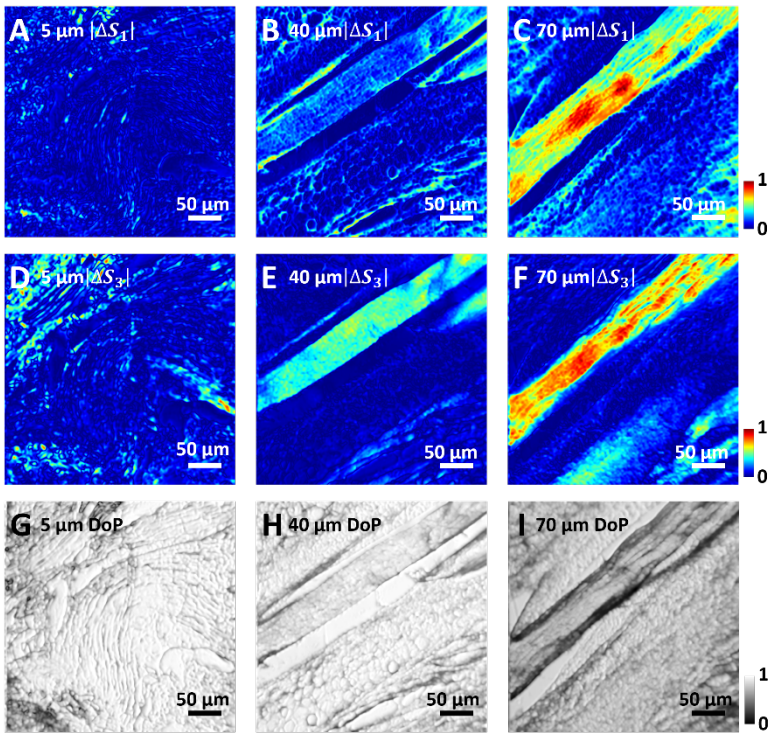

Figure 5.4 Images of the ΔS_1 (A-C) and ΔS_3 (D-F) vector elements for the three tissue thicknesses, polarization state 1 show significant birefringence effects as a function of tissue thickness. The contrast is set from 0 to 1 in terms of absolute deviation, with blue representing 0 deviation from the reference blank and red a deviation of 1; the theoretical maximum deviation is 2. Maps of the DoP for the same polarization (G-I) show regions of high scattering occur preferentially near structural edges.

the 40 μm and 70 μm tissue samples fibers diagonally aligned show significant birefringence relative to the rest of the field of view, particularly on regions near the edge of the tendon fibers. Scattering was also largest in these locations, as they represent regions within the field of view with significant heterogeneity in the refractive index. Both scattering and birefringence substantially increase as a function of tissue thickness.

This significant depolarization from propagation through the sectioned tissues prevents the direct use of Jones tensor analyses to recover tensor elements related to local structure, as the Jones architecture is only formally valid for purely polarized incident light. In the presence of depolarization, polarization states are more appropriately described by Stokes vectors. Measurement of the Stokes vectors of the fundamental and second harmonic fields is afforded by fitting to Eq. (6.7) while the mathematical relations given in Eq. (6.4) allow the more general Mueller tensor description of collagen to be fully described in terms of the simpler Jones tensor elements. Through this relation, incoming and exiting Stokes vectors describing partially polarized light can still be interpreted directly in terms of both the laboratory-frame Jones and local-frame Cartesian tensors normally reserved for purely polarized analyses, discussed here in the context of the tensor element ratio ρ.

Nonlinear optical susceptibility tensor elements of collagen were imaged utilizing Stokes vectors obtained via linear fitting for both laser transmittance and bright field images. For collagen, the only unique nonzero local frame tensor elements by symmetry are χ_{zzz}, χ_{zxx}, χ_{xxz}, and χ_{yzx}, defined in a reference frame with the C_∞ fiber axis of collagen paralleling z. The chiral element χ_{yzx} is relatively small in magnitude and does not contribute to the detected intensity for collagen fibers aligned in the image plane within the paraxial approximation.[22] Quantum chemical calculations show the tropocollagen molecular hyperpolarizability is dominated by the β_{zzz} element.[23,24] Interchangeability of indices within the dominant β_{zzz} element at the molecular level translates to interchangeability at the ensemble level, such that projections of β_{zzz} onto the macromolecular elements χ_{zxx} and χ_{xxz} are identical. Experimentally, the approximate equality is often observed.[25] Using the assumption of equality for these two elements, the number of unknowns for the sample

drops to 3: orientation, χ_{zxx}, and χ_{xxz}. Using the image analysis plugin OrientationJ for NIH ImageJ, local orientation of fibers can be extracted from the SHG images.[26,27] A nonlinear optimization to the tensor elements χ_{zzz} and χ_{zxx} was conducted using the Levenberg-Marquardt algorithm.[28,29] The tensor element ratio ρ was then recovered, which has been used to analyze the local distribution of tilt angle of collagen fibrils about the fiber axis.[30,31]

It is interesting to compare the present results with previous measurements of SHG of collagen tissue obtained with fully depolarized incident light, prepared using a microretarder array depolarizer.[20] In that work, the NLO response was used to directly fit azimuthal and polar orientation of collagen, yielding good agreement between image analysis approaches and direct fitting to the azimuthal orientation angle of collagen. Given the established agreement between single-pixel polarization analysis and image texture analysis for quantifying collagen azimuthal orientation, a greater emphasis was placed here on recovery of nonlinear optical parameters inaccessible from knowledge of azimuthal angle alone, which can be obtained by image analysis. Utilizing OrientationJ for azimuthal angle determination enabled increased statistical confidence in the nonlinear optical parameters recovered by fitting of the polarization-dependent SHG produced by partially polarized incident light.

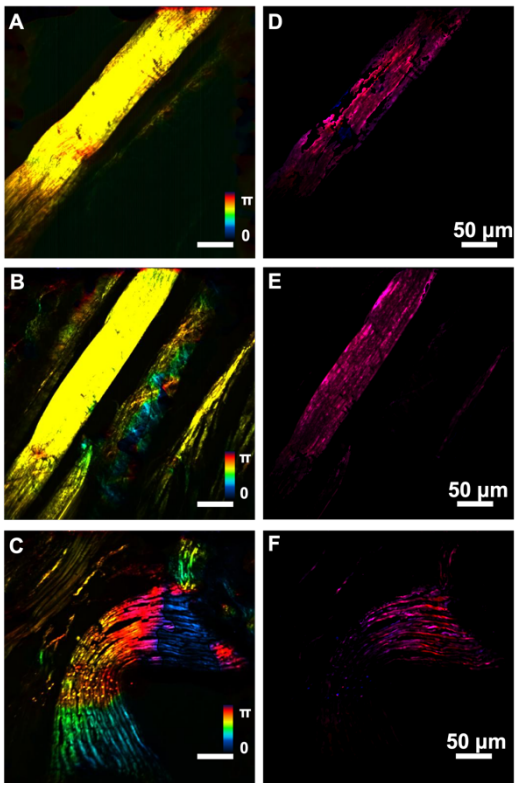

Figure 5.5 Orientation maps (A-C) and red-blue colormaps of χ_{zzz} and χ_{zxx} (D-F), for 70 µm, 40 µm, and 5 µm thick tissues obtained from the analysis are shown.

Figure 5.5 shows orientation maps and colormaps of the χ_{zzz} and χ_{zxx} tensor elements for tissues of 5, 40, and 70 µm thickness. Quantitative analysis of NLO susceptibility tensor elements was conducted for pixels containing less than 20% relative error in both coefficients, as determined by the Jacobian approximation to the Hessian in combination with the standard error of the fit. Pixels

with negative ρ values were assumed to be nonphysical and excluded from this analysis; simulations suggest that Poisson noise in the shot-noise limited photomultiplier tube detector is sufficient to produce distributions in ρ with significant negative valued elements. Mean tensor ratios of 1.8, 1.8, and 2.3 were observed for the three tissue thicknesses. It is posited that the larger ρ value observed for the 70 µm tissue is due to the lower signal-to-noise ratio for that experiment. Indeed, **Figure 5.5D** shows large regions of SHG activity that produce fitted tensor values with high relative error and were thus excluded from analysis of the ρ distribution.

Most intriguing about the method of analysis utilized here is the ability to analyze the change in polarization induced by the process of SHG. As SHG is often mathematically treated as arising from only the purely polarized component of incident light, the consequences of the SHG process on the overall degree of polarization of the exiting field is often neglected. Examination of the distributions of DoP for both the second harmonic and the infrared light indicates that the SHG was more polarized for 40 and 70 um thick tissues than the corresponding pixels in the laser transmittance image, with ratios averaging 1.03 and 1.10 respectively. In contrast, the Stokes vectors of SHG in the thinnest tissue segment showed the greatest induced depolarization with a ratio of 0.82.

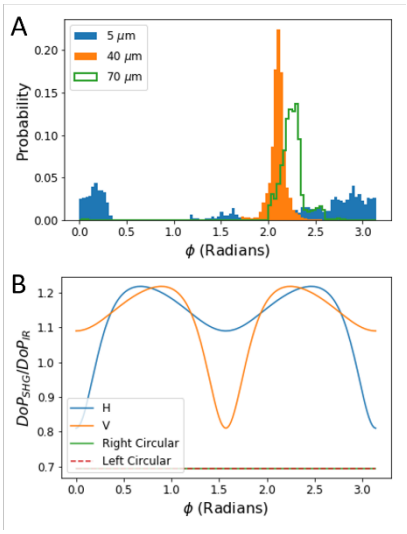

Figure 5.6 The distributions of orientation for 5, 40, and 70 µm thick tissue (A) are plotted. The simulated ratio of DoP_{SHG}/DoP_{IR}, as a function of collagen rotation in plane (B) shows the SHG process to be either hyperpolarizing or depolarizing depending on orientation for linearly polarized light, and always to be depolarizing for circularly polarized light at $DoP_{IR} = 0.8$.

The observation of hyperpolarization from SHG measurements of collagen with partially depolarized incident light is consistent with previous studies of SHG produced from the limit of complete depolarization of the fundamental beam. It has previously been shown that depolarized light incident to thin sections of collagenous tissue results in emission of partially polarized light, in excellent agreement with predictions from the Mueller tensor framework. The depolarized field is projected onto the finite set of nonzero tensor elements of the NLO susceptibility, which only allows a few select polarization states of SHG. Consequently, the Stokes vector for SHG emitted by collagen

from a depolarized field always has a DoP_{SHG}/DoP_{IR} greater than one. This effect is qualitatively similar to fluorescence excitation with unpolarized light resulting in emitted light partially polarized parallel with the transition moment. This intrinsic hyperpolarization propensity in part may explain the increase in DoP_{SHG}/DoP_{IR} as tissue thickness increases, due to a larger relative contribution of depolarized incident light to stimulate SHG. If the histograms within **Figure 5.3** (E-F) are examined, the greatest mean in incident degree of polarization is observed for the thinnest tissue section. Similarly, **Figure 5.4** (G-I) show the greatest degree of polarization as a function of position, interpretable via the brightness in the images, for the thinnest tissue. For a fixed degree of depolarization inherent in the process of SHG from finite-sized objects, the relative polarization purity DoP_{SHG}/DoP_{IR} is smaller for the thin section, as the denominator is higher. Consequently, as the DoP_{IR} approaches zero, the hyperpolarization asymptotically approaching infinity.

In practice, this limiting case of complete depolarization of the incident beam is tempered by the presence of contributions from the purely polarized component of light as well, the interplay of which is dependent on the orientation of collagen. In the limit of no depolarization, the ratio of DoP_{SHG}/DoP_{IR} will simply be unity. The anticipated trends for partially polarized incident light relative to these two limits are not immediately obvious. Simulations of the DoP_{SHG}/DoP_{IR} as a function of orientation angle of collagen were performed to provide additional insights into the origin of the hyperpolarizing and depolarizing effects of SHG. Values of $\rho = 1.8$ and $\theta = 0$ were assumed. **Figure 5.6** shows a plot of DoP_{SHG}/DoP_{IR}, with a DoP_{IR} of 0.8, for H and V polarized light, right circularly polarized light, and left circularly polarized light. Light unperturbed by the sample can be interpreted in terms of these four components since measurements conducted modulated retardance of light incident to the tissue sample from a starting polarization of pure H light. For linearly polarized light the process of SHG under these conditions produces a Stokes vector that is either more or less purely polarized than the incident IR, as a function of collagen orientation. Circularly polarized incident light always produces a relatively depolarized SHG field under the simulation conditions.

Physically, the maxima observed in **Figure 5.6B** can be explained by a competing relative contribution of partially polarized and fully polarized incident light to the total SHG intensity produced by the collagen fiber. Consider the total SHG produced as a linear combination of SHG

occurring from depolarized and purely polarized incident light. Within this model, as the collagen fiber is rotated off of the axis of polarization of the incident field, the polarization of the SHG emitted from the purely polarized component is rotated. This has a secondary effect of modulating the intensity of the SHG emitted from the purely polarized component, due to the difference in tensor element magnitudes. Similarly, SHG from the depolarized fundamental beam component results in a partially polarized Stokes vector emitted by the collagen. This partially polarized Stokes vector rotates as a function of collagen orientation with respect to the laboratory frame, but at a constant intensity. The net effect is that the relative contribution of purely polarized light to SHG and relative contribution of depolarized light to the SHG are both changing, and there is a single collagen orientation for a given $DoP_{IR,}$ which then maximally polarizes the output SHG.

These same collective arguments provide a potential explanation for the observation of a $DoP_{SHG}/DoP_{IR} < 1$ for the thinnest tissue section. Even through just 5 μm of tissue, the measured DoP_{IR} had a mean of 0.88, corresponding to small but non-negligible depolarization of the incident beam. The orientation distribution of collagen within the 5 μm thick tissue section suggests the origin of net depolarization via SHG when contrasted with the H-polarized intensity trace observed in **Figure 5.6B**. In **Figure 5.6A**, note the large population of orientations for the thin section near $\phi = 0$ and π, where SHG is maximally depolarizing for H-polarized incident light. In contrast, the same incident polarization becomes hyperpolarizing for collagen orientations near $\pi/4$ and $3\pi/4$ azimuthal angles, consistent with maxima in the orientation distributions of collagen in the 40 and 70 μm thick sections. This simplified model provides a qualitative explanation for the observed differences in depolarization and hyperpolarization for the different samples investigated.

5.5 Conclusion

A method was demonstrated for the experimental recovery of local frame tensor elements determining the NLO activity of collagen embedded in turbid tissue. The method relies on the independent measurement of the Stokes vectors for the fundamental frequency and second harmonic beams, followed by fitting to recover the underlying Jones tensor elements. The distribution of the tensor element ratio ρ for collagen fibers in mouse tail tissue was measured, with mean tensor values of 1.8, 1.8, and 2.3 for 5, 40, and 70 μm samples, respectively, consistent

with previous measurements of mouse tail sectioned thinly as well as previously reported values in the literature.[20,24,25] Recovery of consistent tensor element values for varying tissue thicknesses demonstrates utility of the Stokes-Mueller framework to account for changes in polarization from both birefringent and scattering effects on the fundamental frequency. The framework utilized leverages the simplicity of the Jones description for interpreting polarization dependent NLO with the general applicability of the Stokes description of polarization. Furthermore, this framework enables modification of existing architectures for analysis of NLO polarization to account for loss of polarization purity in the fundamental fields. Hyperpolarizing and depolarizing effects of SHG were observed, and their physical origin was ascribed to an interplay of the relative intensity contribution of polarized and depolarized light incident to the sample. The process of SHG is not often discussed in reference to its capacity to hyperpolarize or depolarize a field, and the observations reported herein are consequently of particular note.

5.6 Acknowledgements

The authors graciously acknowledge financial support from the National Science Foundation grant numbers 1710475 and 1763896 and National Institutes of Health grant 5R01GM103401 through the National Institute of General Medical Sciences.

5.7 References

1. Ulcickas, J. R. W.; Simpson, G. J. Mueller Tensor Nonlinear Optical Polarization Analysis in Turbid Media. *J. Phys. Chem. B* **2019**, *123* (30), 6643–6650. https://doi.org/10.1021/acs.jpcb.9b04961.

2. Drobizhev, M.; Makarov, N.; Tillo, S.; Nature …, H.-T. Two-Photon Absorption Properties of Fluorescent Proteins. *Nat. …* **2011**.

3. Yang, W.; Yuste, R. In Vivo Imaging of Neural Activity. *Nat. Methods* **2017**. https://doi.org/10.1038/nmeth.4230.

4. Li, D.; Zheng, W.; Zeng, Y.; Luo, Y.; letters, Q.-J. Two-Photon Excited Hemoglobin Fluorescence Provides Contrast Mechanism for Label-Free Imaging of Microvasculature in Vivo. *Opt. Lett.* **2011**.

5. Balu, M.; Mazhar, A.; Hayakawa, C.; journal, M.-R. In Vivo Multiphoton NADH Fluorescence Reveals Depth-Dependent Keratinocyte Metabolism in Human Skin. *Biophys. J.* **2013**.

6. Tilbury, K.; Lien, C.-H. H.; Chen, S.-J. J.; Campagnola, P. J. Differentiation of Col I and Col III Isoforms in Stromal Models of Ovarian Cancer by Analysis of Second Harmonic Generation Polarization and Emission Directionality. *Biophys J* **2014**, *106* (2), 354–365. https://doi.org/10.1016/j.bpj.2013.10.044.

7. Golaraei, A.; Cisek, R.; Krouglov, S.; Navab, R.; Niu, C.; Sakashita, S.; Yasufuku, K.; Tsao, M.-S.; Wilson, B. C.; Barzda, V. Characterization of Collagen in Non-Small Cell Lung Carcinoma with Second Harmonic Polarization Microscopy. *Biomed Opt Express* **2014**, *5* (10), 3562. https://doi.org/10.1364/BOE.5.003562.

8. Levental, K.; Yu, H.; Kass, L.; Lakins, J.; Egeblad, M. Matrix Crosslinking Forces Tumor Progression by Enhancing Integrin Signaling. *Cell* **2009**.

9. Kerian, Emma L. Polarization-Dependent Nonlinear Optical Microscopy Methods for the Analysis of Crystals and Biological Tissues, Purdue University, 2015.

10. Roth, S.; Freund, I. Second Harmonic Generation in Collagen. *J. Chem. Phys.* **1979**, *70* (4), 1637–1643. https://doi.org/10.1063/1.437677.

11. Plotnikov, S. V.; Millard, A. C.; Campagnola, P. J.; Mohler, W. A. Characterization of the Myosin-Based Source for Second-Harmonic Generation from Muscle Sarcomeres. *Biophys. J.* **2006**, *90* (2), 693–703. https://doi.org/10.1529/biophysj.105.071555.

12. Nadiarnykh, O.; Plotnikov, S.; Mohler, W. A.; Kalajzic, I.; Deborah, R.-B.; Campagnola, P. J. Second Harmonic Generation Imaging Microscopy Studies of Osteogenesis Imperfecta. *J Biomed Opt* **2007**, *12* (5), 051805. https://doi.org/10.1117/1.2799538.

13. Gusachenko, I.; Latour, G.; MC, S.-K. Polarization-Resolved Second Harmonic Microscopy in Anisotropic Thick Tissues. *Opt. Express* **2010**.

14. de Aguiar, H.; Gigan, S.; Brasselet, S. Polarization Recovery through Scattering Media. *Sci. Adv.* **2017**.

15. Shi, Y.; WM, M.; physics letters, H.-R. An Extension of the Mueller Scattering Matrix to Nonlinear Light Scattering. *Chem. Phys. Lett.* **1993**.

16. Shi, Y.; WM, M.; A, H.-R. Generalized Stokes-Mueller Formalism for Two-Photon Absorption, Frequency Doubling, and Hyper-Raman Scattering. *Phys. Rev. A* **1994**. https://doi.org/10.1103/PhysRevA.49.1999.

17. Samim, M.; Krouglov, S.; B, B.-V. Double Stokes Mueller Polarimetry of Second-Harmonic Generation in Ordered Molecular Structures. *JOSA B* **2015**.

18. Burke, M.; Golaraei, A.; Atkins, A.; structural biology, A.-M. Collagen Fibril Organization within Rat Vertebral Bone Modified with Metastatic Involvement. *... Struct. Biol.* **2017**.

19. Simpson, G. Connection of Jones and Mueller Tensors in Second Harmonic Generation and Multi-Photon Fluorescence Measurements. *J Phys Chem B* **2016**, *120* (13), 3281–3302. https://doi.org/10.1021/acs.jpcb.5b11841.

20. Ding, C.; Ulcickas, J.; Deng, F.; review letters, S. G. Second Harmonic Generation of Unpolarized Light. *Phys. Rev. Lett.* **2017**.

21. DeWalt, E. L.; Sullivan, S. Z.; Schmitt, P. D.; Muir, R. D.; Simpson, G. J. Polarization Modulated Second Harmonic Generation Ellipsometric Microscopy at Video Rate. *Anal. Chem.* **2014**, *86* (16), 8448–8456. https://doi.org/10.1021/ac502124v.

22. Dow, X. Y.; DeWalt, E. L.; Sullivan, S. Z.; Schmitt, P. D.; Ulcickas, J. R. W.; Simpson, G. J. Imaging the Nonlinear Susceptibility Tensor of Collagen by Nonlinear Optical Stokes Ellipsometry. *Biophys. J.* **2016**, *111* (7), 1361–1374. https://doi.org/10.1016/j.bpj.2016.05.055.

23. de Wergifosse, M.; de Ruyck, J.; Champagne, B. How the Second-Order Nonlinear Optical Response of the Collagen Triple Helix Appears: A Theoretical Investigation. *J. Phys. Chem. C* **2014**, *118* (16), 8595–8602. https://doi.org/10.1021/jp501602a.

24. Dow, X. Y.; L, D., Emma; Sullivan, S. Z.; Schmitt, P. D.; Ulcickas, J.; Simpson, G. J. Imaging the Nonlinear Susceptibility Tensor of Collagen by Nonlinear Optical Stokes Ellipsometry *Biophys J* **2016**, *111* (7), 1361–1374. https://doi.org/10.1016/j.bpj.2016.05.055.

25. Romijn, E.; Finnøy, A.; of biophotonics, L.-M. Analyzing the Feasibility of Discriminating between Collagen Type I and II Using Polarization Resolved Second Harmonic Generation. *J. Biophotonics* **2018**. https://doi.org/10.1002/jbio.201800090.

26. Schneider, C.; Rasband, W.; methods, E.-K. NIH Image to ImageJ: 25 Years of Image Analysis. *Nat. Methods* **2012**.

27. Rezakhaniha, R.; Agianniotis, A.; modeling in … J. Experimental Investigation of Collagen Waviness and Orientation in the Arterial Adventitia Using Confocal Laser Scanning Microscopy. *... Model. ...* **2012**. https://doi.org/10.1007/s10237-011-0325-z.

28. L.-K. A Method for the Solution of Certain Non-Linear Problems in Least Squares. *Q. Appl. Math.* **1944**.

29. M.-D. An Algorithm for Least-Squares Estimation of Nonlinear Parameters. *J. Soc. Ind. Appl. ...* **1963**.

30. Su, P.-J.; Chen, W.-L.; Hong, J.-B.; Li, T.-H.; Wu, R.-J.; Chou, C.-K.; Chen, S.-J.; Hu, C.; Lin, S.-J.; Dong, C.-Y. Discrimination of Collagen in Normal and Pathological Skin Dermis through Second-Order Susceptibility Microscopy. *Opt. Express* **2009**, *17* (13), 11161–11171. https://doi.org/10.1364/OE.17.011161.

31. Chen, W.; Li, T.; Su, P.; Chou, C.; Physics …, F.-P. Second Harmonic Generation Tensor Microscopy for Tissue Imaging. *Appl. Phys. ...* **2009**.

CHAPTER 6. THEORETICAL FOUNDATION FOR ELECTRIC DIPOLE ALLOWED CHIRAL-SPECIFIC FLUORESCENCE OPTICAL ROTARY DISPERSION (F-ORD) FROM INTERFACIAL ASSEMBLIES

The contents of this chapter are adapted from the publication Theoretical Foundation For Electric Dipole Allowed Chiral-Specific Fluorescence Optical Rotary Dispersion (F-ORD) From Interfacial Assemblies, originally published in *The Journal of Physical Chemistry Letters* in 2016.[1]

6.1 Introduction

Absolute chirality plays a critical role in biological interactions, governing enzyme-substrate interactions.[3-5] To design a functioning pharmaceutical therapeutic agent, target chirality is typically a prerequisite. However, few probes are available to definitively characterize chirality. Vibrational CD (VCD) and Raman optical activity (ROA) are selective techniques commonly utilized for chiral sensing but are limited by low sensitivity.[6-7] Electronic CD (ECD) offers higher sensitivity, but the broad band nature of electronic transitions reduces specificity.[8] Fully electric dipole allowed chiral-specific effects including circular extinction are reasonably well-established in measurements of crystalline materials. In studies of achiral dyes incorporated during crystal growth, Kahr and coworkers have nicely demonstrated the observation of chiral-specificity for achiral dyes incorporated into chiral lattices.[9] In this instance, the circular dichroism observed arose from an interplay between birefringence in the crystal and linear dichroism from preferred crystal orientation and is thus limited to dye-doped crystalline and polycrystalline materials[10]. Alternative methods employing second order nonlinear optical (NLO) spectroscopy have been shown to be highly sensitive to chirality, also through an electric dipole–allowed mechanism.[11-13] Near 100% dichroic ratios have been observed for oriented binapthol monolayer films using second harmonic generation (SHG) CD.[14] In addition, Fourier transform microwave spectroscopy has been employed for electric dipole allowed enantiomer-specific detection methods via triply resonant microwave nonlinear wave mixing.[15-16] However, the accessibility of NLO approaches is reduced by the requirement of a pulsed laser source at optical frequencies and the complexity of the experiments in general. One-photon fluorescence (1PF), in contrast, has a much higher quantum efficiency, does not require a coherent light source, and can be easily implemented into

existing fluorescence microscopes. Here, we propose a new spectroscopic method based on 1PF that is selective to chirality at interfaces.

6.2 Electric-dipole allowed chiral specific fluorescence

A simple physical model explaining the prediction of electric dipole allowed chiral-specific fluorescence in uniaxial assemblies is shown in **Figure 6.1** in the limiting case of orthogonally polarized absorption (red arrow) and fluorescence (blue arrow) transition moments. A non-zero net rotation in the primary axis of polarization can be observed between the projections of $\vec{\mu}^a$ and $\vec{\mu}^f$ on the *X*-*Y* plane. Excitation with linearly polarized light will result in fluorescence that, on average, yields a maximum in the polarized emission intensity that is rotated relative to the excitation axis. This rotation is the origin of the chiral-specific signal. From inspection of the graphic, the F-ORD process is non-reciprocal such that flipping the surface through a 180° rotation about the *X*-axis will result in the opposite sense of rotation.

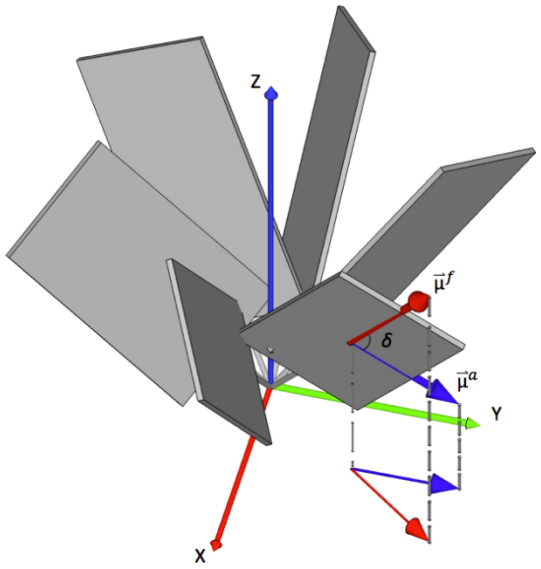

Figure 6.1 A graphic illustration of planar fluorophores (represented by gray plates) with uniaxial symmetry in the laboratory X-Y-Z frame. The Euler angle φ is uniformly sampled for the assembly. Detected signal is defined in the projection onto the laboratory laboratory X-Y-Z frame. The Euler angle φ is uniformly sampled for the assembly. Detected signal is defined in the projection onto the laboratory X-Y plane. Y-polarized excitation results in fluorescence detected at an angle rotated clockwise, as shown in the projection.

The mathematical framework for chiral-specific fluorescence builds most directly on the electric dipole-allowed orientational mechanism underpinning chiral-specific four-wave mixing described by Davis et al.[17] In this mechanism, a chiral-specific nonlinear optical field can be produced even in the absence of intrinsic chirality within the chromophore through chiral orientational arrangement in an ensemble. The macroscopic chirality arises purely through packing effects and does not require any coupling between chromophores or chiral distortion. Furthermore, because both the chiral and achiral responses are fully electric dipole allowed, they are often comparable

in magnitude with dichroic ratios approaching unity under favorable conditions. A qualitatively similar mechanism is well-established for describing the high sensitivity of chirality in surface second harmonic and sum frequency generation.

6.3 Mechanism of F-ORD

The connection between the experimental observables and the molecular properties can be constructed by starting with fundamental light matter interactions at the molecular level. The process of absorption can be described either by a transition dipole moment μ^i, or more formally by the imaginary component of the polarizability matrix α^{ij}, where i, j represent the polarization of the emission and excitation light respectively. The two formalisms are connected by the following equation describing the excitation from state I to state n. The damping term Γ describes the half width at half max of the lineshape function.

$$\alpha^{ij}(-\omega;\omega) = \frac{1}{\hbar}\sum_n \frac{\mu_{In}^i \mu_{nI}^j}{\omega_n - \omega - i\Gamma_n} + \frac{\mu_{In}^j \mu_{nI}^i}{\omega_n + \omega + i\Gamma_n} \tag{6.1}$$

For a molecule initially in the ground state such that I = 0, the first term in the summation will dominate, since the excited state lies at an energy higher than the initial state. In the case of fluorescence emission, the second term dominates, as the initial state is higher in energy than the state contributing to the resonance enhancement.[18] Only the imaginary contributions to the polarizability impact the overall attenuation or amplification of the optical field, corresponding to absorption or emission, respectively. The polarization-dependence of absorption and emission are dictated by the terms in the numerator. In a molecular coordinate system in which the z'-axis parallels the fluorescence emission transition moment and the absorption transition moment lies in the x'-z' plane, the fluorescence transition moment only has one nonzero term $\mu_{z'}^f = |\vec{\mu}^f|$ and the absorption transition moment has two components: $\left(\mu_{nI}^{x'}\right)^a = |(\vec{\mu}_{nI})^a| \sin\delta$ and $\left(\mu_{nI}^{z'}\right)^a = |(\vec{\mu}_{nI})^a| \cos\delta$ where δ defines the angle between the fluorescence and absorption transition moments consistent with **Figure 6.1**.

Using the relation $\vec{\mu}_{nm} = \vec{\mu}_{mn}^*$, the expression for the linear polarizability describing absorption in Equation (6.1) can be rewritten as follows for a molecule initially in the ground state I = 0.

$$\alpha^{x'x'} \cong S(\omega)\left|\vec{\mu}_{n0}\right|^2 \sin^2\delta$$
$$\alpha^{z'z'} \cong S(\omega)\left|\vec{\mu}_{n0}\right|^2 \cos^2\delta \tag{6.2}$$
$$\alpha^{x'z'} = \alpha^{z'x'} \cong S(\omega)\left|\vec{\mu}_{n0}\right|^2 \sin\delta\cos\delta$$

Where the S(ω) describes the resonance line-shape function. If it is assumed that molecular rotation is slow relative to the fluorescence lifetime, the orientational averages connecting the molecular frame to the laboratory frame are performed over the combined coordinates describing absorption and emission.

In a general sense, the intensity of pure linearly polarized fluorescence as a function of the polarization rotation angle γ for linearly polarized excitation light depends on the following three trigonometric polynomial coefficients *A* - *C*.

$$I_n(\gamma) = A_n\cos^2\gamma + B_n\sin\gamma\cos\gamma + C_n\sin^2\gamma \tag{6.3}$$

In the above equation, n may refer to the Stokes frame horizontal polarization (H) or vertical polarization (V). These three coefficients are in turn related back to the molecular orientation distribution and the transition moments within the molecular frame. Furthermore, if the angle between the absorption and emission angles is defined to be δ described above, the expressions for the polynomial coefficients can be rewritten in terms of δ as shown below for H polarized detection.

$$A_H = K\left(\left|\bar{\mu}^f\right|^2\left|\bar{\mu}^a\right|^2\right)\begin{Bmatrix}\cos^2\delta\left\langle\left(R_{Xz'}R_{Xz'}\right)^f\left(R_{Xz'}R_{Xz'}\right)^a\right\rangle\\ +2\sin\delta\cos\delta\left\langle\left(R_{Xz'}R_{Xz'}\right)^f\left(R_{Xx'}R_{Xz'}\right)^a\right\rangle\\ +\sin^2\delta\left\langle\left(R_{Xz'}R_{Xz'}\right)^f\left(R_{Xx'}R_{Xx'}\right)^a\right\rangle\end{Bmatrix} \tag{6.4}$$

$$B_H = K\left(\left|\bar{\mu}^f\right|^2\left|\bar{\mu}^a\right|^2\right)\begin{Bmatrix}\cos^2\delta\left\langle\left(R_{Xz'}R_{Xz'}\right)^f\left(R_{Xz'}R_{Yz'}\right)^a\right\rangle\\ +2\sin\delta\cos\delta\left\langle\left(R_{Xz'}R_{Xz'}\right)^f\left(R_{Xx'}R_{Yz'}\right)^a\right\rangle\\ +\sin^2\delta\left\langle\left(R_{Xz'}R_{Xz'}\right)^f\left(R_{Xx'}R_{Yx'}\right)^a\right\rangle\end{Bmatrix} \tag{6.5}$$

$$C_H = K\left(\left|\vec{\mu}^f\right|^2\left|\vec{\mu}^a\right|^2\right)\begin{Bmatrix}\cos^2\delta\left\langle\left(R_{Xz'}R_{Xz'}\right)^f\left(R_{Yz'}R_{Yz'}\right)^a\right\rangle\\+2\sin\delta\cos\delta\left\langle\left(R_{Xz'}R_{Xz'}\right)^f\left(R_{Yx'}R_{Yz'}\right)^a\right\rangle\\+\sin^2\delta\left\langle\left(R_{Xz'}R_{Xz'}\right)^f\left(R_{Yx'}R_{Yx'}\right)^a\right\rangle\end{Bmatrix} \tag{6.6}$$

Expressions for each of the nine orientational averages in Equations (6.4)-(6.6) for a uniform distribution in φ have been explicitly evaluated previously.[17] The orientational averages for the contribution in B_H are given by the following expressions.

$$\left\langle\left(R_{Xz'}R_{Xz'}\right)^f\left(R_{Xz'}R_{Yz'}\right)^a\right\rangle = 0 \tag{6.7}$$

$$\left\langle\left(R_{Xz'}R_{Xz'}\right)^f\left(R_{Xx'}R_{Yz'}\right)^a\right\rangle = -\tfrac{1}{8}\left\langle\sin^3\theta\sin\psi\right\rangle \tag{6.8}$$

$$\left\langle\left(R_{Xz'}R_{Xz'}\right)^f\left(R_{Xx'}R_{Yx'}\right)^a\right\rangle = \tfrac{1}{4}\left\langle\sin^2\theta\cos\theta\sin\psi\cos\psi\right\rangle \tag{6.9}$$

In the presence of a mirror plane containing the unique axis, the B term goes to zero due to the corresponding even symmetry in the distributions in ψ. Thus, only ensembles exhibiting chiral order will display this response and the B coefficient contribution to detected signal is hereby referred to as the chiral-specific signal. The origin of the chiral-specific signal can be understood from the nonzero orientational averages in Equations (6.8) and (6.9). Note that a chiral uniaxial assembly alone is thus insufficient to observe F-ORD experimentally; a nonzero orientational average in θ is required and implied by the term polar order. Using a lipid monolayer on an air/water interface as an example, the aliphatic moiety for the ensemble is virtually always oriented away from the bulk liquid, giving the whole interface a polar orientation. In contrast, a bilayer of those same lipids can exhibit alignment about a unique axis, but no preferred orientation (i.e., polar order) and no corresponding F-ORD response. The B_H coefficient is given by the following equation as a function of orientational parameters and the transition moments of the fluorophore.

$$\begin{aligned}B_H &\propto \left\langle\sin^2\theta\cos\theta\sin\psi\cos\psi\right\rangle\left(\left|\mu_z^f\right|^2\left|\mu_x^a\right|^2\right) - \left\langle\sin^3\theta\sin\psi\right\rangle\left(\left|\mu_z^f\right|^2\left|\mu_x^a\mu_z^a\right|\right)\\ &= \left|\vec{\mu}^f\right|^2\left|\vec{\mu}^a\right|^2\left(\sin^2\delta\left\langle\sin^2\theta\cos\theta\sin\psi\cos\psi\right\rangle - \sin\delta\cos\delta\left\langle\sin^3\theta\sin\psi\right\rangle\right)\end{aligned} \tag{6.10}$$

From Equation (6.10), three requirements must be met to exhibit chiral-specificity in the fluorescence produced from uniaxial assemblies: i) the assembly exhibits polar order, such that the

expectation values over the polar tilt angle θ are nonzero, ii) the arrangement of the plane containing the absorption and fluorescence transition dipoles must exhibit a chiral twist such that the expectation values over ψ are nonzero, and iii) the transition moments for absorption and fluorescence are nonparallel such that δ is nonzero. In the limit of a uniform distribution in ψ, both orientational averages in Equations (6.8) and (6.9) approach zero.

The magnitude of the F-ORD signal can be interpreted in the context of a linear intensity difference (LID) measurement most analogous to circular intensity difference measurements with circularly polarized excitation. In LID measurements, the polarized fluorescence intensity is measured for $+45°$ and $-45°$ linear polarizations, with the difference in the detected intensity directly connected to the F-ORD rotation angle.

$$LID \equiv \frac{I_H(+45) - I_H(-45)}{I_H(+45) + I_H(-45)} = \frac{B_H}{A_H + C_H} \tag{6.11}$$

By inspection of Equation (6.10) it is noted that maximal B_H coefficients are achieved when $\theta = 54.7°$, $\delta = 90°$, and $\psi = 45°$. Explicit evaluation for the theoretical maximum using Equations (6.11) and (6.4)-(6.6) yields a dichroic ratio of 0.808. This is approaching the theoretical maximum dichroic ratio for electronic CD of 1, but dichroic ratios typically observed for magnetic dipole effects in isotropic media are on the order of 10^{-3}. It is posited that since the F-ORD mechanism arises purely from electric dipole contributions, the generated signal may be much greater.

6.4 Evidence of F-ORD

Evidence supporting the potential relevance of this proposed mechanism can be found in single molecule fluorescence studies of chiral molecules first reported by Barnes and coworkers, reproduced with permission in Figure 2. In that study, Barnes and coworkers observed dissymmetry parameter *g* related to differences in fluorescence intensity for right versus left circularly polarized excitation.[2] Clear statistically significant differences were observed in the histograms of *g* values produced for the two senses of helicity for the chiral fluorophores used.

In follow-up work by Cohen and coworkers,[19-20] it was suggested that the dichroic mirrors altered polarization incident to the sample. It was demonstrated that the dichroic mirror induced phase shifts and had different reflectivity efficiencies. Furthermore, corrections to ensure pure circular polarizations at the sample resulted in significant decreases in the spread and magnitude of *g*-values obtained. Cohen and coworkers concluded that the observation of nonzero dissymmetry could be attributed to the presence of linear dichroism rather than circular dichroism. In subsequent studies by Barnes and coworkers, a reduction in dissymmetry was confirmed when particular attention was taken to remove potential artifacts from linear dichroism, although the underlying sensitivity to absolute chirality remained.[21]

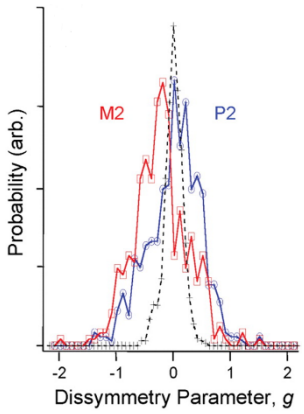

Figure 6.2 Normalized fluorescence-detected circular dichroism (FDCD) histogram published by Barnes and coworkers.[2] The blue and red traces represent the signal from right (*P2*) and left (*M2*) handed helical structures, respectively. Mean *g* values reported were 0.52 and -0.63, respectively; 2 orders of magnitude greater than the bulk response. Reproduced with permission.

Interestingly, no subsequent work has to our knowledge appeared to address what are arguably the most exciting observations in the original study; namely the observed chiral specificity in the single molecule linear dichroism contributions to the Barnes' and coworkers' measurements. The results shown in Figure 8.2 demonstrate clear differences in the mean values of the dissymmetry factors for the two diastereomers at the interface. These observations can potentially be explained through the F-ORD mechanism proposed herein.

The presence of unanticipated F-ORD contributions in the prior experimental design can be understood by considering the influence of the Jones matrices for the optical path in the original study, as subsequently detailed by Cohen and coworkers. In brief, the Jones matrix describing the polarization state of the incident circularly polarized light upon reflection from a dichroic mirror can be broken up into a complex component describing elliptically polarized light along the eigenpolarizations of the mirror and a purely real component corresponding to $\pm 45°$ linear polarization.

$$\begin{aligned}\vec{e}^{\,a} &= \begin{bmatrix} r_H^a & 0 \\ 0 & r_V^a \end{bmatrix} \tfrac{1}{\sqrt{2}} \begin{bmatrix} 1 \\ \pm i \end{bmatrix} = \begin{bmatrix} |r_H| & 0 \\ 0 & |r_V| e^{i\Delta} \end{bmatrix} \tfrac{1}{\sqrt{2}} \begin{bmatrix} 1 \\ \pm i \end{bmatrix} \\ &= \tfrac{1}{\sqrt{2}} \begin{bmatrix} |r_H^a / r_V^a| - \sin\Delta \\ \pm i \cos\Delta \end{bmatrix} + \tfrac{\sin\Delta}{\sqrt{2}} \begin{bmatrix} 1 \\ \pm 1 \end{bmatrix}\end{aligned} \tag{6.12}$$

In Equation (6.12), r_H^a and r_V^a refer to the complex-valued amplitude reflection coefficients for the dichroic mirror (assuming the *p* and *s* eigenpolarizations coincide with the *H* and *V* reference frames of the image), and Δ is the phase shift in the polarization state induced by the mirror, given by $\Delta = \arg(r_H^a / r_V^a)$. From Equation (11), the difference in detected intensity for $\pm 45°$ is directly connected to the chiral-specific coefficients B_H and B_V. For detection of horizontally polarized light the following equality emerges.

$$I_H\left(+45^0\right) - I_H\left(-45^0\right) = 2\left(\tfrac{1}{2} B_H\right)\left|t_H^f\right|^2 \tag{6.13}$$

Taking advantage of the identity $B_H = -B_V$, the integrated fluorescence intensity difference arising from residual linear dichroism can be connected to the transmission coefficients of the dichroic mirror along the return path at the fluorescence wavelength through the following relationship.

$$I_{tot}\left(+45^0\right) - I_{tot}\left(-45^0\right) = B_H\left|t_H^f\right|^2 + B_V\left|t_V^f\right|^2 = B_H\left(\left|t_H^f\right|^2 - \left|t_V^f\right|^2\right) \tag{6.14}$$

From previous measurements of dichroic mirrors performed by the Cohen group,[19] reasonable values of $\Delta = 0.79$ were recorded for one dichroic mirror, corresponding to as much as ~1/2 the incident light potentially contributing to linear dichroism. From Equation (6.13), the presence of a significant difference in transmissivity for the eigenpolarizations of the dichroic mirror prior to detection could provide one possible explanation for the observations of large dissymmetry factors directly tied to the sense of chirality. Conversely, unpolarized detection of the total fluorescence should yield no selectivity for chirality, consistent with the two transmissivity terms in Equation (6.13) being equal. It would also explain the reductions in this sensitivity when using pure circular polarizations, corresponding to the case of $\Delta \cong 0$. Note that the reduction in signal observed with circularly polarized light is entirely consistent with the Cohen response in 2009, where it was noted that careful treatment of polarization purity to ensure pure CPL at the sample resulted in sharp collapse of the distribution of g about zero. Finally, it suggests that the overall sensitivity to chirality could be significantly improved yet further through optimization of the experiment to explicitly target F-ORD measurements.

6.5 Alternative Origins of Chiral Specificity

It is interesting to compare and contrast the proposed mechanism with previous work by Cohen and coworkers, in which "superchiral" light arises in the region in the vicinity of nodes present at highly reflective interfaces.[19, 22-23] In brief, the electric dipole contributions approach zero at a node, while the same effect does not arise for magnetic dipole contributions. As such, suppression of the electric dipole induced fluorescence results in a relative enhancement in the chiral-specific magnetic dipole contributions and a correspondingly large dissymmetry factor. This mechanism produces a greater g value with a maximum signal detected for pure circularly polarized light and zero signal for linearly polarized light. In contrast, the F-ORD mechanism, as detailed above, yields a minimum g value for circularly polarized light as evidenced by the 2009 response to the original Barnes manuscript.[19] In a follow-up manuscript by Barnes and coworkers in 2012, it was shown that careful treatment to reduce linear polarization contamination resulted in a reduction in dissymmetry parameter g, consistent with the predictions of F-ORD and contrary to those of the "superchiral" light mechanism.[24]

It is worthwhile to compare and contrast the chiral-specific response predicted for fluorescence with the fully electric dipole allowed chiral-specific Raman from oriented assemblies first considered several years ago by Efrima and subsequently refined by Hecht and Barron.[25-26] In brief, symmetry arguments indicated the possibility of electric dipole-allowed chiral-specific Raman optical activity (ROA) in chiral assemblies exhibiting polar order. In that work, electric dipole-allowed ROA was predicted to be possible from macroscopic symmetry arguments, with the ROA scaling with the anti-symmetric component of the Raman tensor. Since anti-symmetry is enhanced near electronic resonance, ROA was predicted to be enhanced in resonance Raman measurements. These predictions were subsequently confirmed experimentally and put to great advantage in surface-enhanced Raman measurements.[27] This confirmation has led to a recent growth in SEROA arising from molecules assembled at the surfaces of metal nanoparticles. Despite the successes of SEROA, few detailed molecular level interpretations have emerged for the origins of the chiral specificity in terms of the molecular orientation distribution at the interface, such that ab initio interpretations of SEROA measurements for absolute chirality determination remain challenging.

6.6 Outlook of Derived Model and Conclusions

More recent independent studies of coherent four-wave mixing of uniaxial assemblies[17] may potentially help clarify the origin of the chiral specificity of spontaneous Raman in SEROA measurements and their possible connection to chiral-specific fluorescence. In that work, explicit expressions were derived for the orientational averages connecting the molecular frame to the interfacial frame for all coherent four-wave mixing measurements. Fortunately, both fluorescence and the spontaneous Raman processes can be treated mathematically with the same framework as four wave mixing, although with two of the four fields produced by the sample rather than one as in CARS. These general expressions are equally valid for spontaneous Raman and fluorescence, providing a route for clarifying the molecular-level requirements for both electric dipole allowed chiral-specific Raman and F-ORD.

In summary, a framework for the theoretical description of chiral-specific fluorescence was described. The proposed model imposes the following molecular constraints: i) the presence of a significant difference between the absorption and emission transition moment orientations within the molecular frame, ii) polar order of a uniaxial interface, and iii) ensemble chirality. The F-ORD chiral-specific signal was mathematically connected to the *B* polynomial coefficient in polarization rotation measurements and to linear intensity difference measurements of chiral assemblies. The model provides a novel electric-dipole allowed mechanism for chiral-specific fluorescence, which may explain the remarkable linear dissymmetry parameters reported by Barnes and Cohen previously. Furthermore, the described framework lends itself to future extension into the theoretical treatment of SEROA measurements, providing increased generality over previous treatments.

6.7 Acknowledgements

The authors gratefully acknowledge support from the NIH Grant Numbers R01GM-103401 and R01GM-103910 from the NIGMS. Support in the form of a Ross Assistantship from Purdue University is also graciously acknowledged.

6.8 References

1. Deng, F.; Ulcickas, J. R. W.; Simpson, G. J., Theoretical Foundation for Electric-Dipole-Allowed Chiral-Specific Fluorescence Optical Rotary Dispersion (F-ORD) from Interfacial Assemblies. *The Journal of Physical Chemistry Letters* **2016,** *7* (21), 4248-4252.

2. Hassey, R.; Swain, E. J.; Hammer, N. I.; Venkataraman, D.; Barnes, M. D., Probing the chiroptical response of a single molecule. *Science* **2006,** *314* (5804), 1437-1439.

3. Kohls, H.; Steffen-Munsberg, F.; Höhne, M., Recent achievements in developing the biocatalytic toolbox for chiral amine synthesis. *Current opinion in chemical biology* **2014,** *19*, 180-192.

4. Yasukawa, K.; Asano, Y., Enzymatic synthesis of chiral phenylalanine derivatives by a dynamic kinetic resolution of corresponding amide and nitrile substrates with a multi-enzyme system. *Advanced Synthesis & Catalysis* **2012**.

5. Gupta, A. K.; Kazlauskas, R. J., Substrate modification to increase the enantioselectivity of hydrolases. A route to optically-active cyclic allylic alcohols. *Tetrahedron: Asymmetry* **1993,** *4* (5), 879-888.

6. Syme, C. D.; Blanch, E. W.; Holt, C.; Jakes, R., A Raman optical activity study of rheomorphism in caseins, synucleins and tau. *European Journal of Biochemistrty* **2002,** *269*, 148-156.

7. Barron, L. D.; Hecht, L.; McColl, I. H.; Blanch, E. W., Raman optical activity comes of age. *Molecular Physics* **2004**.

8. Sreerama, N.; Woody, R. W., Estimation of protein secondary structure from circular dichroism spectra: comparison of CONTIN, SELCON, and CDSSTR methods with an expanded reference set. *Analytical biochemistry* **2000,** *287* (2), 252-260.

9. Kahr, B.; Freudenthal, J.; Gunn, E., Crystals in Light. *Accounts Chem. Res.* **2010,** *43* (5), 684-692.

10. Claborn, K.; Chu, A. S.; Jang, S. H.; Su, F. Y.; Kaminsky, W.; Kahr, B., Circular extinction imaging: Determination of the absolute orientation of embedded chromophores in enantiomorphously twinned LiKSO4 crystals. *Cryst Growth Des* **2005,** *5* (6), 2117-2123.

11. Rodrigues, S. P.; Lan, S.; Kang, L.; Cui, Y.; Cai, W., Nonlinear Imaging and Spectroscopy of Chiral Metamaterials. *Advanced Materials* **2014,** *26* (35), 6157-6162.

12. Lee, H.; Huttunen, M. J.; Hsu, K. J.; Partanen, M.; Zhuo, G. Y.; Kauranen, M.; Chu, S. W., Chiral imaging of collagen by second-harmonic generation circular dichroism. *Biomedical Optics Express* **2013,** *4* (6), 909.

13. Haupert, L. M.; Simpson, G. J., Chirality in Nonlinear Optics. In *Annual Review of Physical Chemistry*, Annual Reviews: Palo Alto, 2009; Vol. 60, pp 345-365.

14. Petralli-Mallow, T.; Wong, T. M.; Byers, J. D.; Yee, H. I.; Hicks, J. M., Circular dichroism spectroscopy at interfaces: a surface second harmonic generation study. *The Journal of Physical Chemistry* **1993,** *97* (7), 1383-1388.

15. Patterson, D.; Schnell, M.; Doyle, J. M., Enantiomer-specific detection of chiral molecules via microwave spectroscopy. *Nature* **2013,** *497* (7450), 475-+.

16. Lobsiger, S.; Perez, C.; Evangelisti, L.; Lehmann, K. K.; Pate, B. H., Molecular Structure and Chirality Detection by Fourier Transform Microwave Spectroscopy. *Journal of Physical Chemistry Letters* **2015,** *6* (1), 196-200.

17. Davis, R. P.; Moad, A. J.; Goeken, G. S.; Wampler, R. D.; Simpson, G., J., Selection Rules and Symmetry Relations for Four-Wave Mixing measurements of Uniaxial Assemblies. *J. Phys. Chem. B* **2008,** *112*, 5834-5848.

18. Moad, A. J.; Simpson, G. J., Self-consistent approach for simplifying the interpretation of nonlinear optical and multiphoton phenomena. *J. Phys. Chem. A* **2005,** *109*, 1316-1323.

19. Tang, Y. Q.; Cook, T. A.; Cohen, A. E., Limits on Fluorescence Detected Circular Dichroism of Single Helicene Molecules. *J Phys Chem A* **2009,** *113* (22), 6213-6216.

20. Cohen, A.; Tang, Y. Q., Reply to "Comment on 'Limits on Fluorescence Detected Circular Dichroism of Single Helicene Molecules'". *J Phys Chem A* **2009,** *113* (35), 9759-9759.

21. Hassey-Paradise, R.; Cyphersmith, A.; Tilley, A. M.; Mortsolf, T.; Basak, D.; Venkataraman, D.; Barnes, M. D., Dissymmetries in Fluorescence Excitation and Emission from Single Chiral Molecules. *Chirality* **2009,** *21* (1E), E265-E276.

22. Tang, Y. Q.; Cohen, A. E., Optical Chirality and Its Interaction with Matter. *Phys Rev Lett* **2010,** *104* (16).

23. Tang, Y. Q.; Cohen, A. E., Enhanced Enantioselectivity in Excitation of Chiral Molecules by Superchiral Light. *Science* **2011,** *332* (6027), 333-336.

24. Cyphersmith, A.; Surampudi, S.; Casey, M. J.; Jankowski, K.; Venkataraman, D.; Barnes, M. D., Chiroptical Dissymmetries in Fluorescence Excitation from Single Molecules of (M-2) Helicene Dimers. *J Phys Chem A* **2012,** *116* (22), 5349-5352.

25. Hecht, L.; Barron, L. D., RAYLEIGH AND RAMAN OPTICAL-ACTIVITY FROM CHIRAL SURFACES. *Chem Phys Lett* **1994,** *225* (4-6), 525-530.

26. Efrima, S., RAMAN OPTICAL-ACTIVITY OF MOLECULES ADSORBED ON METAL-SURFACES - THEORY. *Journal of Chemical Physics* **1985,** *83* (3), 1356-1362.

27. Vargek, M.; Freedman, T. B.; Lee, E.; Nafie, L. A., Experimental observation of resonance Raman optical activity. *Chem Phys Lett* **1998,** *287* (3-4), 359-364.

CHAPTER 7. HYPERSPECTRAL INFRARED IMAGING

7.1 Introduction

Infrared (IR) imaging provides chemical sensitivity, allowing identification of target moieties across heterogeneous systems and enabling label-free characterization of active pharmaceutical ingredients. Infrared spectroscopy in general has a rich history in the pharmaceutical sciences, primarily as a means of assessing chemical identity. When conducting accelerated stability tests, a critical step in the formulations development pipeline, APIs are exposed to elevated humidity and temperature ranges for extended periods of time to determine if the API is physically and chemically stable. If crystalline APIs transition from one polymorph to another under these conditions and the polymorphs exhibit varying degrees of solubility and consequently bioavailability medication may lose its potency or have unanticipated side-effects, endangering patients. Even small changes in the overall composition of the API can dramatically affect patient outcomes. As such, when analyzing these samples it is critical to evaluate structure on a per-particle basis, as bulk measurements such as differential scanning calorimetry, IR spectroscopy, and the standard of X-ray diffraction of the whole powdered sample will average their results over the ensemble. Infrared imaging enables direct analysis of single particles in a multiplexed measurement, allowing heterogeneous distributions of chemical identity to be identified and classified based on spectral features, however challenges associated with image resolution and acquisition speed continue to impede widespread adoption.

Historically, IR imaging has been enabled by Fourier-transform IR spectroscopic detection coupled with sample-scanning.[1] This approach enables high signal-to-noise measurement of the IR spectra, but at cost of imaging speed, although recent developments in focal plane array detectors have vastly improved imaging speed. More recent work has leveraged the giant advances in solid-state IR sources through the advent of quantum cascade lasers (QCLs). These relatively narrow-band sources emit light at IR wavelengths, operate at room temperature, and produce milliwatts of radiation.[2] Raster scanning, the conventional method of point-scan imaging, acquires an image a single pixel at a time by scanning a single line, then moving down to a second line and repeating the process. For single-wavelength detection this can still be quite fast; in chapter 2 raster scanning via synchronous digitization was achieved at video rate.[3] However, by leveraging image reconstruction and inpainting techniques these

speeds can be improved upon greatly. In the monochromatic regime, simply adjusting the scan pattern from raster to a Lissajous trajectory, whereby the two scan axes for imaging are driven by frequency offset sine waves, can increase framerates up to kHz with the same frequency laser.[4] This illumination pattern has the advantage where you sample from all four quadrants of the image much more rapidly. In addition to challenges associated with imaging speed, IR absorbance/transmittance microscopies are further hamstrung by the diffraction limit, which caps spatial resolution to a maximum resolution on the order of 5 μm for typical LWIR sources.

While the potential utility of IR imaging for chemical characterization is undisputed, direct application to pharmaceutical systems has been hindered by the relatively low spatial resolution afforded by the diffraction limit of light in the mid-IR. Resolution of far-field imaging configurations is at best diffraction limited, which for spectra centered around 10 μm enables on 5 μm spatial resolution, insufficient to image small crystals. Practically, the poor collimation afforded by broadband IR sources reduces effective resolution to the order of detector pixel sizes.[5] Previous work has utilized synchrotron radiation to enhance collimation and consequently achieve imaging at the diffraction limit.[6] Alternative approaches to enhance resolution include the use of scanning near-field approaches and photothermal induced resonance methods, which provide significant resolution enhancements at the cost of imaging speed and measurement complexity.[7-9] Far-field photothermal approaches provide optical resolution by detecting the change in refractive index associated with lensing from thermal expansion following stimulation with IR-wavelengths.[10, 11] These methods typically leverage the high-peak power of QCLs as illumination sources, but because the measurement is based on small changes in intensity from the thermal lensing effect, experimental design and implementation can be challenging. In contrast to this approach, a digital image fusing architecture is proposed where localization via segmentation of visible-wavelength brightfield images is applied to constrain chemical classification from IR imaging to features at visible-wavelength resolution.

In this chapter, methods to enhance spatial resolution and imaging speed in IR microscopy are presented. The design of a hyperspectral IR microscope with co-propagating beams ranging from 1190–1340 cm^{-1} in the IR and 640 nm in the visible. Initial application of the microscope was to image mixtures of dichloromethane and water, which were subsequently classified via K-means clustering.

To improve spatial resolution, IR transmittance images and visible laser transmittance images were acquired simultaneously. IR and visible images were registered via cross-correlation USAF-1951 test grid images obtained for both wavelength regimes. This approach was initially applied to of thin porcine liver, and subsequently tested on mixed spherical particles of silica and polymethylmethacrylate. Following image registration, chemical classification was conducted via a single layer neural network on each pixel within the IR images. Image segmentation conducted via image morphological analysis enabled selection of individual particles within the visible image. A consensus chemical classification for pixels within each particle was then utilized to determine particle chemical identity which was then visualized by color mapping the original red-intensity image. In this manner, chemical sensitivity from IR spectroscopy was encoded into visual images with resolution on the order of the visible wavelength, affording an order of magnitude gain in theoretical resolution over direct imaging with IR wavelengths.

7.2 Experimental Methods

7.2.1 Instrument Apparatus

The hyperspectral microscope is depicted in **Fig. 7.1**. In brief, a custom 32-channel LWIR QCL array with a wavenumber range of 1190–1340 cm^{-1} (Pendar Technologies) was used as the absorption light source. A 640 nm laser diode (Thorlabs) was used as the bright-field light source. The two laser beams were combined using a germanium window (Thorlabs). The 640 nm laser diode beam was 4f coupled to a germanium window with two lenses to enable fine adjustment of the collimation at the point of beam combination to correct for chromatic aberration. The copropagating beams were expanded twice with two sets of lenses and scanned across

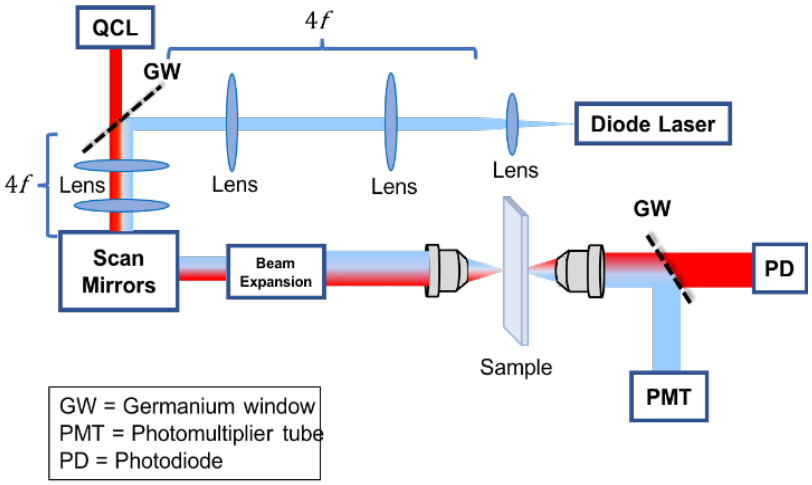

Figure 7.1 Instrument schematic of the LWIR hyperspectral microscope. 640 nm beam is emitted from the diode laser and is combined with 32-channel LWIR beam emitted from the QCL.

the sample using a pair of galvanometer mirrors (ScannerMAX). A 15× 0.4 NA reflective Cassegrain objective (Edmund Optics) was used to focus the beams onto the sample. Light from the sample plane was recollimated using a collection lens and a germanium window was used to separate the 640 nm beam from the LWIR beam. 640 nm light was detected using a photomultiplier tube (Hamamatsu). LWIR light was detected using an LWIR-sensitive photodiode (Vigo Systems). IR compatible lenses (Thorlabs) were used when focusing the LWIR beam. Responses of the detectors were digitized synchronously with a 10 MHz clock using a digital oscilloscope card (ATS9350, AlazarTech). Custom software (MATLAB) was used to down-sample raw data to coincide with LWIR laser pulses and remap the down-sampled data onto a set of 256 pixel × 256 pixel LWIR images (one for each QCL channel) and one 256 pixel × 256 pixel 640 nm bright-field image. K-means clustering was used to assign chemical identity in images of mixtures. The high-resolution 640 nm image and the low-resolution LWIR images were combined using custom software (MATLAB) to create a merged image containing IR spectral information encoded in an RGB color map.

7.2.2 Digitization and Image Acquisition

A significant portion of the development effort in building this microscope was focused on image reconstruction and acquisition software. In this chapter, two separate methods were used for acquiring data and generating the images. Initial efforts described in sections 7.3 and 7.4 used a frame-sync method to trigger the beginning of the image. This approach was incompatible with averaging many frames, however, as the configuration of the PCIExpress Alazar digitizer card (model ATS9350) required a digitization frequency of 100 MHz or greater to utilize a direct external fast clock for synchronizing the electronics. Because the laser frequency was much slower than this, on the order of 1 MHz, this resulted in a large amount of data digitized per frame, the handling of which becomes unsustainable beyond a few frames at image sizes of 256×256 pixels. To combat this and enable signal averaging across multiple frames an approach based on triggering digitization based on the QCL cycle initiation was developed. In this configuration, digitization is triggered by a function generator which triggers both the Alazar card and QCL in a synchronized fashion. A custom MATLAB script is used to acquire 6240 digitization events at a rate of 160 MHz, corresponding to an acquisition duration of 40 μs. The resulting vector of voltages is then multiplied by an integration matrix of dimensionality n×6240, where n is the number of active QCL channels. A blank acquisition is utilized to define the

integration matrix, where the edge of each QCL peak is found via thresholding and taking the gradient. Each row in the matrix contains ones at time points where a single channel is firing, such that multiplying the $n\times6240$ matrix by the digitized buffer yields a vector of 22 elements, each one corresponding to a single pixel in one of the n images acquired. This approach allows redundant data points and digitized dead-time to be eliminated from computational overhead and acquire longer streams of data overall.

7.2.3 **Sample preparation**

Dichloromethane was acquired from Sigma-Aldrich. Spectroscopy was performed by pipetting small aliquots of DCM onto UV-grade CaF_2 obtained from Crystran LTD. For mixtures of H_2O and DCM, the two fluids were briefly agitated in a sealed vessel before being pipetted onto a CaF_2 slide. Pig liver was acquired from the Boilermaker Butcher Block at Purdue University. Liver tissue was frozen and sectioned to 5 μm thickness on a Leica CM 1860 cryostat, then mounted on UV-grade CaF_2 obtained from Crystran LTD. Poly(methyl methacrylate) (PMMA) and glass beads were obtained from Cospheric. Training data for particle classification studies were acquired from images with only PMMA beads or only glass beads on a CaF_2 slide obtained from Crystran LTD. Test data were acquired from images with PMMA beads and glass beads mixed together on a CaF_2 slide.

7.2.4 **Machine learning methods**

Visible images from the training data were segmented using k-means clustering (k = 2 for images of pure PMMA/silica), generating a set of approximately 10,000 training spectra for each class. Visible images from the test data were segmented using a circle-finding algorithm (imfindcircles in MATLAB). A feed-forward artificial neural network (ANN) from the machine learning toolbox in MATLAB was used for image segment classification. The ANN had an input layer of an infrared spectrum, a single hidden layer with ten neurons, and an output layer with three neurons, one neuron for each class. The activation function that produced the output layer was a classifier such that only one of the output neurons was equal to one and the rest were equal to zero. The ANN was trained using pixels from images of known composition. Each pixel was classified initially before image

segmentation. After segmentation of the visible image, pixels were grouped based on the segmentation and each segment was classified based on the class with the greatest number of pixels.

7.3 Hyperspectral Imaging

Initial efforts in hyperspectral imaging were targeted on a simple mixture of immiscible fluids. Dichloromethane (DCM) and water exhibit distinct absorbance spectra in the region of 1200-1350 cm^{-1} where the QCL array probes. **Figure 7.2A-B** demonstrates the absorbance spectrum for DCM obtained in the microscope described in **Figure 7.1** with the beam at a fixed position. A single spectrum can be acquired from the QCL array in as few as 9.6 µs, corresponding to 32 channels with a fixed pulse width of 300 ns. When firing the QCL for multiple cycles, the duty cycle should be constrained below 2% per channel, or 20% overall. This constraint for 32 channels was achieved using 200 ns pulse widths followed by 800 ns dead time before firing the next channel. The overall firing frequency of the QCL array was thus 1 MHz, yielding a spectrum from 50 cycles in 1.6 ms dictated by the total of 32 channels.

Following acquisition of the hyperspectral images displayed in **Figure 7.2C**, the data dimensionality was reduced from the fully hyperspectral data cube of 256×256×32 to a Boolean classification image of 256×256. Reduction was achieved by projecting each spectrum onto the first and second principal components of the data set, and subsequently utilizing K-means clustering (K=2) to distinguish pixels containing water and DCM. The output binary image is

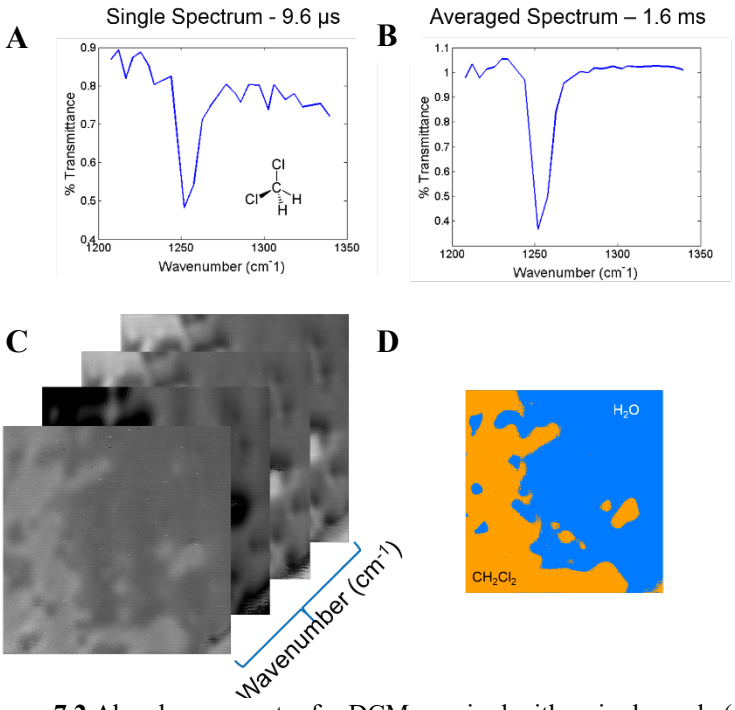

Figure 7.2 Absorbance spectra for DCM acquired with a single-cycle (A) and 50 cycles (B) of the array pattern. When imaging, simultaneously acquired images at each wavelength from the array (C) enable K-means clustering to distinguish DCM from H_2O (D).

shown in **Figure 7.2D**. In this initial demonstration the power of chemical specificity via IR spectroscopy was shown; subsequently described implementations utilize the co-propagating visible beam as a contrast agent with a diffraction limit on the order of 10× smaller than the IR beam.

Figure 7.3 demonstrates the application of a naïve fusion approach to merge the visible and infrared images of a 5 μm thick section of porcine liver on CaF_2. In this approach, evenly dispersed wavelength channels were selected as single-color channels within an RGBCYM colormap where the length of the color vector is normalized by the visible channel. In other words, intensity maps structure, while hue maps chemistry. Prior to imaging the porcine section, a blank image was acquired, enabling the construction of a percent transmittance image in the IR. While the IR images provide chemical specificity, localization with visible-wavelength diffraction limits can be inferred from the fused image.

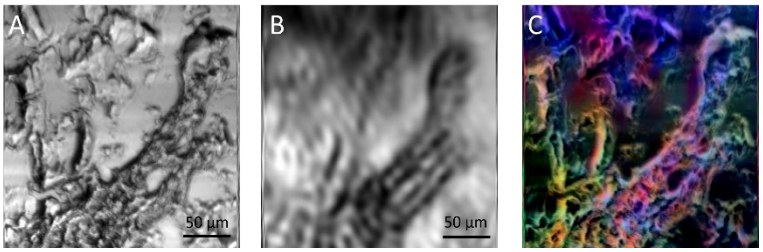

Figure 7.3 Bright field laser transmittance image acquired with 639 nm illumination (A) and laser transmittance in the 1200-1350 cm-1 spectral window (B) can be combined to generate an image with diffraction-limited resolution in the visible, but chemical specificity from the infrared (C). The 1244 cm-1 channel is shown in B.

The QCL's ability to rapidly modulate wavelength by turning on and off distinct single-mode channels affords this microscope a degree of speed incompatible with pixel-detector FTIR-based microscopes. Focal plane array (FPA) based systems can image large fields of view rapidly, but at significant cost. At the time of this writing, current state of the art commercial IR microscopes can be acquired with 128×128-pixel detectors – pushing to higher pixel count is currently a challenge associated with the detector technology. In contrast, scan-based systems can have an arbitrary number of pixels within the image, governed by an interplay between the diffraction limited spot-size of the IR beam and angle of entry for light entering the back of the objective (in beam-scanning experiments) or number of scan steps afforded by a mechanical stage. Image speed can be further improved in scanning experiments by leveraging the programmable nature of the QCL array with more efficient scan patterns than the raster

approach. The next section will discuss methods which were explored in improving image speed with IR imaging.

7.4 Sparse-Sampling in Time and Space

One powerful aspect of the QCL array approach to hyperspectral imaging is the ability to modulate wavelength with arbitrary patterns in time. Combined with flexible beam-scanning optics, e.g., galvanometers controlled by arbitrary waveform generators, both the spatial and wavelength domains can be scanned in creative patterns. Sparse-sampling methods have been employed with great success to improve the rate of imaging due to the inherent redundancy of adjacent pixels.[4] Initial efforts in enhancing imaging speed leveraged a sparse raster approach, illustrated in **Figure 7.4**. In this approach, each subsequent laser pulse from the QCL array is assumed to be in a unique location, as is shown by the varying color across the field of view. The net outcome is that for objects within the field of view, such as crystals, some wavelengths may probe the sample while others do not. For a single wavelength this sparse raster generates a grid of sampled positions, with unsampled pixels dictated by the firing frequency of that laser channel and the scan speed.

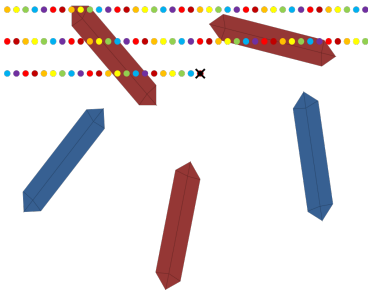

Figure 7.4 Sparse raster approach used to enhance imaging speed. The beam scanned continuously while wavelengths emitted from the QCL array was cycled.

Considering the image built from a single wavelength, the fast mirror axis continuously scanning results in a sparsely sampled raster pattern with only 3% total sampling (1/32 of total pixels). A 96×96-pixel acquisition in turn can be inpainted to a 3096×3096 image. **Figure 7.5** demonstrates this for the USAF 1951 test grid. With this sparse-sampling approach, image acquisition was sped up by a factor of 32.

The USAF 1951 test grid is well-suited for demonstrating this method because it exhibits a simple pattern, the information content of which is constrained into a few finite spatial frequencies. As images become more complex and contain higher spatial frequency information sparse-sampling approaches require greater and greater percent sampling of the field of view. In previous work published by the Simpson group, sampling percentages below 20% were utilized to achieve kHz framerates in imaging the USAF 1951 grid.[4] In that work, total imaging frequency could be accelerated due to utilization of two high-Q resonant mirrors to sample in a Lissajous pattern. This initial demonstration of sparse sampling with a QCL array provides a slight contrast to this work, in that it represents instead a first step towards n-dimensional sparse sampling.

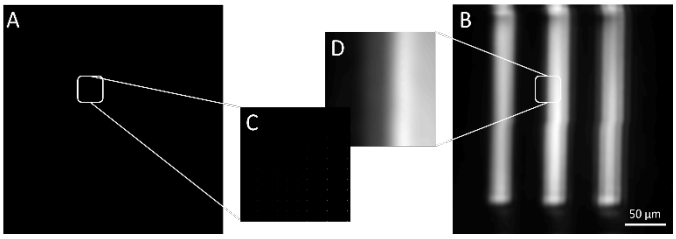

Figure 7.5 Sparse raster approach applied to imaging the USAF 1951 test grid at 1244 cm^{-1}. Full images before (A) and after (B) inapainting are shown. Inset images show a 28×28 µm field of view before (C) and after (D) inpainting

In the spatial domain, it is common for two adjacent pixels to contain similar amplitudes; in other words, the spatial information is slowly varying across the field of view for many images. Similarly, the spectral domain carries this relationship as well – it is uncommon in the condensed phase to find extremely sharply peaked resonances due to the variety of thermal states available in such systems. Of course, exceptions exist – notably within the fingerprint region of the infrared. As such, care should be taken when attempting to inpaint a data cube utilizing correlations across the spectral domain. In cases where the linewidth of resonances in the condensed phase far exceed the step in wavelength associated with each QCL channel, as is anticipated for the amide III stretch of proteins, these correlations can be leveraged to further enhance imaging speed. While **Figure 7.5** does not harness correlations in the spectral domain, the algorithm used for interpolation of the sparse image is amenable to extension into the third dimension. A discrete cosine transform based interpolation, previously reported by Garcia, was used to inpaint the sparsely sampled image.[12,13] In brief, this approach assumes a smoothly varying, noisy data set with possible missing data and smooths the data via discrete cosine transform (a purely real discrete Fourier transform) with penalized partial least squares. When applied to smooth data, a bisquare weighting factor improves robustness by reducing the impact of outliers. In the context of inpainting, the smoothing parameter is set to an arbitrarily

small value to reduce change in the sampled data points. The difference between the originally sampled data points and their value following the inpainting procedure can be used as an assessment of reconstruction error. It is the goal of the algorithm to generate data at the unsampled locations such that the inverse cosine transform minimizes these errors.

This work demonstrates the capacity for improving imaging speed in the infrared via patterned illumination. In addition to changes in the spatial sampling that are afforded by patterns like sparse-raster and the Lissajous scan, arbitrary wavelength patterns programmable on the QCL array provide an additional layer of flexibility. In this work the wavelength was ramped linearly across the range 1190–1340 cm^{-1}, but any pattern within the constraints of per-channel and total duty cycle may be used. This sampling pattern can be optimized on the basis of maximal information content, as well. Much like image formation, where the least informative pixel to measure after a single measurement is the adjacent pixel, in spectroscopy the adjacent wavelength channel will provide the least new information to generate the spectrum. From an information-theory perspective, a randomized QCL firing pattern would provide a greater amount of information per cycle, as it minimizes correlations between subsequent measurements.

With steps taken toward achieving faster hyperspectral imaging, the subsequent section will discuss methods to improve the ability to interpret those images.

7.5 Neural Network Based Particle Classification

Acquiring hyperspectral images provides a powerful tool for analyzing chemical content in heterogeneous systems, but displaying the information content inherent to these measurements in an easily digestible manner remains a challenge. To address this, dimension reduction in the form of chemical classification was applied to a mixed system of PMMA and silica microspheres. The spheres exhibit slightly different diameters, providing an alternative method of characterization to corroborate spectroscopy-based classification.

Before discussing the final approach taken, it is pertinent to describe several alternative architectures which were explored to reduce the higher dimensional spectroscopy information into a ternary

classification scheme (PMMA, silica, background). This type of approach is useful in industrial or medical settings where outlier detection provides a powerful diagnostic assessment of product material. For example, in the pharmaceutical industry, spectroscopic imaging can be implemented for polymorph detection when crystallizing active pharmaceutical ingredients, or to characterize distribution of product material in formulations.[14,15] In the field of biomedical imaging, hyperspectral signatures have been studied to identify malignant cells, such as those found in tumors.[16,17] However, a chemist should not have to view each wavelength channel of the corresponding image cube – rather, reducing the information content to a single image would provide the actionable information necessary to engage the appropriate response.

There are several methods available to reduce the dimensionality of a hyperspectral image. Arguably the most common approach involves an initial step of principal component analysis, selection of the most relevant components, and projection of the parent spectra onto those components. Each projection can then act as a single-color channel on an RGB or RGBCYM image. This method is analogous to the approach taken in section 7.3, but ideally should encode a greater amount of spectral information into the reduced image. Following reduction, the user must then interpret the corresponding image. While this method is flexible, due to the unsupervised nature of PCA, it has several distinct drawbacks. First, disentangling intensity effects from spectral differences across the field of view can be challenging – direct PCA analysis without proper pretreatment or normalization procedures will often yield a first principal component entirely related to intensity. Second, in order to determine the most critical principal components proper study with known material should first be conducted. Only a finite number of projections can be utilized when mapping to a fixed number of color channels, and so the choice of components to map can have a profound impact upon the final image. Lastly, by leaving the hyperspectral image up to human interpretation alone, image analysis can coincide with systematic error or bias by the user. Classification algorithms provide an alternative to this paradigm by reducing user bias on the output image.

Selection of an appropriate classification algorithm is nontrivial. If no training data is available, clustering methods like K-means clustering or fuzzy C-means provide an alternative. Like the PCA approaches discussed above, K-means alone on untreated data will largely classify images based on

overall intensity. If there are sufficient data available, supervised learning methods can be utilized to classify data. Linear discriminant analysis is one trained method to reduce the dimensionality of the data – subsequent classification can be achieved by means such as support vector machines. Neural networks provide an alternative strategy for classification given sufficient training data. The primary advantage of a neural network in this context is the ability to separate data with nonlinear functions.

To classify PMMA and silica, a single-layer feed-forward neural network was utilized. The training data were gathered by imaging samples of single components, with particles separated from background by k-means clustering of the visible laser transmittance images. The classification was based solely on single-pixel spectra, and thus feeding a testing image set into the neural network will result in classification on a single pixel basis. To impose visible-wavelength resolution on the final outcome, first the visible and red images were aligned. This was achieved by cross correlating the image of the USAF 1951 test grid obtained with each IR wavelength with the red reference image. The maximum in the cross-correlation determines the shift value for the x and y axes in the image. Once aligned, the visible laser transmittance image was segmented by using a circle-finding algorithm. Raw IR data cubes were fed to the neural network, resulting in a ternary classified image. The consensus classification for all pixels within a given circle determines the classification – regions not bounded by circles were determined to be background. **Figure 7.6** shows the results of the alignment and classification procedure. By inspection, despite some individual pixels being misclassified within the two glass spheres (green), the consensus is correct as corroborated by particle size. While this initial demonstration applied a

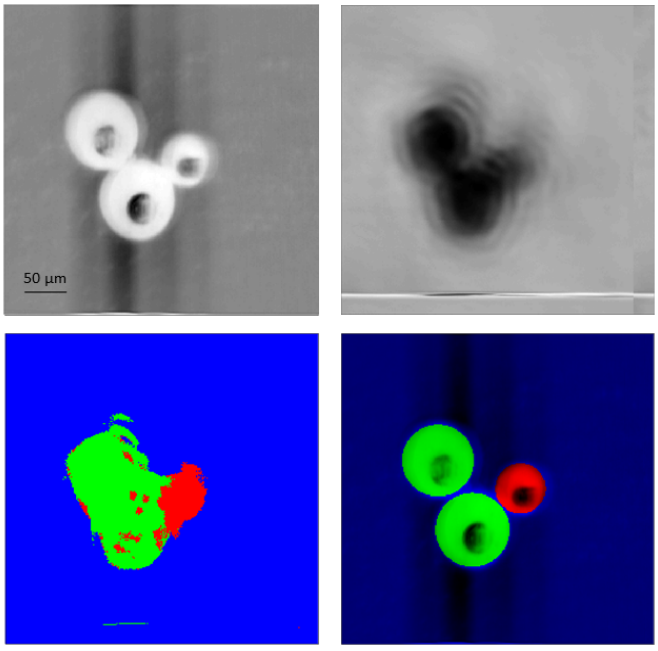

Figure 7.6 Images acquired via hyperspectral microscopy are displayed for the red laser transmittance (A), a single QCL channel at 1244 cm^{-1} (B), the classified IR image (C), and the segmented classified hyperspectral image (D). Spectra classified as PMMA are shown in red, while silica spectra are classified as green.

simple neural network to monodisperse particles of varying chemistry, further work can be done to apply this work to more pressing problems in image classification, such as polymorph discrimination.

7.6 Conclusions

A LWIR hyperspectral microscope was developed and utilized to image several chemical model systems. The microscope exhibits 32 channels with a spectral range of 1190–1340 cm^{-1} and a total image acquisition time of approximately two seconds using conventional raster scanning, yielding a 256 pixel × 256 pixel × 32 channel hyperspectral image stack. Initial efforts outlined in section 7.3 demonstrate spectroscopy capable of distinguishing DCM and water, as well as a corresponding hyperspectral image. Thin sections of porcine liver were imaged, using high amplitude transmittance channels as RGBCYM color channels. Image intensity encoded by the laser transmittance image fused results from visible and infrared images. Following initial demonstration of the feasibility of this microscope, studies to improve image acquisition speed via sparse sampling were conducted. A sparse-raster approach was employed, whereby each subsequent QCL channel was assumed to fire in a unique location along the raster scan trajectory. Individual IR channel images were then inpainted using a robust smoothing algorithm, providing a 32-fold image speed enhancement. A single hidden layer neural network with 10 neurons was trained to classify spectra as PMMA, glass, or background and applied to classification of a mixture. Merging LWIR images with 640 nm bright field images fused spectral information with visible-wavelength resolution. Image segmentation in this study was conducted via assuming spherical particles, however extension to rod or needle-like particles for alternative pharmaceutical formulations is trivial and requires only a template of the anticipated structure for use with image morphology methods.

7.7 References

1. Snively, C. M.; Katzenberger, S.; Oskarsdottir, G.; Lauterbach, J., Fourier-transform infrared imaging using a rapid-scan spectrometer. *Optics Letters* **1999,** *24* (24), 1841-1843.

2. Goyal, A. K.; Kotidis, P.; Deutsch, E. R.; Zhu, N.; Norman, M.; Ye, J.; Zafiriou, K.; Mazurenko, A. In *Detection of chemical clouds using widely tunable quantum cascade lasers*, Chemical, Biological, Radiological, Nuclear, and Explosives (CBRNE) Sensing XVI, International Society for Optics and Photonics: 2015; p 94550L.

3. Dow, Ximeng Y.; DeWalt, Emma L.; Sullivan, Shane Z.; Schmitt, Paul D.; Ulcickas, James R. W.; Simpson, Garth J., Imaging the Nonlinear Susceptibility Tensor of Collagen by Nonlinear Optical Stokes Ellipsometry. *Biophysical Journal* **2016,** *111* (7), 1361-1374.

4. Sullivan, S. Z.; Muir, R. D.; Newman, J. A.; Carlsen, M. S.; Sreehari, S.; Doerge, C.; Begue, N. J.; Everly, R. M.; Bouman, C. A.; Simpson, G. J., High frame-rate multichannel beam-scanning microscopy based on Lissajous trajectories. *Opt. Express* **2014,** *22* (20), 24224-24234.

5. Levenson, E.; Lerch, P.; Martin, M. C., Infrared imaging: Synchrotrons vs. arrays, resolution vs. speed. *Infrared Physics & Technology* **2006,** *49* (1), 45-52.

6. Nasse, M. J.; Walsh, M. J.; Mattson, E. C.; Reininger, R.; Kajdacsy-Balla, A.; Macias, V.; Bhargava, R.; Hirschmugl, C. J., High-resolution Fourier-transform infrared chemical imaging with multiple synchrotron beams. *Nature methods* **2011,** *8* (5), 413.

7. Knoll, B.; Keilmann, F., Near-field probing of vibrational absorption for chemical microscopy. *Nature* **1999,** *399* (6732), 134-137.

8. O'Callahan, B. T.; Lewis, W. E.; Möbius, S.; Stanley, J. C.; Muller, E. A.; Raschke, M. B., Broadband infrared vibrational nano-spectroscopy using thermal blackbody radiation. *Optics Express* **2015,** *23* (25), 32063-32074.

9. Centrone, A., Infrared Imaging and Spectroscopy Beyond the Diffraction Limit. *Annual Review of Analytical Chemistry* **2015,** *8* (1), 101-126.

10. Zhang, D.; Li, C.; Zhang, C.; Slipchenko, M. N.; Eakins, G.; Cheng, J.-X., Depth-resolved mid-infrared photothermal imaging of living cells and organisms with submicrometer spatial resolution. *Science advances* **2016,** *2* (9), e1600521.

11. Bai, Y.; Zhang, D.; Lan, L.; Huang, Y.; Maize, K.; Shakouri, A.; Cheng, J.-X., Ultrafast chemical imaging by widefield photothermal sensing of infrared absorption. *Science Advances* **2019,** *5* (7), eaav7127.

12. Garcia, D., Robust smoothing of gridded data in one and higher dimensions with missing values. *Computational Statistics & Data Analysis* **2010,** *54* (4), 1167-1178.

13. Wang, G. J.; Garcia, D.; Liu, Y.; de Jeu, R.; Dolman, A. J., A three-dimensional gap filling method for large geophysical datasets: Application to global satellite soil moisture observations. *Environmental Modelling & Software* **2012,** *30*, 139-142.

14. Li, C.; Zhang, D.; Slipchenko, M. N.; Cheng, J.-X., Mid-Infrared Photothermal Imaging of Active Pharmaceutical Ingredients at Submicrometer Spatial Resolution. *Analytical Chemistry* **2017,** *89* (9), 4863-4867.

15. Chowdhury, A. U.; Ye, D. H.; Song, Z.; Zhang, S.; Hedderich, H. G.; Mallick, B.; Thirunahari, S.; Ramakrishnan, S.; Sengupta, A.; Gualtieri, E. J.; Bouman, C. A.; Simpson, G. J., Second Harmonic Generation Guided Raman Spectroscopy for Sensitive Detection of Polymorph Transitions. *Analytical Chemistry* **2017,** *89* (11), 5958-5965.

16. Kong, R.; Reddy, R. K.; Bhargava, R., Characterization of tumor progression in engineered tissue using infrared spectroscopic imaging. *Analyst* **2010,** *135* (7), 1569-1578.

17. Mittal, S.; Yeh, K.; Leslie, L. S.; Kenkel, S.; Kajdacsy-Balla, A.; Bhargava, R., Simultaneous cancer and tumor microenvironment subtyping using confocal infrared microscopy for all-digital molecular histopathology. *Proceedings of the National Academy of Sciences* **2018,** *115* (25), E5651-E5660.

CHAPTER 8. MULTI-AGENT CONSENSUS EQULIBRIUM (MACE) FOR IMPROVING CHEMICAL STRUCTURE DETERMINATION

8.1 Introduction

The ultimate goal of computational chemistry is arguably to provide causal mechanistic understanding of chemical phenomena. In many cases that means there is some experimental observable and the aim is to understand why that outcome occurred. This general architecture of modeling as an explanatory method has had great success in a variety of applications, from chemical structure analysis to ionization energy prediction and modeling of thermodynamic quantities. However, as the complexity of the experimental observable increases it becomes a more difficult process. Spectroscopic matching, e.g., in vibrational analysis of flexible gas phase molecules, has found success in identifying conformational structure.[1-3] Unfortunately, such studies are limited in their throughput due to the necessity for modeling many discrete configurations of the system in question and utilizing manual matching methods to identify conformations most closely resembling experimental spectra. Such methods are costly in both computational and human resources. Other experimental methods, such as probes of excited state electronic structure for extended conjugated systems, semiconductors, and photosynthetic protein complexes, encounter difficulty in the theoretical description of the experimental outcome.[5] Computational scaling becomes a large obstacle in such cases; low-level methods are able to describe structure, but unable to predict more complex properties accurately due to lack of higher-order interactions. The classical paradigm of "compare and contrast" for theoretical studies with experiment provides no clear metric for success or failure with respect to the nature of differences (i.e., comparisons are generally qualitative in nature). Theoretical and experimental outcomes are generally performed entirely independently, with little or no feedback from the experimental constraints in the computational modeling. Model fusion provides one avenue to leverage existing theoretical frameworks as constraints upon models in computational chemistry, bridging the gap.

Fusion in the context of modeling refers to an approach which leverages multiple descriptions of the same system in order to generate a single description which incorporates the nuances of each model into the result. Applications of model fusion methods have had broad ranges of impact, from medical image reconstruction and denoising methods in X-ray computed tomography, to

sensor fusion for autonomous vehicle piloting and image reconstruction in celestial imaging.[7-9] Largely, these efforts have hinged upon creating an optimal reconstruction of the system measured. In more conventional chemical analyses, data and model fusion have been utilized for creation of electronic tongues, systems biology analysis on the basis of proteomics and metabolomics, and grape varietal classification, among many other applications.[10-12] The actual modality of fusion is as varied as the application, from naïve stacking of feature vectors to Bayesian inference frameworks; many methods are viable to combine disparate descriptions of the same chemistry.[11,12] Within computational and theoretical chemistry the term "model fusion" is uncommon, but any approach that merges multiple distinct computational descriptions of the same system can be considered as model fusion. Fragmentation based methods, for example, provide one mechanism by which multiple levels of theory can be integrated to model a complex chemical system.[13] Many of these methods utilize fusion either to combine multiple experimental characterizations, or to bring together several methods in computational chemistry; the direct fusion of empirical and computational models is a largely unexplored topic in the literature.

Recent work by Olsson et al. in the development of augmented Markov models (AMMs) informed statistical modeling of atomistic protein dynamics via empirical thermodynamic data.[14] These Markov state models (MSMs) fuse experimental averages with state-based transitions from atomistic MSM dynamical simulations, guiding the outcome of simulations based on known experimental observables. This work has already been extended to other applications in fusing multiple MSMs with reaction-diffusion simulations. However, MSMs are not trivially extended to applications utilizing quantum chemical modeling. There remains a need for flexible methods which can fuse a variety of models, including those that span quantum chemical descriptions with classical descriptions. The multi-agent consensus equilibrium (MACE) approach described in this work is a general architecture capable of fusing a both computational and experimental models of chemistry.

In this work, multi-agent consensus equilibrium is described and demonstrated for model fusion of *ab initio* chemical calculations and experimentally determined empirical models of chemical structure. A proof-of-concept model fusion for a test-bed system of H_2 as a simple harmonic diatomic is reported. Following validation, MACE is utilized to fuse the results from multiple

computational chemistry methods including Møller-Plesset 2nd order perturbation theory (MP2), density functional theory (DFT), Hartree-Fock (HF), and semiempirical PM3 method for a suite of small organic molecules. Lastly, fusion of empirical methods with computational modeling is demonstrated, combining an empirical model of the moment of inertia with four quantum chemical models. Results are presented for several small organics, and with proper weighting of the experimental agent, recovered structures have a lower RMSD with experimental structures than CCSD(T)/cc-pVTZ optimized structures.

8.2 Theoretical Foundation and Algorithm

Before formally defining the MACE criterion, several definitions will clarify the concept. The column vector $\mathbf{X} = \begin{bmatrix} X_1^T & \cdots & X_N^T \end{bmatrix}^T$ denotes the concatenated set of N state vectors. Each state vector describes the state of the system; for example, in geometry optimization, as conducted in this work, the state vector can be the set of atomic coordinates describing nuclear locations for each atom in a molecule. As an equilibrium calculation is conducted, the state vector describing each agent is updated according to the MACE step. The operator $\mathbf{F}(\mathbf{X})$ in turn is formed by the stack of agent operators in the MACE computation, as shown below.

$$\mathbf{F}(\mathbf{X}) = \begin{pmatrix} F_1(X_1) \\ \vdots \\ F_N(X_N) \end{pmatrix} \tag{8.1}$$

The broadcast mean operator $\mathbf{G}(\mathbf{X})$ is defined below, which takes the arithmetic mean of all agents' state and then broadcasts it to an array of the same dimensionality as X. This mean can be weighted using the set of weights $\vec{w} = \begin{bmatrix} w_1 & \cdots & w_N \end{bmatrix}^T$ to place a greater emphasis on the contributions of some agents over others.

$$\mathbf{G}(\mathbf{X}) = \begin{pmatrix} \bar{X} \\ \vdots \\ \bar{X} \end{pmatrix}; \bar{X} = \sum_{n=1}^{N} w_n X_n; \quad \sum_{n=1}^{N} w_n = 1 \tag{8.2}$$

Formally, MACE is a mathematical criterion where the operation $\mathbf{F}(\mathbf{X})$ returns a vector of states equal to the result of the broadcast mean, as shown in equation (8.3) below.

$$\mathbf{F}(\mathbf{X}) = \mathbf{G}(\mathbf{X}) \tag{8.3}$$

It is useful to briefly discuss the approach to achieving MACE in practice. It has been previously shown that when each agent F_n corresponds to a proximal map, the solution to the consensus equation (8.3) is equivalent to the solution of the optimization problem formulated by the sum of all agent functions.[15] The proximal map of the function $f_n(v)$ is defined below, where σ is some measure of uncertainty associated with the function $f_n(v)$.

$$F_n(x) = \arg\min_v \left\{ \frac{\|v - x\|^2}{2\sigma^2} + f_n(v) \right\} \tag{8.4}$$

Proximal maps can be computed analytically, which provides a convenient transformation for optimization where analytical derivatives are difficult to calculate. Although originally formulated for use with proximal maps, subsequent work extended MACE to alternative agents which behave similarly to proximal maps, including more general maps that start from some input position and take a step towards the minimizer of a convex function.[16] In the present study F_n is the gradient descent update operator, given below. Operators that produce a new state vector of the same dimensionality are compatible with the MACE architecture; other applications of the MACE framework have leveraged alternative objective functions to generate a consensus, e.g., among denoisers in 4D X-ray CT.[17]

$$F_n(X_n) = X_n - \gamma \nabla f_n(X_n) \tag{8.5}$$

In the above expression, $\nabla f_n(X_n)$ is the gradient of an objective function to be optimized, γ is a fixed parameter corresponding to the step size. Furthermore, the equilibrium state can be written as a fixed point on the map $\mathbf{T}$ that is a sum of all agent functions as shown in equation (8.6) below. With this fixed point formulation, Mann iteration can be used to optimize the map.[18] A more complete description of this procedure can be found in reference 11.

$$\begin{aligned} (2\mathbf{G} - \mathbf{I})(2\mathbf{F} - \mathbf{I})v &= v \\ \mathbf{T} &= (2\mathbf{G} - \mathbf{I})(2\mathbf{F} - \mathbf{I}) \end{aligned} \tag{8.6}$$

Practically, it is convenient to split the $\mathbf{T}$ operator into several lines of code. Algorithm 1 shows the procedure for achieving MACE. While the criterion has not been achieved the algorithm applies each of the bracketed terms in equation (8.6) sequentially.

$$
\begin{aligned}
&\textit{while}(\mathbf{FX}-\mathbf{GX}) < \textit{tolerance}, \text{ do:} \\
&\quad q \leftarrow \mathbf{FX} \\
&\quad v \leftarrow 2q - \mathbf{X} \\
&\quad \mathbf{X} \leftarrow 2\mathbf{G}v - v
\end{aligned}
\tag{8.7}
$$

Figure 8.1 illustrates the progression of the MACE algorithm, beginning from a single state for all agents. Each state is updated as a function of both the individual agent (line 1 of the loop in equation (8.7)) and the consensus of all agents (line 3 of the loop in equation (8.7)). At equilibrium, one further MACE step places all agents at the mean state position.

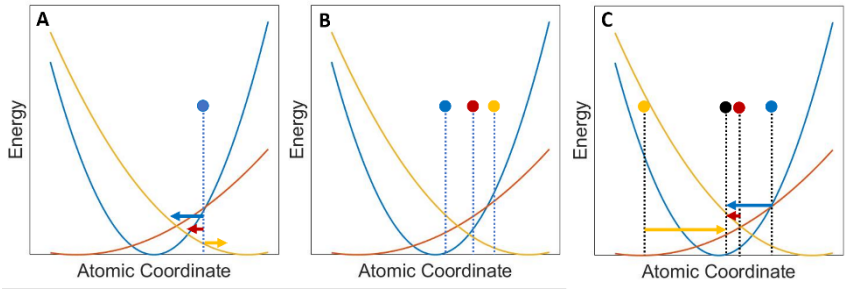

Figure 8.1 Harmonic example of MACE algorithm progression. A) Initial conditions for MACE; all models begin in the same state. Colored arrows represent the varying gradient of each potential. B) State after one step. Each agent has advanced to a unique position. C) Final state for each agent and the equilibrium result.

It is useful to contextualize the general approach of MACE with a simple analogy. Consider several people, each walking a dog within a park. Here, $\mathbf{X}$ gives the position of each person, while $\mathbf{F}(\mathbf{X})$ gives the position of each dog. Each person is simply walking their dog, and they do not care to influence where the dog walks; in turn, the dogs are all interested in investigating a particularly enticing bush. When each person eventually walks the dog to said bush, equilibrium is reached; $\mathbf{F}(\mathbf{X}) = \mathbf{G}(\mathbf{X})$. This position of equilibrium is analogous to the result in MACE, where each dog (agent) exerts a force on the global state (the average position of each person), until all forces balance and the optimization (the walk) stops.

8.3 MACE and Underdetermined Models

The defining novel aspect of MACE in the context of structure determination is the ability to incorporate measurements and models that are underdetermined to recover the structure alone. The general structure of a MACE calculation is composed of one or more computational agents with zero or more experimental agents. In the broader context of model fusion, MACE allows the use of underdetermined systems as constraints upon at least one determined model for modeling any property in a chemical system. Within this study, the underdetermined experimental agent selected to illustrate this mathematical architecture is the moment of inertia (MoI).

To utilize MoI as a constraint, the cost function $cost = \sum(mR^2 - I)^2$ is implemented within the inertia agent. In this function, *R* is the set of atomic coordinates describing the state of the molecule, *I* is the empirically derived inertia tensor, and *m* is the vector of masses of each constituent atom. The inertia agent takes a single gradient descent step upon the cost function of the forward model predicting MOI from a given set of atomic coordinates. Analogous to the approach described in Figure 1, gradients and gradient descent steps for *ab initio* quantum chemical methods are also computed, and MACE steps are taken for each agent. The MACE step updates the state describing the molecular structure for each agent individually, until the equilibrium geometry is achieved. For simple molecular systems, such as H_2 or H_2O, the molecular degrees of freedom provide an overdetermined mapping from MOI to structure, and the use of computational agents is not required for an accurate reconstruction of the molecule. For systems with greater than 3 atoms (not considering isotopomers), this cost function alone is insufficient to determine the molecular structure, as the fitting from moment of inertia to atomic coordinates is underdetermined. In these cases, the computational agents play the larger role of constraining the total set of states to physically reasonable structures.

8.4 Computational Methods

All *ab initio* calculations were conducted with the GAMESS electronic structure package, version 2016 R1.[19] Geometry optimizations were performed via three distinct methods: i) single agent, gradient descent optimizations done solely in GAMESS; ii) 4 agent, utilizing the four computational agents Hartree-Fock / cc-pVDZ, MP2/cc-pVTZ, M06/cc-pVTZ, and PM3; iii) 5

agent, utilizing the same four computational agents and an additional experimental agent. The experimental agent was the gradient-descent optimizer of an empirical model for the moment of inertia. Additional geometry optimizations were performed with CCSD(T)/cc-pVTZ for all systems for comparative purposes. To calculate the root mean square deviation (RMSD) between molecular structures, the Kabsch algorithm was utilized as implemented through the PyPI package.[20, 21] To implement the MACE framework a suite of functions in Python were written, enabling parallel execution of individual gradient computations and calculation of the MACE step during the equilibrium computation.

8.5 Simple Diatomic Systems – H_2

Initial proof-of-concept studies demonstrated fusion of multiple harmonic potential models of H_2. The simple first test utilized Hartree-Fock calculations of energy with 6-31G*, 6-31+G, and cc-pVDZ basis sets. H_2 was fixed at a bond length of 0.80 Å and shortened to a length of 0.60 Å in 0.01 Å increments; the resulting energy curve was fit to a polynomial function. Table 1 below contrasts the equilibrium bond length obtained for fitting to each potential individually with the MACE and experimental result.

Table 8.1 H_2 bond lengths from HF calculations compared with MACE and experiment.

	6-31G*	6-31+G	cc-pVDZ	MACE	Experiment
Equilibrium Bond Length (Å)	0.7326	0.7300	0.7480	0.7405	0.74[22]

These calculations provide evidence for potential utility of MACE in fusing models of ab initio chemistry. Notably, the MACE result of 0.7405 differs from the average of optimizing each individual agent, 0.7369. To illustrate why this difference occurs, consider the bond-length optimization as the process of finding a minimum along a potential energy surface. The equilibrium bond length occurs at the minimum of the potential energy surface. Averaging the results from several models will in turn find the average of these minima. In contrast, MACE does not locate the minima of each agent. The equilibrium result is the point where the sum of all agents is minimized.

In the data shown in Table 8.1, MACE was implemented by fitting a polynomial to energy evaluations with different bond lengths, thus requiring a series of calculations to be run prior to MACE. Rather than manually fitting a set of energies to a polynomial, direct optimization of each agent reduces the total number of necessary ab initio computation steps and removes the arbitrary precision limit imposed by fitting to a fixed step size potential.

8.6 Small Molecule Testing

Direct optimization was implemented by evaluating the gradient of electronic energy with respect to atomic coordinate for each agent directly. The set of gradients was then utilized to calculate the next set of state vectors X_k, i.e., a single MACE step.

To test this architecture, CCSD(T)/cc-pVTZ calculations were conducted to generate optimized geometries for the five test molecules H_2O, HCN, SO_2, pyridine, and urea. From these "ground-truth" geometries, the inertia tensor was calculated and utilized as a surrogate for an experimental observable. The inertia agent minimizes the deviation between the predicted inertia tensor and the inertia tensor obtained from the CCSD(T) result. **Figure 8.2** illustrates the difference between the obtained MACE result and direct optimization of a single agent, e.g., gradient descent upon the potential energy surface of the Hartree-Fock wavefunction.

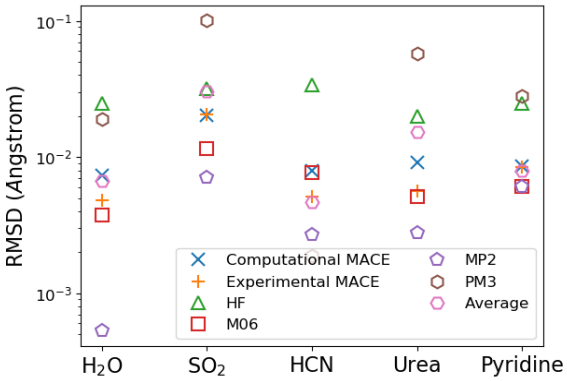

Figure 8.2 RMSD (Å) of individual agents with cc-pVTZ/CCSD(T) structure plotted on a log scale. Computational MACE utilizes 4 computational agents, while experimental MACE also includes the inertia agent.

From **Figure 8.2**, several points can be observed. First, as anticipated, the MACE result is not equivalent to averaging the optimum structure for each agent individually. In the above plot the weighting of each agent is equal – as such, inclusion of the inertia agent provides a relatively small change to recovered structure. The spread of structures obtained from direct optimization of *ab initio* and semiempirical structures is variable depending on chemical identity. The box plot of RMSD for urea is one example; the large spread is at least in part due to the PM3 agent, which exhibits an RMSD on average 5.2 times greater than the other three computational agents. Note

that MACE for SO_2 does not generate a structure closer to the CCSD(T) structure than the MP2 or M06 agent individually, and yet generates a smaller RMSD than the average of the agents; this behavior is indicative of the intrinsic weighting associated with the slope of each agents' potential gradient. Put another way, though the PM3 energy minimum is far from the other agents, the steepness of its potential energy surface weights it to a lesser extent in the equilibrium position than an arithmetic mean of the agents would.

The true novelty of MACE is its ability to enable direct integration of empirical models with *ab initio* chemistry. Fusion of the experimental model of moment of inertia with the 4 computational agents was achieved by first taking an experimentally reported structure for each molecule.[22-25] From the experimental structure, the moment of inertia tensor was calculated. If the resulting tensor was not in the principal coordinate system, the eigenvalues of the tensor were solved and used as the experimental constraint in the inertia agent. MACE was then conducted on the five agents. Table 8.2 shows a comparison of the performance of 4 agent MACE (Hartree-Fock / cc-pVDZ, MP2/cc-pVTZ, M06/cc-pVTZ, and PM3) and 5 agent MACE (Hartree-Fock / cc-pVDZ, MP2/cc-pVTZ, M06/cc-pVTZ, PM3, and the inertia agent) and cc-pVTZ/CCSD(T) structure determination with RMSDs computed against the reported experimental structure.

Table 8.2 RMSD of MACE structure (Å) in Cartesian coordinates relative to experimentally reported structure for several small molecules.

	H_2O	SO_2	HCN	Urea	Acetamide	Pyridine
4 Agent MACE	0.33×10^{-2}	1.57×10^{-2}	19.34×10^{-2}	12.91×10^{-2}	11.78×10^{-2}	4.14×10^{-2}
5 Agent MACE	0.13×10^{-2}	1.30×10^{-2}	19.10×10^{-2}	12.95×10^{-2}	11.78×10^{-2}	4.20×10^{-2}
CCSD(T)	0.43×10^{-2}	0.60×10^{-2}	18.59×10^{-2}	13.02×10^{-2}	10.84×10^{-2}	4.67×10^{-2}

Utilization of the inertia agent improves performance for H_2O, SO_2, and HCN, but shows no improvement compared to the 4 agent MACE for urea, acetamide, and pyridine. Notably, the structures that do not improve their result by use of the inertia agent all contain a greater number of structural degrees of freedom than the inertia tensor does itself; it's possible that the lack of improvement stems from the underdetermined nature of the inertia model. The underdetermined nature of the inertia model is, however, one benefit of the MACE architecture, enabling fully determined structure mapping by fusing just a single computational agent with the inertia model.

8.7 Solketal as a Model System of Experimental Constraint

To illustrate the potential utility of MACE in enhancing the structural sensitivity of experimental measurements, the molecule solketal was modeled using a variety of MACE configurations, as well as *ab initio* methods. Solketal contains 9 heavy atoms and consequently is nearing the size of molecule where high-level computations, e.g., cc-pVTZ/CCSD(T) become tedious and potentially difficult to run, depending upon computational resources. The rotational constants of solketal have been previously published.[4] Microwave spectroscopy provides extremely precise spectral measurements, but is insufficient as a sole probe to predict molecular structure for molecules with greater than 3 atoms in the absence of isotopomers. By supplementing the microwave spectroscopy measurements with *ab initio* and semiempirical methods, MACE can produce a molecular structure that more closely aligns with the true measured structure than theoretical methods alone.

It is worth reiterating the power of MACE to enable recovery of structure in situations where normally fitting to structure or properties would be an underdetermined problem. The inertia tensor exhibits reduced dimensionality and degrees of freedom relative to absolute molecular structure. Even by including a single low-cost computational agent, this issue can be circumvented. Calculations of solketal structure can be evaluated by comparison with experimental measurements of the moment of inertia. **Figure 8.3** below contrasts deviations in the inertia tensor of the predicted structure for several different methods. The M06-2X/cc-pVTZ result listed is adapted from Lobsiger et al., which also reports experimental rotational constants used as experimental constraints within the MACE calculations.[4] The RMSD reported for PM3 + M06 + MP2 corresponds to a MACE computation with only 3 computational agents. The Inertia + MP2 + M06 + PM3 and Inertia (0.5) + MP2 + M06 + PM3 result included PM3, M06, and MP2 as agents in addition to the inertia agent; the former weighted all agents equally while the latter set the weighting of the inertia agent to be equal to 50% of the total weighting. The Inertia + PM3 approach included only the experimental agent and PM3.

While it is notable that all reported MACE structures reproduce an inertia tensor comparable to the literature reported structure from M06-2X (taken as the ground truth), the Inertia + PM3 and 4 Agent Experimental results are of greatest interest. RMSDs of MoI were computed by taking the difference between the predicted tensor value and the experimentally measured tensor values in reference 4.[4] Adding the experimental agent into PM3 + M06 + MP2 MACE reduces the RMSD between the predicted inertia tensor and measured value by 0.20 amu/Å^2, approximately 4%. The flexible MACE architecture allows tuning of the system by utilizing differing weights for each agent. Changing the relative weight of each agent during the broadcast mean step of the MACE algorithm will favor certain agents over others in their contribution to the MACE step. Reweighting can conceivably be utilized to prefer certain computational agents over others, or to increase the contribution of the experimental agent. Further increasing the weighting of the inertia agent to be equal to the sum of computational agents results in further improvement in recovered the inertia tensor of 0.96 amu/Å^2, or about 18%. Similarly, reducing the total number of agents to 2, including only the experimental agent and the PM3 agent, yields additional improvement of 0.55 amu/Å^2, or another 13%. Though not plotted, the RMSD of PM3 alone is 28.7, corresponding to a factor of 7.5 reduction in RMSD by including the experimental agent.

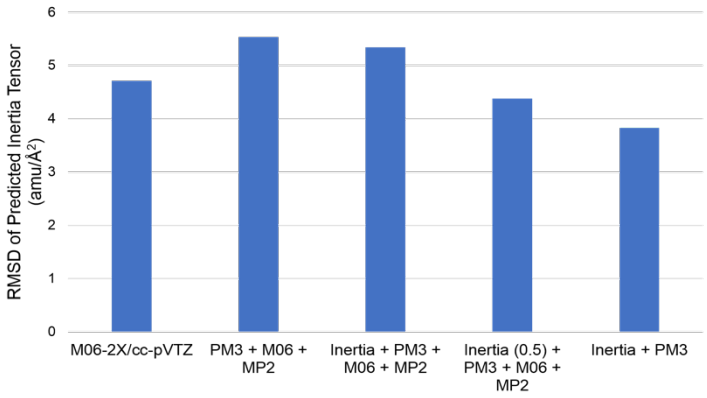

Figure 8.3 RMSD of predicted inertia tensor for structures previously reported in the literature[4] (M06-2X) and those obtained from MACE with varying agents. From left to right, the MACE results correspond to runs with computational agents only, computational and inertia agents, computational and inertia with inertia weighted equal to 0.5, and PM3 plus the inertia agent.

Reducing the number of agents to two gives an overall greater weight to the experimental agent, reducing discrepancy between predicted structure and the structure reflected by empirical measurements. The improved performance of the Inertia + PM3 result is intriguing; the greater contribution of the experimental agent to the equilibrium structure in the two-agent case suggests that the gradient of the PM3 structure may be smaller than the gradient of the other computational agents. This is analogous to the case described in **Figure 8.1** for a simple harmonic potential. The shallowness of the red potential relative to the blue and yellow potentials results in an equilibrium

structure that is closer to the minima of the blue and yellow potentials. In this case, the PM3 is most similar to the red potential and contributes less to the equilibrium structure, while the inertia agent provides a steeper potential akin to the yellow and blue potentials.

Further investigation into the result obtained by optimizing PM3 reveals a key structural difference relative to the other methods. **Figure 8.4** displays an image containing the superimposed PM3 outcome, Inertia + PM3 MACE outcome, and the reported structure from M06-2X.[4] The key structural difference between the PM3 and M06-2X result is most readily observable within the ring moiety. Consider the plane defined by the three carbon atoms in the ring; the literature M06-2X structure exhibits the oxygens above this plane, closer to the alcohol moiety. This upward "pucker" contrasts with the PM3 result, where the oxygens are puckered downward relative to the plane of the ring carbons and the alcohol moiety. Note that the M06-2X structure reported previously is in excellent agreement with the structure obtained by solving Kraitchman's equations.[4] While the PM3 optimization alone results in a distinct structural difference, inclusion of the inertia agent as a constraint on structure eliminates this failure, resulting in an upward pucker and oxygens oriented above the carbon plane. This outcome is illustrative of the potential power in fusing experimental measurements with theoretical values. In this case not only is an underdetermined chemical problem in the form of full structure determination from the MoI achieved, but also the experimental constraint served to improve upon deficiencies in the theoretical model.

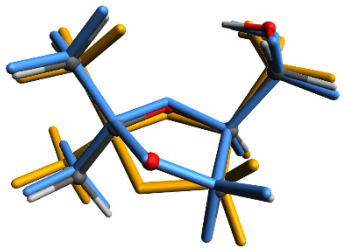

Figure 8.4 Overlay of M06-2X structure (atom-type colored), PM3 structure (yellow), and 2 agent MACE structure (blue) of solketal colored by atom type. Inclusion of the inertia agent constrains recovered geometry to more physical results.

It is worth briefly discussing the scaling attributes of the MACE framework. The addition of experimental constraints via MACE is a simple parallelizable process. Evaluation of the gradient of the experimental agent in the present study was computationally much cheaper than even the semiempirical PM3 methods used. However, this is a property of the model and will vary depending upon the target of study. During MACE, each computational agent is called in parallel; provided sufficient parallelization resources, computational time for each equilibrium step is

limited by the agent with the greatest computational cost. The scaling of agents incorporated into the equilibrium evaluation is additive.

8.8 Conclusions

MACE was demonstrated for formal fusion of *ab initio* methods with experimental measurement. Weighting showed a reduced RMSD for the equilibrium structure relative to individual agents. When compared to direct optimization of structure with the theoretically superior cc-pVTZ/CCSD(T) method MACE achieved comparable accuracy as measured by the RMSD relative to the reported experimental structure for several small molecules, while utilizing computational agents with lower scaling. Further tuning of weighting parameters, as well as implementation of more sophisticated iterative reweighting approaches to reduce contribution of poorly performing agents are anticipated to improve the performance of MACE. In addition to quantifying MACE performance with respect to "ground truth" structures obtained from CCSD(T)/cc-pVTZ calculations, experimental reports of rotational spectroscopy of solketal were used to generate structures informed by experiment. The MACE result fusing previously reported inertia tensors with *ab initio* modeling generated a structure whose inertia tensor more closely resembled experiment than pure *ab initio* methods. Furthermore, the structure obtained from a single low-cost computational agent (PM3) was demonstrably improved via fusion with the experimental agent constraining structure to empirically determined moments of inertia. With the demonstration of successful fusion for the simple empirical parameters of the moments of inertia, future work can leverage more complex empirical feedback for structural determination, such as powder x-ray diffraction patterns or infrared spectra.

8.9 References

1. Baquero, E. E.; James, W. H.; Choi, S. H.; Gellman, S. H.; Zwier, T. S., Single-Conformation Ultraviolet and Infrared Spectroscopy of Model Synthetic Foldamers: β-Peptides Ac-β3-hPhe-NHMe and Ac-β3-hTyr-NHMe. *Journal of the American Chemical Society* **2008,** *130* (14), 4784-4794.

2. McGlone, S.; Elmes, P.; Brown, R.; Godfrey, P. D., Molecular structure of a conformer of glycine by microwave spectroscopy. *Journal of molecular structure* **1999,** *485*, 225-238.

3. Pispisa, B.; Palleschi, A.; Mazzuca, C.; Stella, L.; Valeri, A.; Venanzi, M.; Formaggio, F.; Toniolo, C.; Broxterman, Q., The versatility of combining FRET measurements and molecular mechanics results for determining the structural features of ordered peptides in solution. *Journal of Fluorescence* **2002,** *12* (2), 213-217.

4. Lobsiger, S.; Perez, C.; Evangelisti, L.; Lehmann, K. K.; Pate, B. H., Molecular Structure and Chirality Detection by Fourier Transform Microwave Spectroscopy. *The Journal of Physical Chemistry Letters* **2015,** *6* (1), 196-200.

5. Saer, R. G.; Stadnytskyi, V.; Magdaong, N. C.; Goodson, C.; Savikhin, S.; Blankenship, R. E., Probing the excitonic landscape of the Chlorobaculum tepidum Fenna-Matthews-Olson (FMO) complex: a mutagenesis approach. *Biochimica et Biophysica Acta (BBA)-Bioenergetics* **2017,** *1858* (4), 288-296.

6. Matta, C. F., How dependent are molecular and atomic properties on the electronic structure method? Comparison of Hartree-Fock, DFT, and MP2 on a biologically relevant set of molecules. *Journal of Computational Chemistry* **2010,** *31* (6), 1297-1311.

7. Huang, C.; Ackerman, J. L.; Petibon, Y.; Brady, T. J.; El Fakhri, G.; Ouyang, J., MR-based motion correction for PET imaging using wired active MR microcoils in simultaneous PET-MR: Phantom study. *Medical physics* **2014,** *41* (4), 041910.

8. Chang, B. R.; Tsai, H. F.; Young, C.-P., Intelligent data fusion system for predicting vehicle collision warning using vision/GPS sensing. *Expert Systems with Applications* **2010,** *37* (3), 2439-2450.

9. Bouman, K. L.; Johnson, M. D.; Zoran, D.; Fish, V. L.; Doeleman, S. S.; Freeman, W. T. In *Computational imaging for vlbi image reconstruction*, Proceedings of the IEEE Conference on Computer Vision and Pattern Recognition, 2016; pp 913-922.

10. Gutiérrez, J. M.; Haddi, Z.; Amari, A.; Bouchikhi, B.; Mimendia, A.; Cetó, X.; del Valle, M., Hybrid electronic tongue based on multisensor data fusion for discrimination of beers. *Sensors and Actuators B: Chemical* **2013,** *177*, 989-996.

11. Smilde, A. K.; van der Werf, M. J.; Bijlsma, S.; van der Werff-van der Vat, B. J.; Jellema, R. H., Fusion of mass spectrometry-based metabolomics data. *Analytical chemistry* **2005,** *77* (20), 6729-6736.

12. Roussel, S.; Bellon-Maurel, V.; Roger, J.-M.; Grenier, P., Fusion of aroma, FT-IR and UV sensor data based on the Bayesian inference. Application to the discrimination of white grape varieties. *Chemometrics and Intelligent Laboratory Systems* **2003,** *65* (2), 209-219.

13. Gordon, M. S.; Fedorov, D. G.; Pruitt, S. R.; Slipchenko, L. V., Fragmentation Methods: A Route to Accurate Calculations on Large Systems. *Chemical Reviews* **2012,** *112* (1), 632-672.

14. Olsson, S.; Wu, H.; Paul, F.; Clementi, C.; Noé, F., Combining experimental and simulation data of molecular processes via augmented Markov models. *Proceedings of the National Academy of Sciences* **2017**, 201704803.

15. Buzzard, G. T.; Chan, S. H.; Sreehari, S.; Bouman, C. A., Plug-and-Play Unplugged: Optimization-Free Reconstruction Using Consensus Equilibrium. *SIAM Journal on Imaging Sciences* **2018,** *11* (3), 2001-2020.

16. Sridhar, V.; Wang, X.; Buzzard, G. T.; Bouman, C. A., Distributed Iterative CT Reconstruction using Multi-Agent Consensus Equilibrium. *arXiv preprint arXiv:1911.09278* **2019**.

17. Majee, S.; Balke, T.; Kemp, C.; Buzzard, G.; Bouman, C., *4D X-Ray CT Reconstruction using Multi-Slice Fusion*. 2019; p 1-8.

18. Giselsson, P.; Boyd, S., Metric selection in fast dual forward–backward splitting. *Automatica* **2015,** *62*, 1-10.

19. Gordon, M. S.; Schmidt, M. W., Advances in electronic structure theory: GAMESS a decade later. In *Theory and applications of computational chemistry*, Elsevier: 2005; pp 1167-1189.

20. *Calculate Root-mean-square deviation (RMSD) of Two Molecules Using Rotation*, 1.3.2; GitHub.

21. Kabsch, W., A solution for the best rotation to relate two sets of vectors. *Acta Crystallographica Section A: Crystal Physics, Diffraction, Theoretical and General Crystallography* **1976,** *32* (5), 922-923.

22. Herzberg, G., *Electronic spectra and electronic structure of polyatomic molecules*. Van Nostrand: New York, 1966.

23. Hoy, A.; Bunker, P. R., A precise solution of the rotation bending Schrödinger equation for a triatomic molecule with application to the water molecule. *Journal of Molecular Spectroscopy* **1979,** *74* (1), 1-8.

24. Mata, F.; Quintana, M. J.; Sørensen, G. O., Microwave spectra of pyridine and monodeuterated pyridines. Revised molecular structure of pyridine. *Journal of Molecular Structure* **1977,** *42*, 1-5.

25. Godfrey, P. D.; Brown, R. D.; Hunter, A. N., The shape of urea. *Journal of molecular structure* **1997,** *413*, 405-414.

VITA

Dr. James Ulcickas attended undergraduate at Keene State College in Keene, NH from 2011 to 2015. During his time there he was introduced to chemistry research first in the field of analytical chemistry, where he studied natural product extraction and quantitation. His earliest studies focused on quantification of cortisol in equine saliva via capillary electrophoresis with Prof. James Kraly. Later, extraction of the natural antioxidant resveratrol from Japanese knotweed quantified resveratrol via capillary electrophoresis and gas chromatography – mass spectrometry. In 2013, James attended an NSF Research Experience for Undergraduates at the University of Connecticut. Working with Prof. José Gascón, he aided in the development of a connectivity-based force field for thiolated gold nanoclusters. After returning to Keene State College he synthesized ionic liquids with Dr. Denise Junge. James attended Purdue University in 2015 in the Department of Chemistry with a focus on physical chemistry. After a brief period working with Dr. Libai Huang in the study of exfoliated graphene coupled with 2D transition metal dichalcogenides, he joined the Garth Simpson group for nonlinear optics. Following graduation, James will be joining Northrop Grumman as a systems engineer.

PUBLICATIONS

1. Ulcickas, J. R. W., Simpson, G. J. Mueller Tensor Nonlinear Optical Polarization Analysis in Turbid Media. *J. Phys Chem B*. **2019**, *123* (30), 6643-6650.

2. Geiger, A. C,. Ulcickas, J. R. W., Liu, Y., Witinski, M.F. Blanchard, R. Simpson, G. J. Sparse-sampling methods for hyperspectral infrared microscopy, *Proc. SPIE 10980, Image Sensing Technologies: Materials, Devices, Systems, and Applications VI*, 1098016, 13 May **2019**

3. Ulcickas, J. R. W., Ding, C., Simpson, G. Connecting Mueller and Jones tensors for describing nonlinear optical conversion of unpolarized light. *Proc. SPIE 10882, Multiphoton Microscopy in the Biomedical Sciences XIX*, 1088217, 22 February **2019**

4. Ding, C., Ulcickas, J., Deng, F., Simpson, G. Spatial encoded polarization dependent nonlinear optical analysis for local tensors imaging of collagenous tissue, *Proc. SPIE 10883, Three-Dimensional and Multidimensional Microscopy: Image Acquisition and Processing XXVI*, 108831E, 21 February **2019**

5. Ulcickas, J. Ding, C. Deng, F. Simpson, G. Spatially encoded polarization-dependent nonlinear optics. *Opt. Lett.* **2018**, *43(24)*, 5973.

6. Ulcickas, J. Deng, F. Ding, C. Simpson, G. Mueller tensor approach for nonlinear optics in turbid media. *Proc. SPIE 10498*, **2018**, Multiphoton Microscopy in the Biomedical Sciences XVIII, 1049834.

7. Ding, C.; Ulcickas, J.; Deng, F; Simpson, G. Second Harmonic Generation of Unpolarized Light. *Phys. Rev. Lett.* **2017**, *119*, 193901.

8. Deng, F.; Ulcickas, J.; Simpson, G. Theoretical Foundation for Electric-Dipole-Allowed Chiral-Specific Fluorescence Optical Rotary Dispersion (F-ORD) from Interfacial Assemblies. *J. Phys. Chem. Lett.* **2016**, *7*, 4248–4252.

9. Dow, X.; DeWalt, E.; Sullivan, S.; Schmitt, P.; Ulcickas, J.; Simpson, G. Imaging the Nonlinear Susceptibility Tensor of Collagen by Nonlinear Optical Stokes Ellipsometry. *Biophys. J.* **2016**, *111*, 1361–1374.